
This is an electronic reprint of the original article.
This reprint may differ from the original in pagination and typographic detail.

Santos Silva, Maria; Malitckii, Evgenii; Santos, Telmo G.; Vilaça, Pedro

Review of conventional and advanced non-destructive testing techniques for detection and characterization of small-scale defects

Published in:
Progress in Materials Science

DOI:
[10.1016/j.pmatsci.2023.101155](https://doi.org/10.1016/j.pmatsci.2023.101155)

Published: 01/09/2023

Document Version
Publisher's PDF, also known as Version of record

Published under the following license:
CC BY

Please cite the original version:
Santos Silva, M., Malitckii, E., Santos, T. G., & Vilaça, P. (2023). Review of conventional and advanced non-destructive testing techniques for detection and characterization of small-scale defects. *Progress in Materials Science*, 138, Article 101155. <https://doi.org/10.1016/j.pmatsci.2023.101155>

This material is protected by copyright and other intellectual property rights, and duplication or sale of all or part of any of the repository collections is not permitted, except that material may be duplicated by you for your research use or educational purposes in electronic or print form. You must obtain permission for any other use. Electronic or print copies may not be offered, whether for sale or otherwise to anyone who is not an authorised user.



Review of conventional and advanced non-destructive testing techniques for detection and characterization of small-scale defects

Maria Inês Silva^{a,*}, Evgenii Malitckii^a, Telmo G. Santos^{b,c}, Pedro Vilaça^a

^a Department of Mechanical Engineering, School of Engineering, Aalto University, 02150 Espoo, Finland

^b UNIDEMI, Department of Mechanical and Industrial Engineering, NOVA School of Science and Technology, Universidade NOVA de Lisboa, 2829-516 Caparica, Portugal

^c Laboratório Associado de Sistemas Inteligentes, LASI, 4800-058 Guimarães, Portugal

ARTICLE INFO

Keywords:

Non-destructive testing
Small-scale defects
Electromagnetism
Radiation
Ultrasonic
Hydrogen-as-a-probe
Machine learning

ABSTRACT

Inspection reliability of small-scale defects, targeting dimensions below 100 μm , is crucial for structural safety of critical components in high-value applications. Early defects are often possible to repair, contributing for the circular economy and sustainability by allowing extended life and reuse of components. During in-service operation, the small-scale defects are typically originated from creep, fatigue, thermal cycles, and environmental damage, or any combination of these multiphysical loading conditions. What are thresholds in Non-Destructive Testing (NDT) techniques to detect and reliably characterise small-scale defects? What is the state of the art of NDT-based solutions, in terms of small-scale defects located at surface, and interior of materials? Examples of small-scale defects in engineering materials are established, and a holistic review is composed on the detectability in terms of sensitivity and resolution. Distinguishable high detection accuracy and resolution is provided by computed tomography paired with computer laminography, scanning thermal microscopy paired with Raman spectroscopy, and NDT techniques paired with machine learning and advanced post-processing signal algorithms. Other promising techniques are time-of-flight diffraction, thermoreflectance thermal imaging, advanced eddy currents probes, like the IONic probe, micro magnetic bridge probe used in magnetic flux leakage, driven-bacterial cells, Quantum dots and hydrogen-as-a-probe.

1. Introduction

Early imperfections, such as leading damage, are physical discontinuities that are present in the atomic structure of the original material or are formed during manufacturing or service time. An imperfection becomes a defect when it jeopardizes the component's integrity and/or function, by any change in its size, shape, or material properties, making it not suitable for its desirable or intended requirement, which may consequently lead to failure [1]. For instance, a component is susceptible to fail when there are internal defects and the service temperature is above 0.5 of the melting temperature (e.g. creep) [2,3]; when there are surface defects in components under bending and/or torsion dynamic loads (e.g. fatigue) [4]; or when loaded defective components operate in chemically active environment (e.g. stress-corrosion cracking) [5]. Therefore, the presence of small-scale defects may yield critically

* Corresponding author.

E-mail address: maria.santossilva@aalto.fi (M. Inês Silva).

negative consequences, like through the loss of products, reduction of a component's service life, environmental damage, repairment costs and overall downtime costs [6]. The detection of early damage will not only avoid fails in service of critical components, but in concept, will also enable the healing of those components by repairment of the small-scale defects, e.g. via local heat treatment [7,8], surfacing and coating [9,10], ultrasonic processing [11–13], and powder metallurgy [14].

The main features of discontinuities are: morphology, such as volumetric (spherical or irregular, e.g. porosity or inclusions, respectively) or planar (with or without volume, e.g. cracks and delamination); location, whether they're located at the surface (superficial layer and open to the exterior), subsurface (superficial layer but closed to the exterior) or internal within the material thickness; and size, ranging from few nm to several mm. Depending on the conjugation of these three factors, the discontinuity may be tolerated or not. For example, a spherical discontinuity, such as porosity, is less pernicious than a crack not aligned with the stress field, due to the stress concentration at the crack edge. Similarly, a crack discontinuity that is in a compressive stress zone is not so critical as it is in a tensile stress zone.

At the beginning of the 20th century, with new concepts and tools regarding quantum mechanics being developed, scientists started to explore how to describe the fundamental properties of pure materials [15–17]. In the following decades many defects/crystal imperfections were discovered and characterized, successfully proving early theories, e.g. dislocation theory, disclosed with the development of techniques like X-ray diffraction (1912) and advancements in crystallography [15,18]. The combination of theoretical studies and experimental results, in addition to new developments in computational capacity, and numerical and analytical techniques, allowed to understand and predict the properties and microstructures of engineering materials [15,19]. They also allowed to understand newly developed materials, like nanostructures, for which there is less experimental information available [15]. These developments also contributed to evaluating quantitatively the defect's location, shape, size, evolution, and effect on the performance of the components.

There are many known experimental characterization techniques that acquire information in the micro and nano scale, such as microscopy: optical, electron, acoustic and electromagnetic. Although with great spatial resolution, these techniques can only inspect small areas, have a small penetration depth and therefore are limited to surface domain inspection. They also require considerable time for analysis and interpretation of images, and implicate extracting a sample or cutting a section through the component to examine the exposed surface, which may affect the performance of the component [20–23].

Non-Destructive Testing (NDT) refers to different inspection methods and techniques to evaluate the physical conditions of an object, in order to understand its characteristics and consequent behaviour, without damaging it or interfering with its function [24]. The result from the application of the techniques can be qualitative or enable quantitative inference on relevant characteristics of the imperfection, such as density, size, location, and morphology. The most common NDT techniques are Visual Inspection Testing (VT), Dye Penetrant Testing (PT), Magnetic Particle Testing (MT), Electromagnetic Testing (ET), Thermal/Infrared Testing (IR), Radiographic Testing (RT), Acoustic Emission Testing (AE), and Ultrasonic Testing (UT) [25]. Depending on the level of sophistication of the energy signal processing, the variants of these techniques are frequently classified, and commercialized, as conventional or advanced solutions [26]. NDT is commonly used to inspect raw materials before being processed, to inspect sub-components and final products during and after their manufacture, and to inspect structural systems and equipment during operation and maintenance periods.

During World War II, the NDT experienced a sharp rise owing to the increase of industrial quality control. In the 1950s, the development of commercial NDT instrumentation increased the inspection resolution, allowing thickness measurements of components, detection of major inclusions and to differentiate grain sizes, among others [27]. Following the 1960s, the instrumentation improvement continued with the aid of statistical methods and interferometric concepts increasing once again the techniques' resolution [27]. By that time, it was already common to inspect defects like cracks, voids, porosity, non-metallic inclusions and forging laps, of sizes in the range of millimeters, using NDT techniques [28,29]. Since about five decades ago, new engineering materials, higher quality demands and complex geometries with increasingly safety requirements, as well as the introduction of new defect morphologies with reduced dimensions, have challenged further developments in NDT. Examples are nanostructured materials, functional surfaces and thermal barrier coatings [30], microelectronics [31], optical components and topological defects in liquid crystal textures [32], biomedical and orthodontic devices [33], solar cells [34], microfabrication [35] and additive manufacturing [36,37]. NDT techniques have been also applied in demanding environments, such as power plants [2,38], or in support of demanding quality requirements, such as in defence industry [39], and transportation, with focus on aeronautic [40–42], and marine technology fields [43]. Furthermore, the rise in automation and computational tools have aid in the improvement of data acquisition, storage and processing [27].

In general, a NDT technique involves the application of some type of energy to certain regions or the entire component, followed by the evaluation of the signal resulting from the interaction of that energy with the material properties and condition. The evaluation is implemented directly, or indirectly, using a sensitive detector (e.g. probe, transducer), that can act as an energy source and/or an energy sensitive detector. Discontinuities, that may be imperfections or even defects, are detected from any non-regular interaction of the applied energy with the material domain being inspected. Overall, any energy that interacts chemically and/or physically with a material, can be used for NDT-based inspection. The detection of discontinuities, via acquiring and processing of the output signal, is limited to some level of sensitivity threshold, associated with the technique's fundamentals, inspection conditions, procedure and parameters [24,28].

According to McMaster [28], a typical probing media can consist of movements of matter, transmission of energy or a combined movement of matter and transmission of energy. Movements of matter probing media use a third-body matter in solid, liquid or gas physical condition to inspect a material, for example, photoelastic coating tests, dye penetrant tests and leak testing, respectively. Transmission of energy probing media employ electromagnetic, gravitational and vibrational energy in tests and may or not encompass the presence or motion of matter. Example of methods based on this probing medium are inspection tests in visible

(luminous) or non-visible domain (e.g. infrared or black light); penetrating radiation tests; magnetic-field tests; electrical-field tests; high-energy particles beam-based tests (neutrons, electrons, alpha particles and ions); acoustic emission tests; and ultrasonic tests.

Each NDT technique is usually sensitive to specific regions of the inspected components, to certain types of discontinuities and mechanisms of failure, under limited conditions (e.g. temperature and accessibility) and for certain materials. This depends on the type and mechanisms of energy interaction with the material. The material properties that are typically evaluated by the techniques are geometric, mechanical, electrical, magnetic, acoustic, chemical, thermal. These are affected by properties such as the microstructure, composition, absorption, reflection and scattering. When compared to destructive testing, the NDT techniques include solutions requiring little or no specimen preparation, have portable equipment, can be performed automatically, and have a good temporal resolution. Many also enable online monitoring of fabrication and in-service condition [28].

There are limitations regarding the inspection procedure steps which may compromise the reliability of the information. For instance, the detector sensibility and background disturbances, e.g. from the signal generator, the coupling and certain test conditions, such as the surface finishing. There are also limitations in signal amplification, such as instabilities in high-gain amplifiers, need for frequent re-calibration or sensitivity to environmental changes (e.g. temperature). The modifications of probing medium from interaction with the material need to be big enough to be distinguished from the background noise, which becomes a challenge in very small defects (micro and nano defects). Additionally, enhancing certain parameters, like having higher resolution and better image quality, often results in longer measurement periods and higher operative costs. Therefore, for each NDT technique it is important to adjust the inspection resolution to the size of the sample, and inspection specifications. Moreover, an efficient application of the NDT

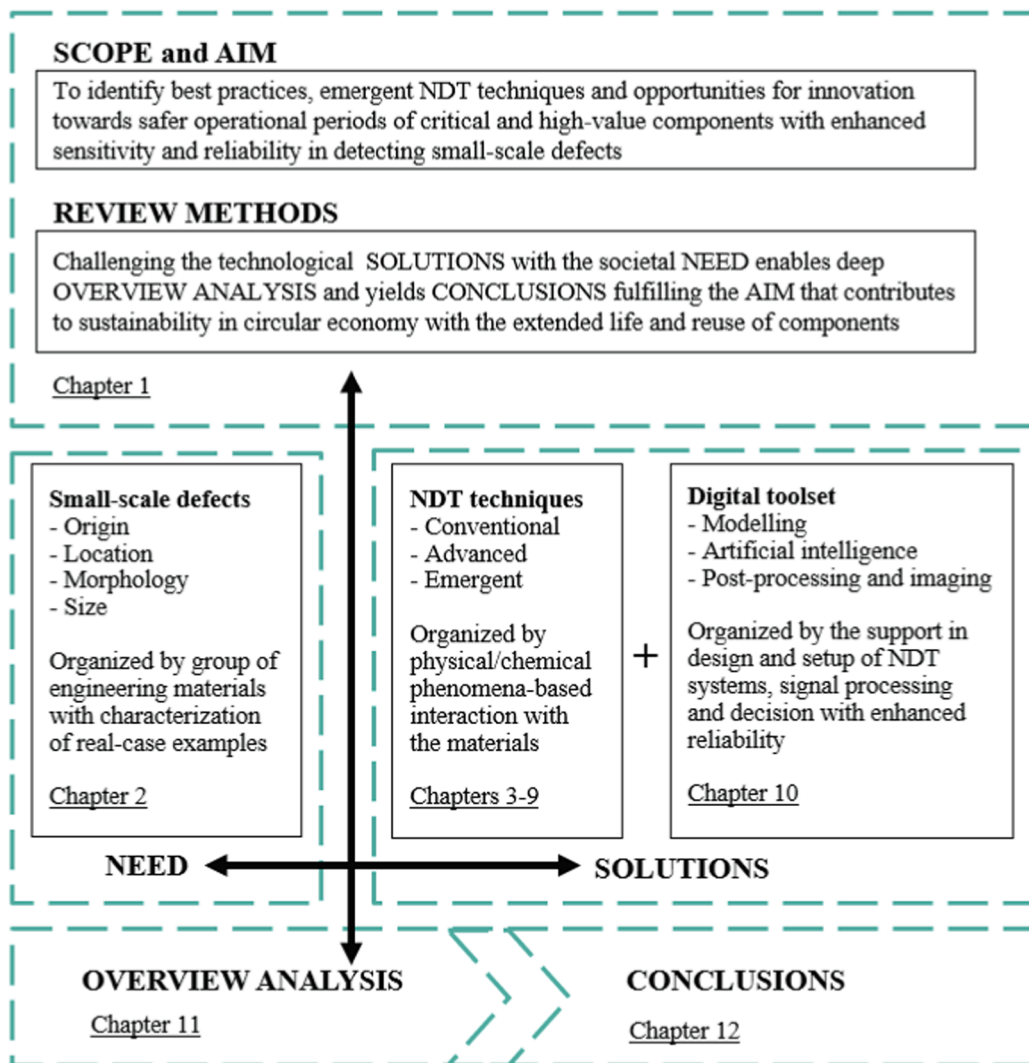
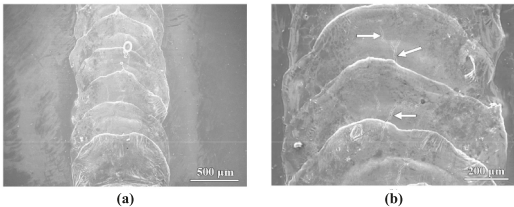
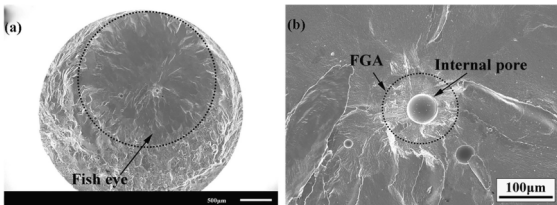
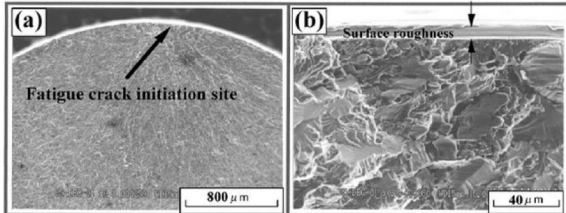
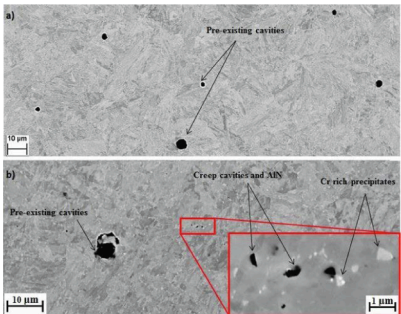


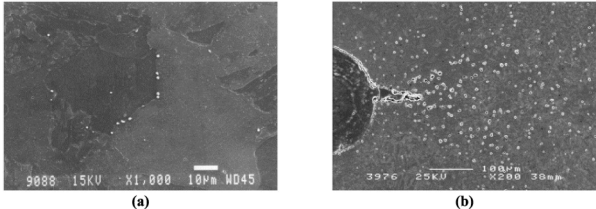
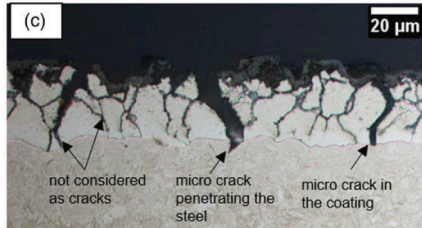
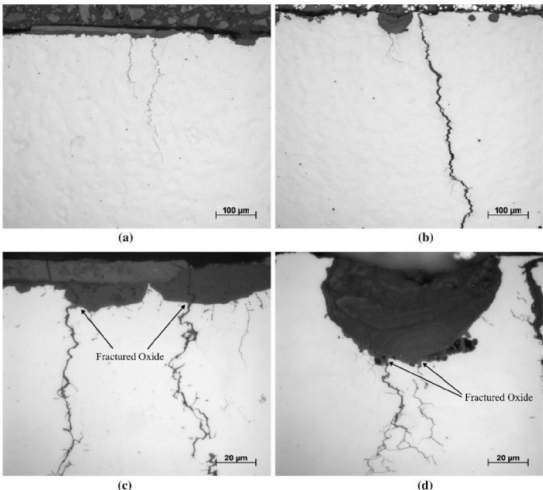
Fig. 1. Graphical representation of the paper’s structure, addressing the scope, aim, and review methods, with a systematic and rational analysis resulting from establishing the need for reliable inspection of multiscale imperfections versus multiphysical technological solutions.

Table 1
Examples of micro defects in metals and alloys.

Type of defects	Dimension domain	Morphology and location
Welding solidification cracking defects	~100 μm	Surface defects
		
		<p>Fig. 2. SEM micrographs of the bead-on-plate laser weld (250 W and 25 mm/s) on magnesium alloy AZ91D: (a) Top view; (b) Close-up showing cracks on the weld surface [70].</p>
Welding pores that induced fatigue fracture	~10 μm	Internal defects
		
		<p>Fig. 3. SEM micrographs of fatigue fracture of a welded joint of TC17 titanium alloy: (a) Overall shape of a single pore of fatigue fracture; (b) Morphology of internal single pore fatigue initiation area ($\sigma_a = 400$ MPa, $N_f = 1.0860 \times 10^7$, FGA = fine granular area) [71].</p>
Artificial surface scratches that induced initiation of fatigue cracking	~10 μm	Surface defects
		
		<p>Fig. 4. SEM micrographs of fatigue fracture surface for Ti-5Al-2.5Sn ELI alloy specimen tested at 77 K ($\sigma_a = 497$ MPa, $N_f = 141; 910$). Photograph (b) is a magnified image as shown by the arrow in (a) [72].</p>
Pre-existing cavities and creep-induced cavities	~1 μm	Internal defects
		
		<p>Fig. 5. SEM micrograph in backscattered electron image (BSE) mode of: (a) As-received material with pre-existing cavities (mean diameter 2.56 μm); (b) Specimen (gauge) crept for 7000 h showing big pre-existing cavity as well as small creep cavities (diameter less than 0.6 μm) and precipitates [73].</p>

(continued on next page)

Table 1 (continued)

Type of defects	Dimension domain	Morphology and location
In-service creep cavitation and laboratory creep-induced cavitation	~1 μm	Internal defects
		 <p>(a) (b)</p>
Micro-cracking in hot deformation of coated steel sheets	~10 μm	Surface defects
		 <p>(c)</p>
Stress corrosion cracking in gas pipelines	~100 μm	Surface defects
		 <p>(a) (b) (c) (d)</p>
		<p>Fig. 8. Cracked surface in gas pipelines: (a) X42 steel; (b) X65 steel; (c) Magnified section showing cracks originating from surface pits in X42 steel; (d) Magnified section showing cracks originating from surface pits in X65 steel [76].</p>

techniques often requires prior knowledge on the defect characteristics, and accessibility to the region to be inspected, which is difficult when it is located internally. No matter if the information from the NDT technique on the defects, is qualitative, or quantitative, it does not allow to determine the defect's severity. Effect of the defects, and appropriate repairment and other measurements are complementary sought information [44,45].

The non-destructive inspection of micro defects, in different materials and components, is a technological issue that remains a scientific challenge. The recent progress in engineering of materials, as well as with micro and nano fabrication, has not been fully accompanied by a parallel development in commercially available NDT solutions.

The purpose of this paper is to identify the best practices and emergent NDT techniques with opportunities for innovation towards enhanced sensitivity and reliability in detecting small-scale defects, with a focus on defect's dimension below 100 μm .

The defects are considered in terms of location, morphology, size of the defects, and their origin (natural or artificial). The review on the techniques addresses their depth of penetration, type of materials possible to inspect, spatial resolution, and typical duration of test procedure. After this introduction, the paper starts with examples and characterization of small-scale defects in different materials. The following sections are dedicated to the current state of the art of existing techniques based on the probing type of energy. [Section 3](#) describes electromagnetic radiation-based testing techniques. [Section 4 and 5](#) address ultrasonic-based testing and acoustic emission techniques, respectively. [Section 6](#) reports on electromagnetism-based testing techniques. [Section 7](#) reviews techniques with motion of matter, and physical and chemical interaction with the inspected surface. [Section 8](#) describes replication metallography testing technique. [Section 9](#) approaches the potential use of hydrogen-as-a-probe, an emerging and highly sensitive inspection method for small-scale defects. [Section 10](#) reviews milestones in analytical and numerical modelling, and artificial intelligence as-aiding tools for enhanced NDT reliability. To sum up, [Section 11](#) comprises an overview of the techniques, and [Section 12](#) presents a reflection on the learnings from the review with final comments and considerations. [Fig. 1](#) summarizes the structure, scope, aim, and review methods considered in this work providing an integrated analysis on the state of the art of conventional, advanced, and emergent non-destructive testing techniques for detection and characterization of small-scale defects.

2. Characterization of small-scale defects in engineering materials

It's important to know the discontinuities present in a component to assess whether those will play, or not, a significant role on the material's engineering performance and the component's service life. The detrimental effect of defects, in terms of their critical size, morphology and location, depends on the material, component geometry and structural features, and application domain. Small-scale defects can have a harmful effect on the performance and safety of the components, especially with the new demands of small-scale products, in industries such as electronic [\[46–48\]](#), biomedical [\[49–53\]](#), and injection moulding [\[54,55\]](#), among others. Specific examples are in the renewable energy industry, the service life of wind turbines' blades is compromised by the propagation of cracks from the order of 10 μm , due to cyclical loading on the component [\[56,57\]](#). In corrosive environments, stress corrosion cracking propagation, from the order of 100 μm , can lead to a component's failure under tensile stress state [\[58\]](#). In the semiconductor industry, defects such as scratches, stains or localized failed patterns in wafers, produced during manufacturing, may decrease the component's performance [\[59\]](#). In nuclear power plants, different components of nuclear reactors, when subjected to nominal temperatures between 300 and 600 $^{\circ}\text{C}$, will eventually fail owing to fatigue and/or creep-fatigue induced damage, that will grow into critical dimensions, from sizes in the order of 10 μm [\[60\]](#).

2.1. Metallic materials

In metals and its alloys, discontinuities at the atomic scale affect the crystalline structure of materials and can be classified as local discontinuities, such as interstitial impurities, substitutional impurities and vacancies; and linear discontinuities, such as dislocations and the intersection of three grains boundaries [\[61\]](#). At a slightly larger scale, between sub- μm and μm scales, there are creep local damage and planar discontinuities, like particle–matrix interfaces, grain boundaries and twin boundaries. Discontinuities between sub-mm and mm scales, such as cracks and notches, occur in the tips of stress concentration sources and/or due to surface reactions at the boundary between the material and environment [\[62,63\]](#). Discontinuities may originate during manufacturing and fabrication, leading to defects such as voids, porosity, cracks and inclusions; during in-service operation, due to overload, wear, environmental damage loading, brittle fracture and metal fatigue or any combination of these multi-physical conditions; or caused by thermal-based processing, like welding, coating, tempering and hardening [\[6,24,62,64–66\]](#). [Table 1](#) shows examples of defects caused by several manufacture and in-service mechanisms.

Fatigue-induced defects occur due to dynamic loads where local stress concentrations from microstructural defects and manufacture defects, not only, but often located in the vicinity of the surface of the components. Examples of crack initiation imperfections are inclusions, microcracks, surface scratches, surface roughness. These imperfections under the cyclic loading, assisted by eventual tensile residual stresses, generate local high stresses that exceed the yield strength and promote cyclic dislocation plasticity initiating and promoting fatigue cracks growth [\[4\]](#).

Creep-induced defects, like cavities or voids, occur due to time-dependent deformation at constant stresses and high temperatures, being also dependent on the material's microstructure. A material experiences three stages of creep, namely: primary or transient creep stage, secondary or steady creep stage, and tertiary or fracture stage [\[67\]](#). These stages are characterized by variations in strain rate and material plasticity, that are a result of multi-mechanisms operating independently, such as strain hardening, recovery, precipitation of carbides and cavity formation [\[2\]](#).

Creep-fatigue defects occur due to a multi-physical damage mechanism dependent on temperature, strain range and rate, hold time, and creep ductility and strength of a component. These defects can be predominantly induced by creep, if there is significant hold time; predominantly induced by fatigue, without any considerable hold time and/or with considerable strain rate; or induced by both mechanisms, with compromising hold time and strain rate [\[3,68\]](#).

Corrosion-induced defects occur due to environmental exposure, e.g. due to damaged coating in pipelines, leading to the degradation of the component, affecting its strength [\[5\]](#). The degradation is a function of the severity of the environmental circumstances and exposure time. There are various types of corrosion damage, depending on the corrosion mechanisms, but common types are uniform corrosion, pitting corrosion and Stress Corrosion Cracking (SCC) [\[5,69\]](#).

2.2. Polymeric-based materials

In composites with polymeric matrix, imperfections may occur in the matrix, fibres, and at matrix-fibre interfaces. Damage in fibres, such as fibre breakage, wrinkling and misalignment, induced in the production of the material, may weaken them, and introduce stress concentrations in the material, therefore, reducing the mechanical properties. In production and storage phases, problems in the matrix can arise due to contamination that leads to a poor cure, e.g. because of incorrect storage, temperature and humidity. Existence of porosity can coalesce and become a void, introducing internal stress concentrations, and/or creating delaminations in the material. In-service, when the materials are subjected to cyclic or monotonic loads, defects like matrix cracking and delamination via separation between fibre and matrix occur. These defects may lead to water infiltration, reduction in elastic and shear modulus with increased chance of buckling, and fibre breakage [77–81].

In polymers, typical imperfections are voids created during the viscous flow and that may grow into cracks. Polymer microstructural imperfections from the polymerization and processing methods (e.g. sub curing, and overcuring) may result in localized residual stresses, microcracks and internal flaws, which are leading defect initiation conditions. In printed-based polymers, distortion and warping of the workpieces, due to expansion and contraction of the plastics as they are printed, leads to stress concentration, and the material can also be contaminated with inclusions (e.g. pigments and stabilizers). These defects may cause crack initiation sites, among other mechanisms that cause loss of mechanical properties and affect the performance of the produced components [82–84]. Table 2 shows examples of micro defects in composites and polymers.

Table 2
Examples of micro defects in composites and polymers.

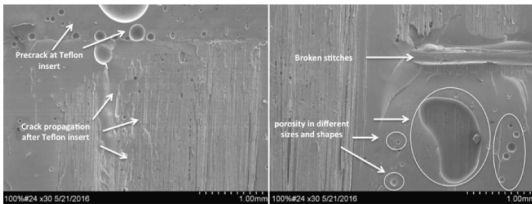
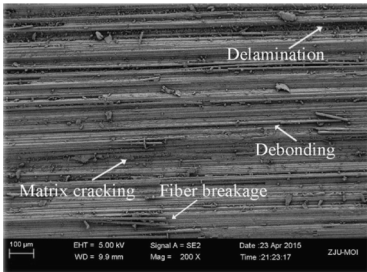
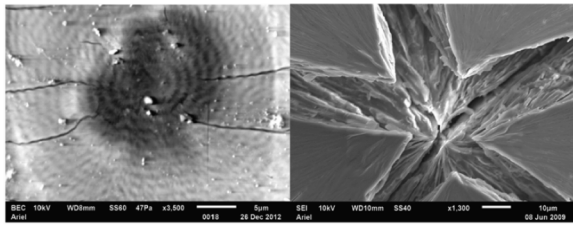
Type of defects	Dimension domain	Morphology and location
Porosity content influenced by vacuum levels in carbon fibre-reinforced polymer composite	from 1 μm to 1 mm	Internal defects 
Delamination, matrix cracking, debonding and fibre breakage	from 1 μm to over 1 mm	Internal defects 
Cracks in semicrystalline polymers	~10 μm	Surface defects 

Fig. 9. SEM micrographs of poor vacuum sample's fracture surface under static mode I [85].

Fig. 10. Various defects in carbon fiber/epoxy composite laminates subjected to single-leg three-point bending tests [86].

Fig. 11. SEM micrograph of: (a) High-density polyethylene (HDPE) spherulite (magnification x3500); (b) PEO 10000 spherulite (magnification x1300). Both exhibit internal micro-cracks [594].

3. Electromagnetic radiation testing

3.1. Conventional and digital X-ray and gamma-ray

Radiographic Testing (RT) is a NDT technique that evaluates the internal conditions of an object through the use of high energy electromagnetic radiation, with very short wavelengths. The typically used ranges of radiation are X-rays, emitted by electron's interaction with an anode target material, and with wavelengths ranging from about 10^{-8} to 10^{-12} m [87], and or γ -rays, emitted by atomic nucleus of radioactive materials and wavelengths shorter than 10^{-10} m [88].

In conventional radiography, a sample is placed between a radiation source, such as Coolidge X-ray tube, and a physical AgBr-based film producing a two-dimensional image upon revelation process; whereas in digital radiography, the radiation can be directly captured in a digital detector, or in a reusable film which is laser scanned. The spatial resolution in digital radiography depends on the digital detector resolution, or laser scanning focal spot. The image is formed based on differential level of energy attenuation due to material thickness, density and its atomic number, which influence the amount of penetrating radiation that is scattered or absorbed [89]. The variations caused by attenuation are recorded by the detector and displayed in two- or three-dimensional representations [46]. Compared to conventional radiography, digital radiography provides better software-based tools for enhancement of image quality, the inspection usually takes less time, does not require additional space, such as a dark room for development and image printing, and in the long term, is more cost-effective [90].

Regarding using X-ray as probing medium, there are various techniques dedicated to different types of material characterization and applications, such as X-ray diffraction, that provides information about the crystallographic structure, chemical composition, and physical properties of materials, such as residual stress measurement [91]; X-ray absorption spectroscopy, which measures the elemental and chemical composition of materials [92]; X-ray scattering, which provides sub-nanometer information about the size, size distribution, electron distribution and structure of nanoparticles [93]; and X-ray imaging, which comprises tomography, laminography, radiography and topography [94].

3.2. X-ray computed tomography

X-ray Computed Tomography (CT) is a digital or computerized X-ray imaging technique that allows the three-dimensional reconstruction of internal and external features of an object, through acquiring a continuous set of scanned images, or slices, composed of voxels [95]. A voxel is a volume element or data point that represents the X-ray absorption in the three-dimensional position of the inspected element. Slices of the object can taken from different rotational angles, by a combined movement of the radiographic detector and the X-ray source, in opposite directions and upon a rotary table. The images are then processed and assembled by a computer algorithm [95].

X-ray computed tomography comprises different imaging acquisition methods and can be used in in-situ investigations [44]. CT is used in fields like electronic [46], energy and energy storage [96–99], aerospace [100,101], medicine [102,103], additive manufacturing [104–107], and metallurgy [108]. There are important differences in the resolution and measurement geometry

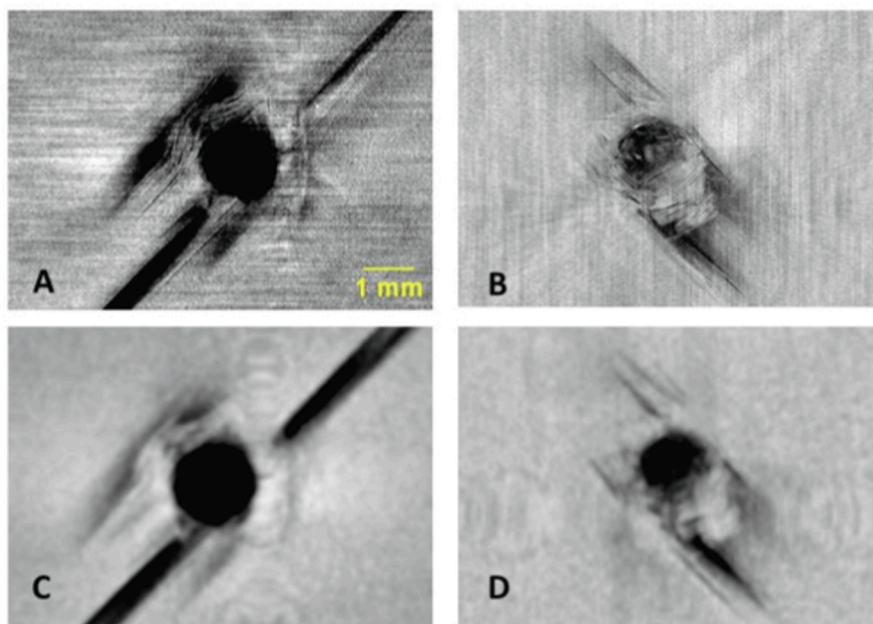


Fig. 12. Slices in planar direction for: (a), (b) Variable zoom X-ray CT; (c), (d) Conventional CT technique [111].

between the CT technologies employed in the different applications, such as medical, material characterization, industrial applications, and dimensional metrology [95,109].

CT has the drawbacks of limited sample sizes, e.g. cylindrical specimens up to about 500 mm of diameter, being time-consuming and expensive, and of having limited measurement capabilities due to the presence of artefacts like beam hardening, scatter radiation, ring artefacts, motion artefacts, noise, among others, although there are various tips in the literature on how to surpass them [44,95,110]. Additionally, it may be difficult to have a high resolution of very small defects in objects with large widths, compared to its thickness, or in objects that need to be placed very close to the X-ray source due to resolution requirements and which prevents a full scan. Nikishkov et al. [111], developed a novel CT technique, Variable Zoom X-ray CT, to overcome some of the mentioned issues, which includes a nonconventional radiograph acquisition trajectory and a modified Feldkamp–Davis–Kress (FDK) reconstruction method. Fig. 12 shows the comparison results of the novel technique and the conventional technique, using a carbon/epoxy composite laminate with 401 mm width and 3.5 mm thickness subjected to low-velocity impact damage [111]. The novel technique was also able to clearly detect delaminations, and damage in a hybrid composite laminate, where defect detection is challenging due to the large contrast variation between carbon and glass fibers.

Furthermore, computed laminography (see §3.3) can also overcome the problem with large widths. CT is also not suitable for materials with low atomic number (Z) and/or low X-ray attenuation contrast (due to low material density). It has difficulty in evaluating high Z materials, such as metals, due to the introduction of the artefacts mentioned above. Moreover, this technique can create very large data sets and requires long time for processing the images [44].

Even though the spatial resolution of CT is affected by the focal spot size of the X-ray source, a variety of CT configurations, such as macro-, micro-, submicron- and nano-CT, has been developed to achieve different spatial resolutions and suitable for different applications [106,112–114]. For instance, nano-CT inspections can be performed through a synchrotron X-ray source or with the help of focusing elements, such as X-ray microscopes (or lens-based systems) [112,115]. Synchrotron radiation are generated by synchrotrons and other accelerators when external forces drive relativistic charged particles to bend their trajectories, producing electromagnetic radiation [115].

Micro-, submicron- and nano-CT can achieve spatial resolutions between 2 and 50 μm , 0.3 and 3 μm , and 0.03 and 0.6 μm , respectively, and temporal resolutions between 0.01 and 3 h, 3 and 12 h, and 8 and 16 h, respectively [116–119]. Furthermore, they can detect discontinuities such as pores, voids, cracks, inclusions or infiltrations, in materials like metals, composites and wood-based materials [114,120,121].

Salarian et al. [105], compared the structural integrity of aluminium rectangular ducts with a thickness of 2.5 mm, produced by laser powder-bed fusion and inspected by micro-CT (3 μm scan) and nano-CT (500 nm scan). Existence of pores in additive manufacturing materials may compromise the integrity and durability of the components. The authors concluded that 3 μm scan did not detect the micro pores (only large pores are visible as shown in Fig. 13a and that there is a discrepancy between the density measurements of nano- and micro-CT (of around 0.41%), as shown in Fig. 13 and Fig. 14, due to each technique's ability to detect small-sized pores, which may be significant when inspecting materials in demanding applications, e.g. fatigue life in aerospace components.

Gong et al. [122], studied the estimation of porosity and detection of lack-of-fusion and keyhole defects in $10 \times 10 \times 10 \text{ mm}^3$ Ti-6Al-4 V samples, with different levels of porosity, produced by Selective Laser Melting (SLM) and Electron Beam Melting (EBM). The inspection was performed with a micro-CT with $7 \times 7 \times 7 \mu\text{m}^3$ voxel size. Fig. 15 shows single slices of the CT scan and the locally reconstructed models of SLM specimens with lack-of-fusion defects. The black areas in the scan indicate the presence of defects, however due to the limitation of detection to a minimum of 21 μm , it is difficult to differentiate it from the bulk material, especially when the porosity level is small, and it is also difficult to identify the defect morphology and locate small defects. Fig. 16 shows the single slices of CT scan and reconstructed models of EBM specimens with lack-of-fusion defects. The authors concluded that the machine setup and detectability play a critical role in defect visualization, and that the defects of SLM samples were harder to observe as compared to the defects of EBM samples, using a micro-CT.

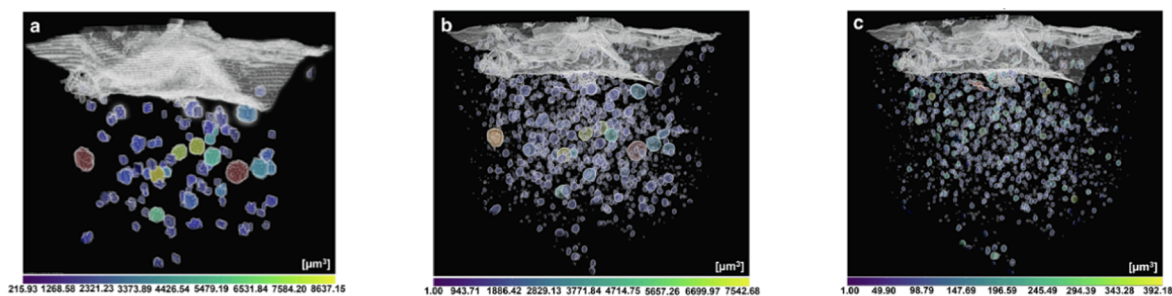


Fig. 13. 3D visualization of porosities at: (a) Micro-scale; (b) Nano-scale; (c) 3D visualization of pore subtraction of the 3 μm /pixel measurement scan from the 500 nm/pixel measurement scan in order to understand the capability of nano-scale imaging [105].

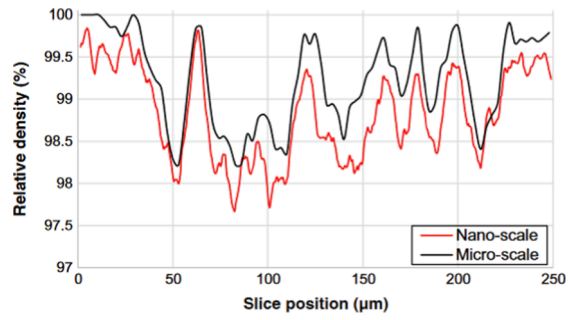


Fig. 14. Density distribution histogram obtained at micro- and nano-scale scans [105].

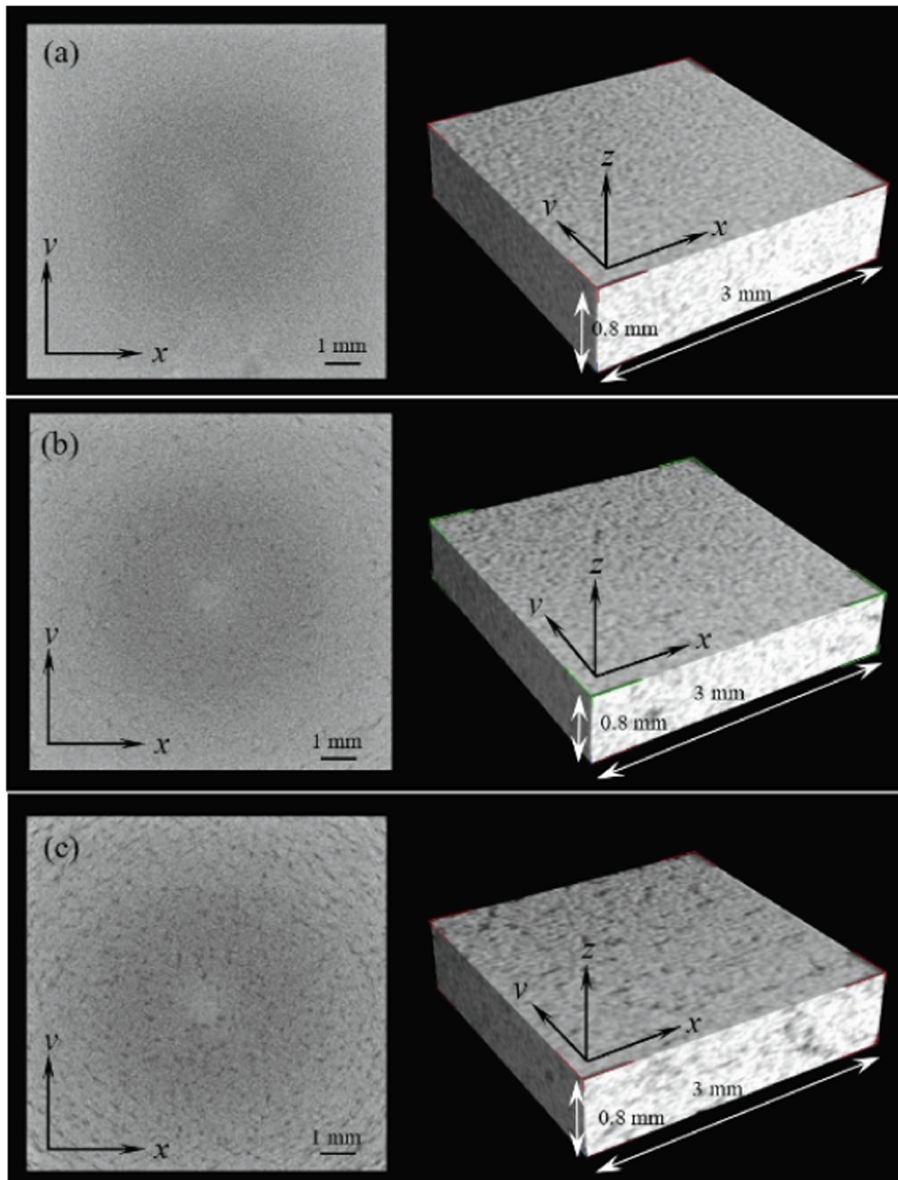


Fig. 15. Single slices and locally reconstructed models of SLM specimens with lack-of-fusion defects: (a) $V = 1080$ mm/s, $RD = 0.3\%$; (b) $V = 1320$ mm/s, $RD = 2.0\%$; (c) $V = 1560$ mm/s, $RD = 6.0\%$ ($V =$ scan speed, $RD =$ estimated porosity) [122].

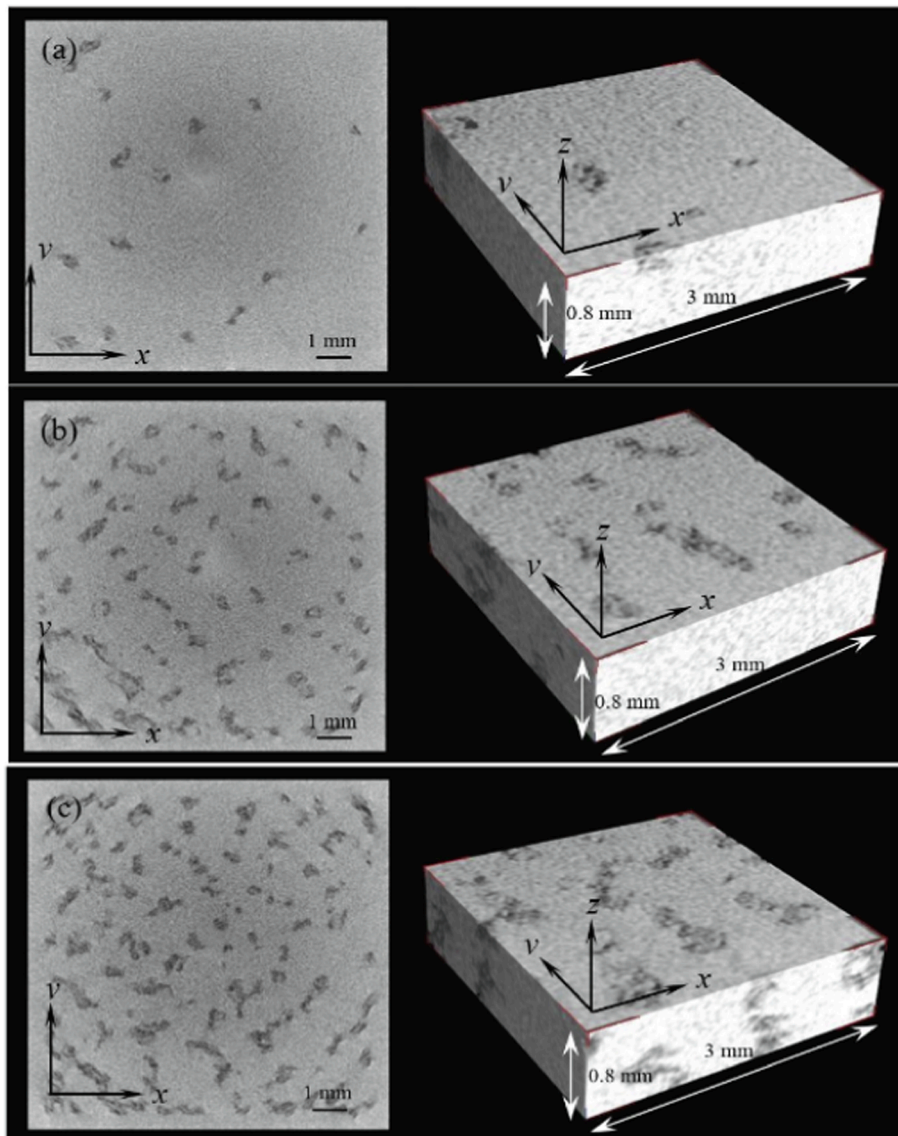


Fig. 16. Single slices and locally reconstructed models of EBM specimens (varied line offset); (a) LO = 0.18 mm, RD = 0.7%; (b) LO = 0.24 mm, RD = 2.0%; (c) LO = 0.30 mm, RD = 4.0% (LO = line offset, RD = estimated porosity) [122].

3.3. X-ray computed laminography

Computed Laminography (CL) is an X-ray analysis technique for the inspection of large and planar components, like printed circuit boards (PCBs) or welding beads. CL is used for inspection of fossils [123], electronics [124,125], welding [126], among others.

In classical laminography, during image acquisition, the X-ray tube and detector move synchronously in opposite directions, which combined with the central beam define a focal plane, i.e. an individual sectional plane of the object. At different positions of the CL components, individual images are generated. Through tomosynthesis (an imaging technique and reconstruction algorithm), it is possible to reconstruct the depth information of the inspected object [127]. Computed laminography is a simple approach since the components remain stationary and the only requirement is a linear translation of the object relative to the tube-detector system, which allows the inspection of larger and heavier objects. Besides, it has better resolution than classical laminography, one scan is enough to acquire all the layers of the specimen, it can overcome the problem of CT in inspecting objects with large widths and the amount of material that needs to be penetrated by X-ray beam is considerably less [123,127]. Similar to CT, CL may also have different artefacts, such as the incorrect centre of rotation (in the case of rotary laminography) and incorrect source-to-object distance, and has lower resolution in other directions than the one directly facing the beam [128]. CL can inspect defects like voids, cracks and pores [129–131].

Since CT and CL have different characteristics and provide different information about the specimen, Zuber et al. [123], proposed

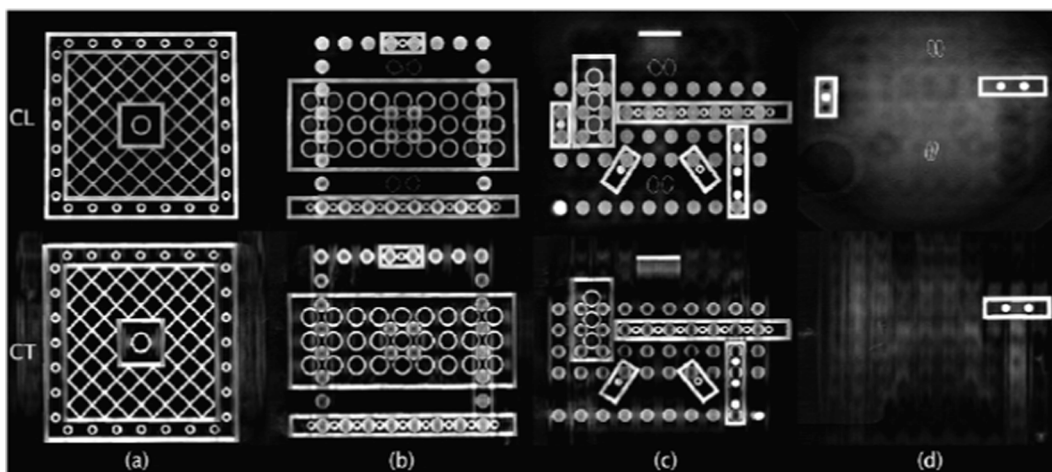


Fig. 17. 3D reconstruction of layers: (a) 1; (b) 2; (c) 3; (d) 4 of a Lego test sample using the CL technique and the limited-angle CT technique. The images shown are slices through the reconstruction volume in the xy plane and layer 1 (a) has size of about $64 \times 64 \text{ mm}^2$ [128].

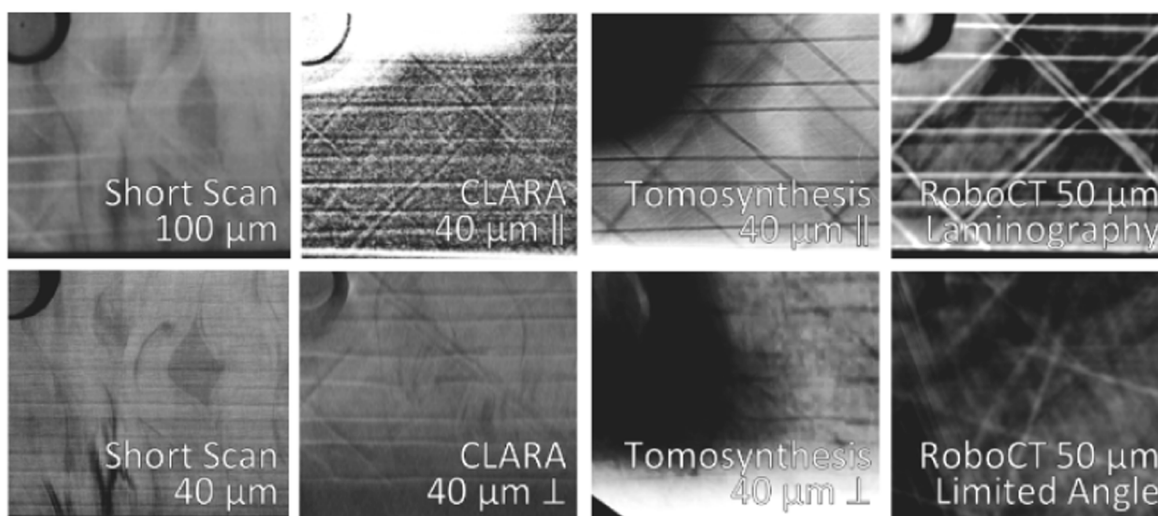


Fig. 18. Comparison of scans of a detail from a CFRP sample using different CT and CL techniques [132].

an Augmented Laminography (AL) that combines both techniques in Fourier space, for example, taking advantage of the constant yet coarser resolution of CT in each direction of the specimen and the better resolution of CL images along the plane parallel to the specimen's face but which may not provide information in all directions.

Fisher et al. [128] have proposed a way of implementing rotary laminography in conventional micro-CT scanners to minimize the need for specialized equipment, and to produce images with fewer artefacts and a more uniform resolution in all directions of the planar object. In conventional CT, the specimen rotates through a vertical axis and projections are taken at equal angle increments, whereas in the CL system, the specimen is tilted at $\alpha = 30^\circ$ to the vertical axis, which facilitates the inspection of flat planar objects. The new system was able to generate high-quality reconstructions in the plane parallel to the specimen face, when compared to limited-angle CT, which was also used to validate and compare the results of the new system, as shown in Fig. 17.

Holub et al. [132], inspected a sample extracted from a BMW i3's side frame, made of Carbon Fibre Reinforced Polymer (CFRP), using different techniques including two distinct CL machines: CLARA and RoboCT laminography. The samples have sizes ranging between $40 \times 80 \text{ mm}^2$ and $40 \times 120 \text{ mm}^2$. Fig. 18 shows the results of different inspection methods of a section of the sample which has a curvature. Axial short scan CT gave the best results and RoboCT provided the easiest inspection of complex components. Overall, laminography provided good results but showed dependency on the orientation of regions-of-interest.

3.4. Thermal characterization techniques

Thermography or Infrared Thermography Testing (IR) is a non-contact NDT technique that acquires and processes the thermal

response of an object, excited by infrared radiation, and that uses an infrared camera and thermographic image software to produce thermograms (thermal images) where there can be detected and identified internal defects through the contrasts of temperature presented.

There are two basic types of IR: passive and active thermography. In passive thermography, there is no external stimulation, and the defect is detected through the difference between the natural temperature of the object and the defect, which must be sufficiently high to be detected by the IR sensor. One limitation is that, when the difference of temperature between the object and defect is zero, the technique cannot detect the flaws [40]. In active thermography, there is an external thermal stimulation of the object to create a heat flux within the material, which generates a difference in temperature between the object and defect and allows the detection and characterization of defects. The heat propagation depends on the material's properties, like thermal conductivity, heat capacity and density [133,134]. The heat sources produce thermal pulses that can last seconds depending on the thickness and material of the object. Examples of these sources are incandescent light bulbs and heat radiators.

IR is used in applications like electronics [135], energy industry [136], aerospace [137], to inspect materials like composites [138,139]. IR is non-intrusive, can inspect large areas in a short period of time, is portable and relatively cheap, when compared to ultrasonic testing and X-ray CT [40,133,140].

Conventional IR techniques, including optically stimulated thermography techniques like pulsed thermography and locked-in thermography, perform poorly when inspecting micro defects. Due to factors like noise, and uniform heating distribution in materials with low emissivity, such as metals [141], at best, it may detect defects in a spatial resolution between 3 and 5 μm [141,142]. IR measurements are commonly restricted by the order of wavelength measured.

Laser thermography is a non-contact technique that heats a sample through a focused laser beam. When in search of increasing the scanning rate, the laser spot can be substituted by a laser line [140]. Zhang et al. [143] proposed a micro-Laser Line Thermography (micro-LLT) technique to inspect submillimeter surface and near-surface defects (between 0.2 and 2 mm) in composites, which proved to be suitable for detecting some, but not all defects [144,145]. According to the authors, this technique can be cheaper when compared to micro-CT. It can detect micro-porosities of 0.162 mm diameter at a depth of 90 μm , but it is time-consuming because only one point can be inspected at a time. It wasn't able to detect through-depth defects in thick samples and porosities smaller than 54 μm [143,146]. Fig. 19a-c shows slices of 10 \times 152 mm² from micro-CT with inspection resolution of 18 μm with some micro-porosities (A, B, C, D and E) and some fibres (F and G) outlined. For comparison purposes, Fig. 19d-f shows slices of the same area of inspection but from micro-LLT inspection. For instance, micro-porosity B with diameter of 0.216 mm at a depth of 0.18 mm is only visible with micro-CT maybe due to the micro-LLT camera resolution limitation or being at the subsurface and below fibre F.

The same authors of [143] conducted another study using micro-LLT and micro-laser spot thermography (micro-LST) with both pulse and lock-in methods for the inspection of composite materials with the same porosities as in Fig. 19. The authors concluded that using micro-LLT lock-in raw images doesn't allow to detect some porosities (like porosity B), similar to micro-LLT [146], but after image processing, using principal component thermography (PCT) and Fourier Transform (FT), the porosities can be detected

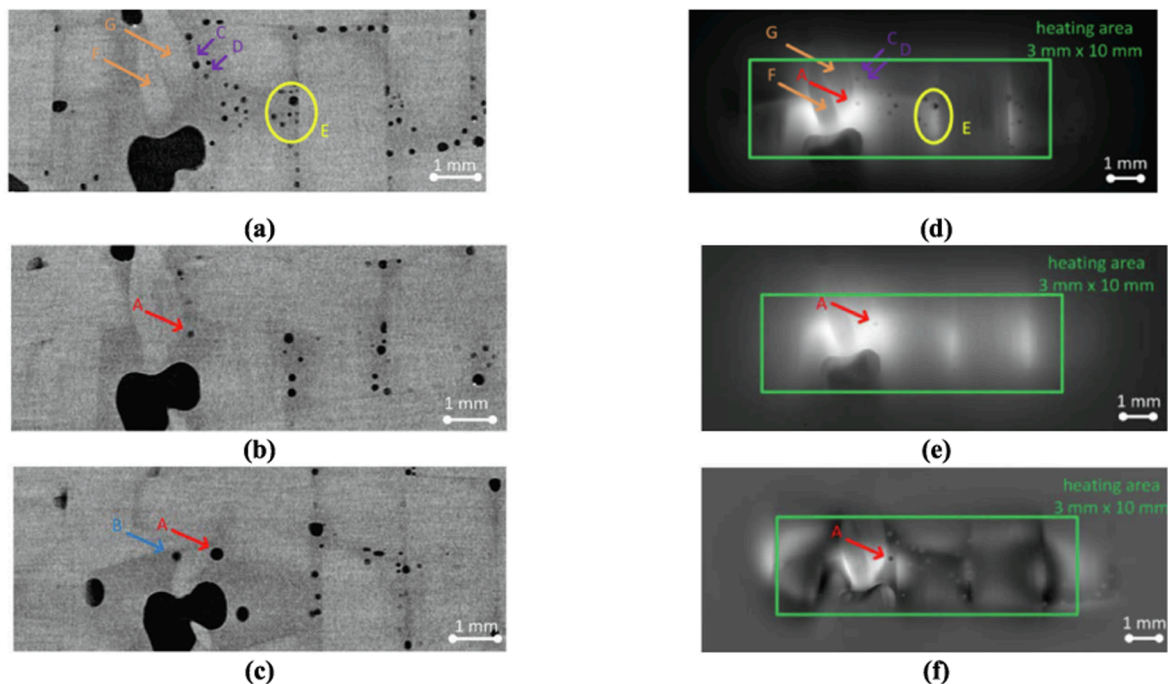


Fig. 19. Micro-CT results of slices at: (a) Surface; (b) Depth of 90 μm ; (c) Depth of 0.18 mm; and micro-LLT results: (d) Cold image; (e) Raw image with contrast adjustment; (f) Principal component thermography (PCT) [146].

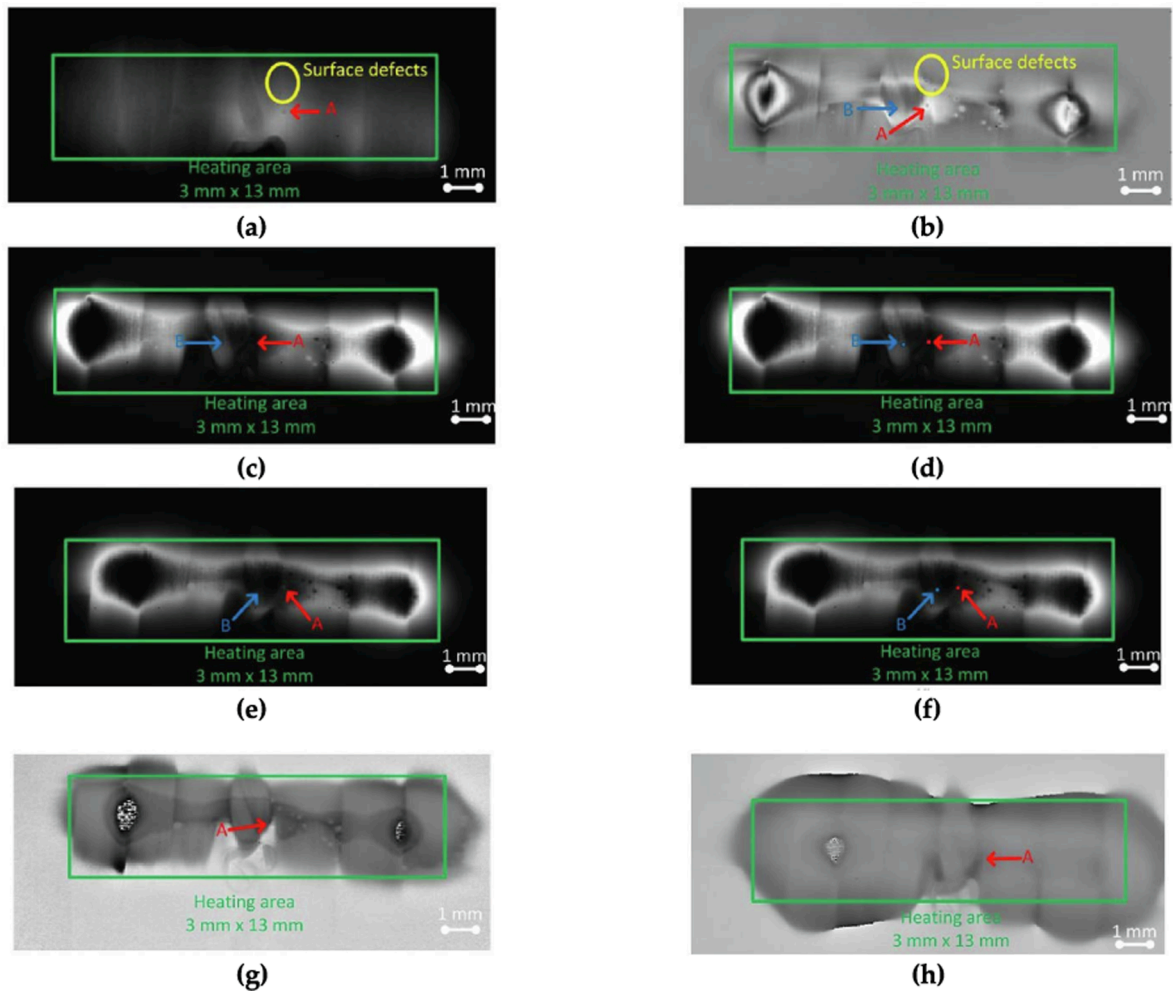


Fig. 20. The micro-LLT results: (a) Pulse: 0.5 s, cold image; (b) Lock-in: 5 Hz, PCT (Empirical Orthogonal Functions (EOF) 8); (c) Lock-in: 5 Hz, FT amplitude; (d) Lock-in: 5 Hz, FT amplitude (defects marked); (e) Lock-in: 1 Hz, FT amplitude; (f) Lock-in: 1 Hz, FT amplitude (defects marked); (g) Lock-in: 5 Hz, FT phase; (h) Lock-in: 1 Hz, FT phase [147].

(Fig. 20), although not clearly as the ones already detected in the raw images [147]. FT in phase can't detect micro porosity B. Micro-LST lock-in shows clearer results (porosity B) compared to micro-LLT lock-in, as shown in Fig. 21 b and c for PCT and FT amplitude but not for FT in phase (Fig. 21 d) [147]. From these results, it seems that the lock-in method can access deeper depth (porosity B) than pulse method for both micro-LLT and micro-LST.

Yang et al. [148], developed a visualization algorithm, using an edge filter, that removes noises and enhances the visualization of micro defects of raw thermal images acquired when a single-spot pulse laser beam excites semiconductor chips and ceramic-epoxy composites. The developed algorithm has the advantages of providing reference-free analysis, and instantaneous and automated

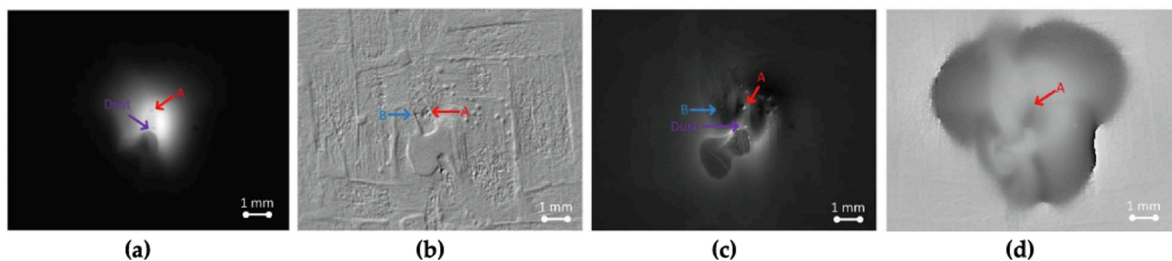


Fig. 21. The micro-LST results (a) Pulse: 0.5 s, cold image; (b) Lock-in: 1 Hz, PCT (EOF 5); (c) Lock-in: 1 Hz, FT amplitude; (d) Lock-in: 1 Hz, FT phase [147].

high-reliability inspection of micro defects, as shown in Fig. 22 (example of images taken from [148]).

Barker code, commonly used in radar systems, comprises binary phase sequence coding group of different lengths and 10 known categories [149,150]. Barker code is generated as a modulated stimulation signal for IR. Bu et al. [149], used Barker Code Laser Infrared Thermography (BCLIT) to inspect a semiconductor Si-wafer with micro-crack defects. The wafer has a diameter of 101.6 mm (4 in.) and thickness of 0.50 mm. The thermal images were processed using Total Harmonic Distortion (THD), with TH_{Dp} - 13-bit Barker code pulse compression waveform, TH_{DA} - peak related side lobe level and F_{peak} - Barker coded discrete autocorrelation function. The inspection area and size of defects, as well as results after algorithm processing are presented in Fig. 23. Another study [151] revealed that Barker-coded thermal wave imaging (BCTWI), with correlation data processing, was able to detect artificial blind holes in mild steel, located at different depths (0.5–2 mm) each having 10 mm diameter or with same depth of 1.5 mm but with different diameters (3–5.5 mm).

Thermoreflectance Thermal Imaging (TTI) is a two-dimensional microscopic technique for reflective surface inspection, as it provides a surface thermal mapping due to the optical reflectance of the inspected surfaces. This technique uses shorter wavelengths than IR for measurement and excitation and can achieve sub-micron spatial resolution between 0.3 and 0.5 μm , in small electronic devices [141,142]. A Charge-Coupled Device (CCD)-based thermoreflectance microscopy system was proposed as a non-contact

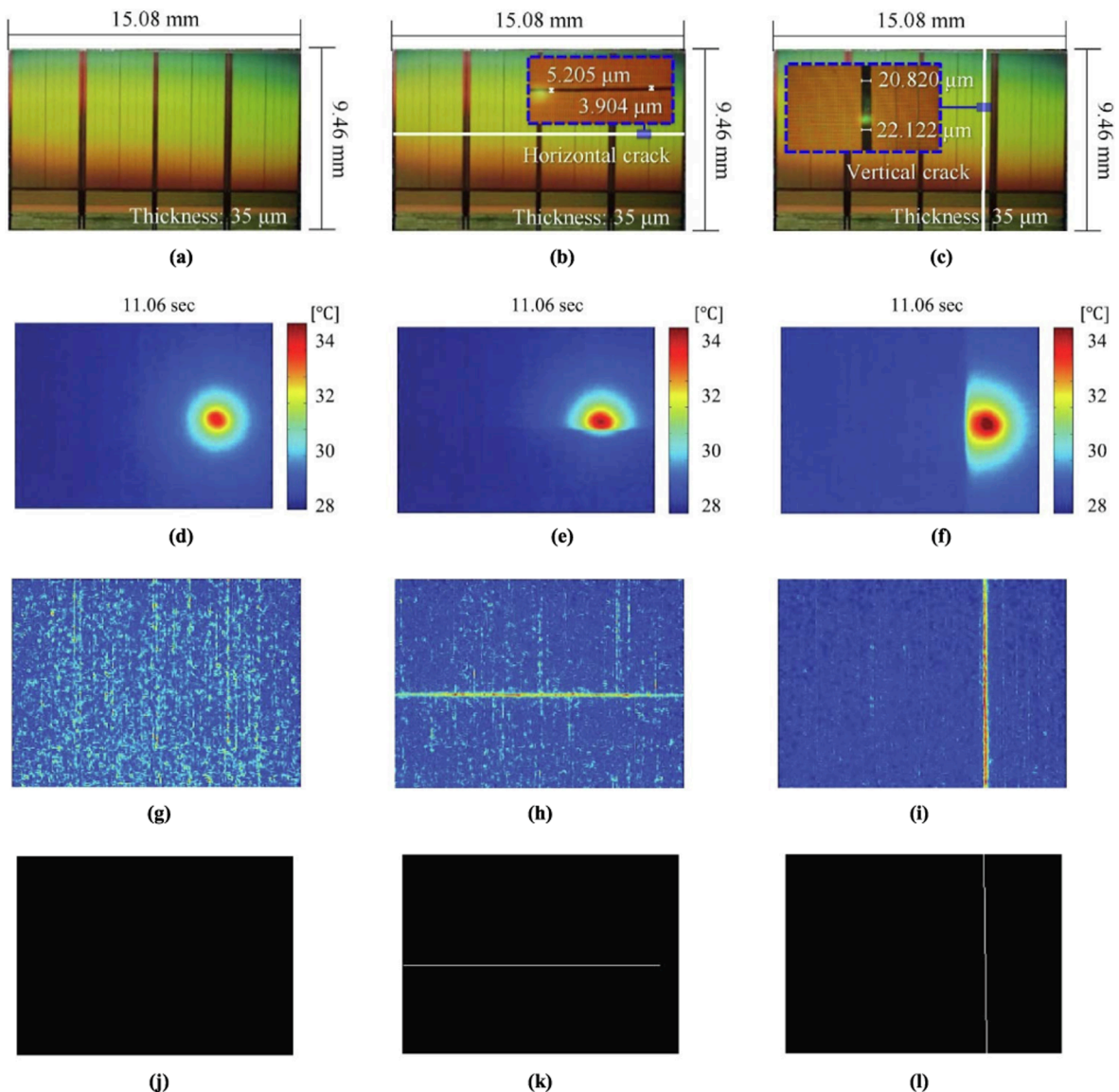


Fig. 22. Reference-free micro defect visualization: (a) Semiconductor chip without defects (sample 1); (b) Semiconductor chip with horizontal defect (sample 2); (c) Semiconductor chip with vertical defect (sample 3). Raw thermal images measured from: (d) Sample 1; (e) Sample 2; (f) Sample 3. The accumulated edge images from (g) Sample 1; (h) Sample 2; (i) Sample 3. The final processed images from the binary images: (j) Sample 1; (k) Sample 2; (l) Sample 3 [148].

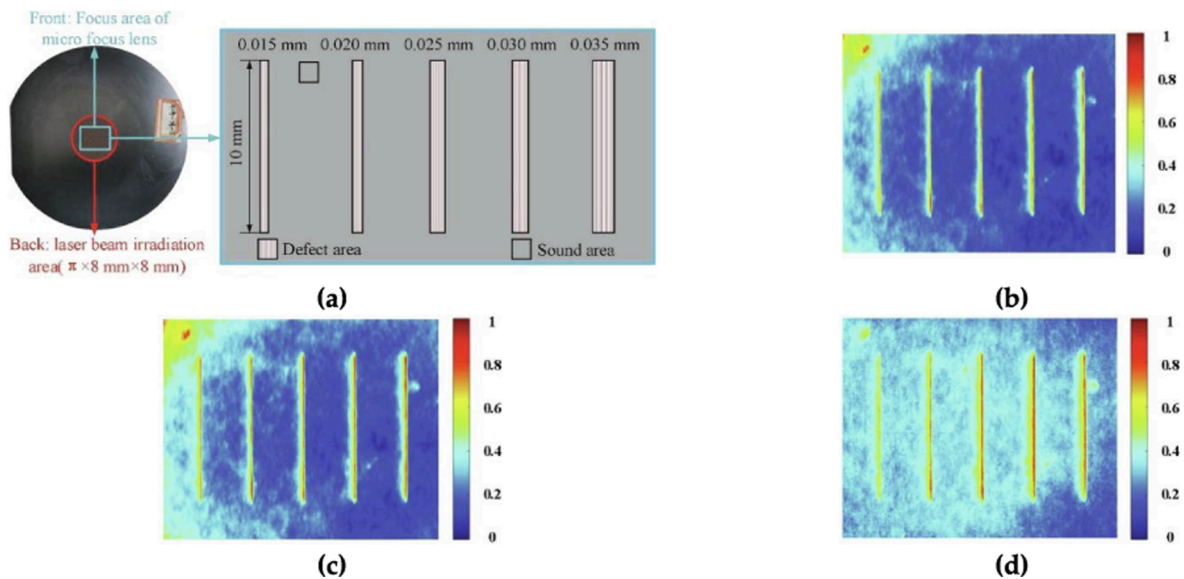


Fig. 23. BCLIT inspection: (a) Semiconductor Si-wafer and defects' parameters; (b) Algorithm processing result of TH D_p ; (c) Algorithm processing result of TH D_A ; (d) Algorithm processing result of F_{peak} . Adapted from [149]

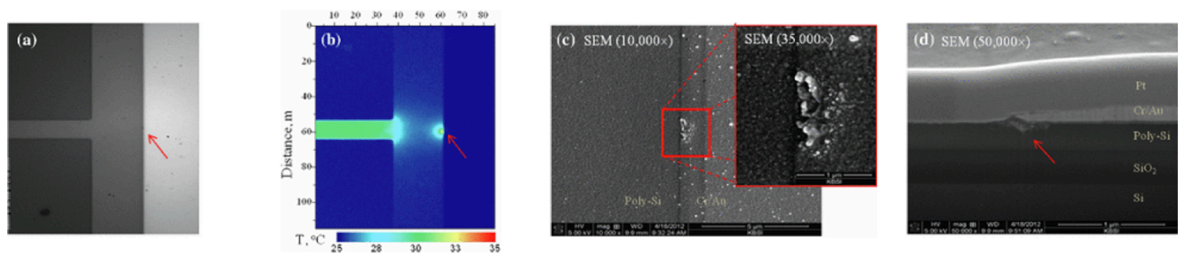


Fig. 24. Results of the inspection of a polysilicon micro-resistor with 10 μm width, and 200 μm length: (a) Conventional microscope image; (b) CCD-based thermoreflectance microscopy image; (c) SEM images (10 000 \times and 35 000 \times); (d) Cross-sectional SEM image (50 000 \times) of the hotspot region [141].

technique to analyse small defects that occur at the interface between the polysilicon resistor and metal contacts [141]. The system was able to identify hotspots related to defects of less than 1 μm , in a polysilicon micro-resistor with 10 μm width, and 200 μm length, as shown by the red arrow in Fig. 24b. Optical microscope and SEM were used to validate the results, as also shown in Fig. 24, although the defect was barely detected with the former.

Another emerging thermal technique is the Scanning Thermal Microscopy (SThM), that uses Atomic Force Microscopy (AFM) probes with a temperature sensor, used for two-dimensional local temperature and thermal conductivity measurements with nanometer spatial resolution [152,153]. When an AFM probe, mounted on a z stage, approaches the sample, a force acting between the tip of the probe and the sample surface causes the probe cantilever to bend, and a light beam, for instance from a LED, reflects from the cantilever and falls upon the position detector. The displacement of the light spot is related to the cantilever bending. An AFM feedback loop corrects the vertical position of the probe to keep the force constant, and the information from this feedback loop during scanning allows the creation of a topographical image of the sample surface [152].

Micro-Raman spectroscopy is a technique that uses scattered light to study the vibrational energy levels of chemical bonds, i.e. the difference between the incident photon and the Raman scattered photon on Raman active materials [154,155]. The technique can characterize residual stresses, thermal conductivity, stacking faults and phase transformation [154,156]. However, it is a time-consuming technique because, like micro-LLT, it inspects each point of the sample rather than scan the complete surface at once. Besides, the technique can't detect subsurface defects [23]. The spatial resolution of micro-Raman spectroscopy is of less than 1 μm and it has nanosecond temporal resolution [156,157]. For example, Pizani et al. [158] used Raman spectroscopy to measure a silicon sample with the surface machined by single point diamond turning. Fig. 25 shows the Raman spectra of the surface before being machined and after being machined in brittle and ductile modes, with evidence that in machining in ductile mode there is a new Raman broad band at about 470 cm^{-1} , which was attributed to a thin amorphous layer at the surface of the sample, with a thickness smaller than the penetration depth of light.

Soudi et al. [159], have combined SThM and Raman spectroscopy to successfully inspect the heat dissipation in GaN nanowires

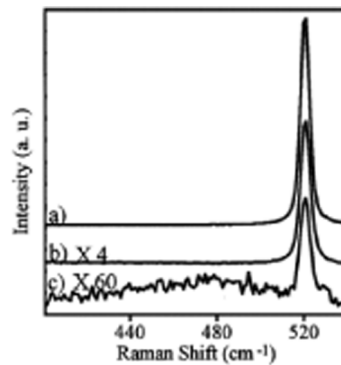


Fig. 25. Raman spectra (performed with wavelength 488.0 nm exciting light) of the silicon sample: (a) Before machining; (b) After machining in brittle mode; (c) After machining in ductile mode [158].

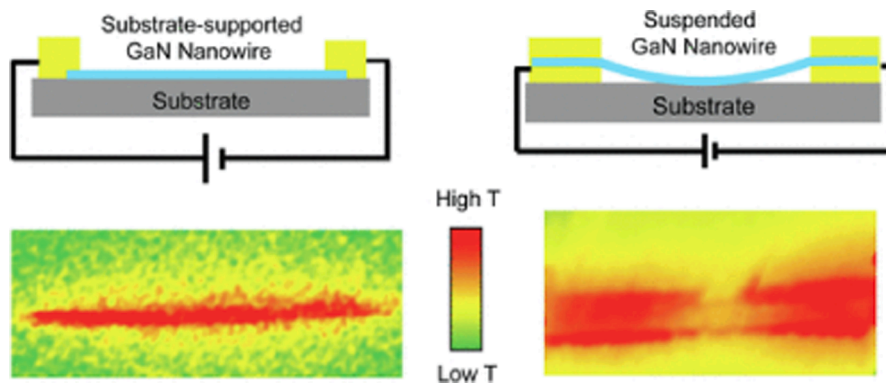


Fig. 26. Schematic representation of a substrate supported and suspended GaN nanowires [159].

with diameters between 40 and 60 nm, shown in Fig. 26. They were able to quantify the contributions from nanowire – substrate and nanowire – electrode thermal transfer to the total heat dissipation, the thermal resistance at their interfaces as well as the nanowire thermal conductivity.

Other commonly used techniques include Frequency Modulated Thermography (FMT) and Golay Coded Thermal Wave Imaging (GCTWI). FMT has been shown to detect defects in mm and cm range [160–163] but has been simulated by Finite Element Method (FEM) (see §10.1) to detect micro defects. GCTWI has also been shown to detect defects in mm range [164–168]. Other thermal techniques, like Ultrasound thermography (see §4.3) and Eddy current thermography (see §6.1), are presented in later chapters.

3.5. Terahertz imaging

Terahertz (THz) are electromagnetic waves, which in the radiation spectrum are located between the microwave and infrared regions, and their wavelengths range from about 0.03 to 3 mm [169,170]. This type of electromagnetic waves started being investigated about 30 years ago, with the establishment of ultrafast lasers that can emit these waves [171].

THz imaging is a non-contact NDT technique, used in applications like aerospace [42], welding [172], biology [173], and semiconductors industry [171], among others. In 2020, Tao et al. [174], wrote a review concerning the many applications of THz imaging. Discontinuities or the dielectric characteristics of a material affect the propagation of the THz signal, whose changes can be detected and recorded using a suitable detector, such as a detection antenna. These waves can penetrate a wide range of materials, like non-metallic materials, insulating materials and opaque materials; have higher spatial resolution than microwave radiation and lower than infrared radiation, although they have more penetration depth; can produce images of the cross-section of layered structures, and are not hazardous for the specimens under investigation, nor the inspectors [175–177].

THz imaging can be divided into Continuous-Wave (CW) THz imaging and pulse THz time-domain imaging. The former is less complex and less flexible than the latter, which may be advantageous in certain applications that don't require a lot of information from the inspection [176].

THz imaging can detect micro defects, such as small protrusions and air gaps, in the micrometer range [174,178]. Costa et al. [178], used a CW THz imaging system composed of a THz source and a detector mounted on a 3D scanner, in a transmission configuration, i. e. the source and detector are placed on opposite sides of the specimen. The inspection was performed by fixing the source and detector, and moving the sample in between them, perpendicular to the beam. The system was able to detect copper wires with different

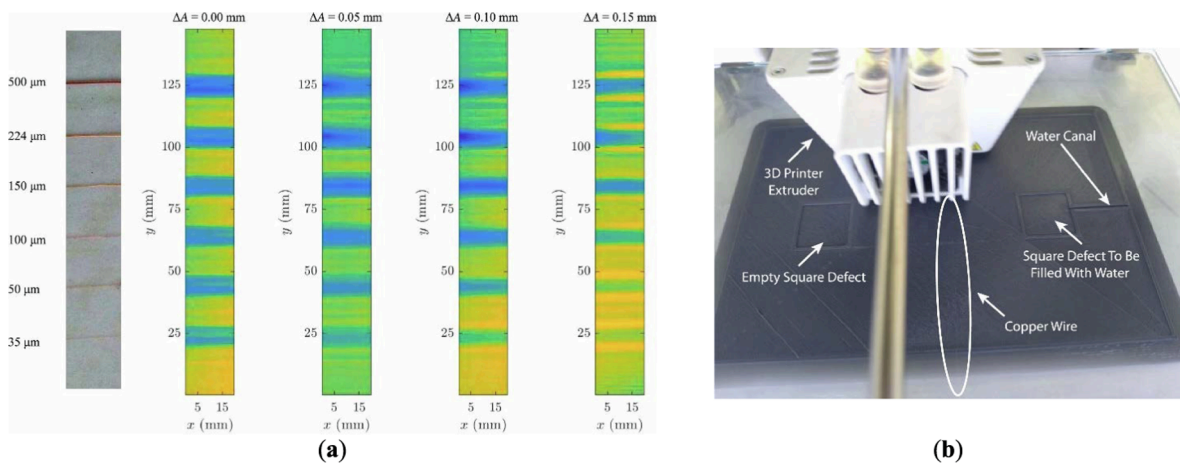


Fig. 27. CW THz inspection: (a) Four C-scans taken at different heights of a sample consisting of six coated copper wires laid on a 7.8 mm thick acrylic sheet; (b) PLA samples with defects shown during 3D printing [178].

Table 3

Value proposition of the different NDT techniques for the analysis of the PLA sample [178].

	Empty Defect	Water infiltration	Metallic wire	Typical time	Health safety
CW THz Imaging	✓	✓✓✓	✓	34x35 min	✓
Air-coupled Transmission UT	✓	✓	X	34 min	✓
Active Transient Thermography	✓	✓*	X	2x2 min	✓
Digital X-ray Imaging	✓✓✓	x	✓✓✓	Instantaneous	x

* Only when close to the surface.

diameters, ranging between 35 and 500 μm, at different inspection heights, as shown in Fig. 27a. To validate the results, an inspection using different NDT techniques was performed in a PLA sample, with artificial defects such as 20 × 20 × 0.5 mm³ square defects, one filled with water, and a copper wire with diameter of 35 μm. The sample is shown in Fig. 27b. Overall, THz radiation presented high reliability compared to other NDT techniques, and both the wires and water infiltrations were detected, as presented in Table 3.

3.6. Interferometry techniques

Interferometry is a NDT method that uses the phenomena of wave interference in a material do detect discontinuities. The working principle consists of splitting the incident light (or radio or sound waves) into two beams that will travel two different optical paths, one through a reference mirror and another through a measurement mirror, and merge later to produce an interference. In the present of a discontinuity, the optical paths of both beams will be different, and the discontinuity can be detected in the interference pattern. Interferometry NDT techniques, like digital holography, electronic speckle pattern interferometry and digital shearography, are used for example in aerospace [177,179], electronics [180], and industrial paints and coatings [181,182]. This group of techniques are of non-contact nature and are able to provide full-field measurements [183].

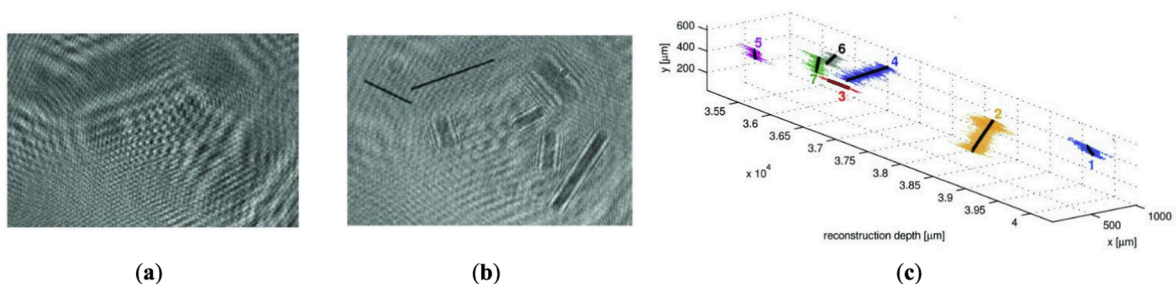


Fig. 28. Digital hologram results: (a) Hologram of a suspension of fibers in liquid; (b) Sample reconstruction; (c) 3D image of a volume of carbon fibers in suspension, viewed from two different directions and showing both the lines fitted by PCA (black lines), as well as the point clouds (colored dots) [188]. Reprinted with permission from [188] © The Optical Society.

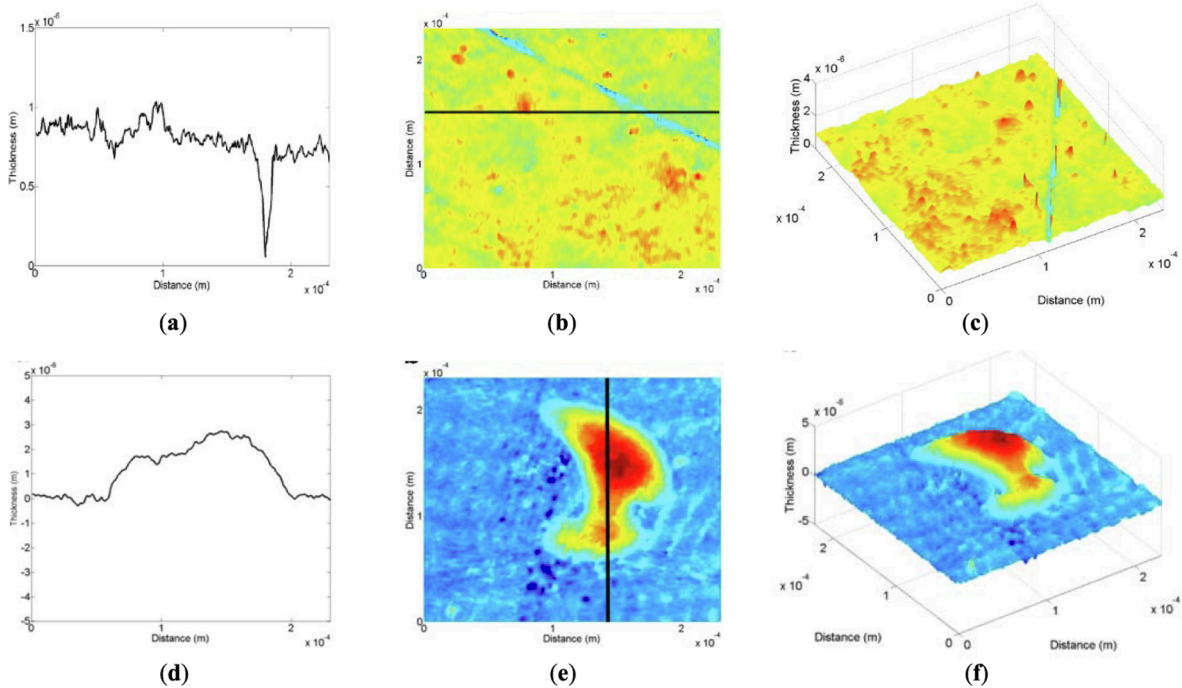


Fig. 29. Digital holography modified LSI results. Reconstructed line-scratch images of the touch-glass panel: (a) 1D image; (b) 2D image; (c) 3D image. Reconstructed dig images of the touch-glass panel: (d) 1D image; (e) 2D image; (f) 3D image [189].

Digital holography is an imaging interferometry technique, which employs two beams of laser light and records the amplitude and phase of light reflected from an object as an interferometric pattern [184]. Digital holography has the advantages of high sensitivity to deformation, in the mm and μm range, and high quality fringes with low speckle noise [185–187]. Rajendran et al. [188], used digital holography to measure the size, orientation, and location of opaque micro-fibers with no a priori information. Fig. 28a and b show the hologram and reconstructed image with focused and out of focus fibers. The resulting 3D image and application of Principal Component Analysis (PCA) allow the identification of the 7 fibers and the measurement of their position, length, and orientation (see Fig. 28c).

Seo et al. [189], proposed a digital holographic microscopy technique based on a modified lateral shearing interferometer (LSI) with a subdivided two-beam interference (STBI), to detect μm and nm defects on transparent target objects. As shown in Fig. 29, the proposed system was capable of detecting the micro and nano defects in a touch-glass panel for mobile displays.

Electronic Speckle Pattern Interferometry (ESPI) is a NDT non-contact interferometry technique where speckle patterns applied to a component are recorded before and after a load or displacement is applied under test. By correlating the speckle patterns to fringe patterns, i.e. contour map of the measurement, and comparing the speckle patterns before and after the test, i.e. subtracting the deformed speckle interferometric pattern with the undeformed speckle interferometric pattern, it is possible to detect discontinuities in the component created due to the load/displacement [183]. This technique employs a single mode monochromatic laser that is split into object beam and reference beam [190]. ESPI has the advantages of high accuracy, full-field measurement and high speed of measurement, and has been shown to detect strain, surface defects and cracks in the mm and μm range [191–196].

Wen et al. [197], used ESPI to inspect artificial edge micro-defects, with length 70 μm and width of about 5 μm , in photovoltaic (PV) cells. By comparing defect-free samples with damaged ones, the authors were able to identify differences in the speckle fringes, as shown in Fig. 30. The speckle fringes for the micro-defect are not continuous across the edge crack and the fringes in the front of the crack tip appear with discontinuous tangential slopes. The interference fringes on the opposite sides of the defect have their own individual concentric fringes (see Fig. 30e and f, compared to Fig. 30c and d).

Additionally, Arai [198], showed that ESPI can be employed to measure the shapes of periodic structures and single silica microspheres beyond the diffraction limit.

Digital shearography is a NDT technique similar to ESPI in the sense that it also detects surface strain through interference of laser speckle patterns. However, shearography only uses one laser beam and doesn't split the beam in order to have a reference beam [183,190]. Shearography has been shown to detect surface and subsurface defects in the mm range [199–205].

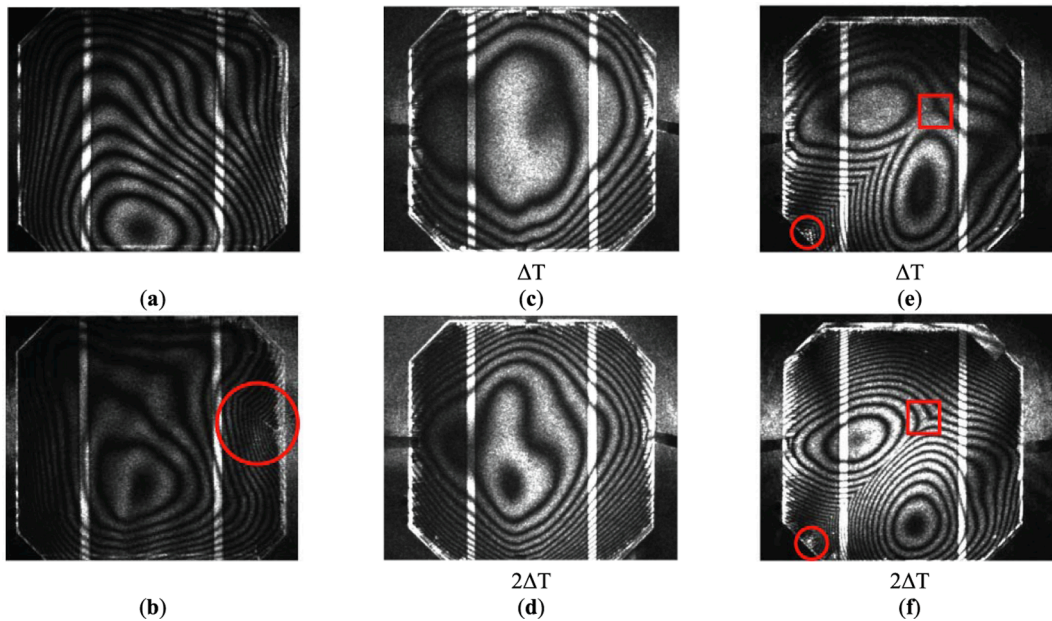


Fig. 30. The out-of-plane ESPI image of a solar cell: (a) Without damage; (b) The same cell damaged with an edge defect appearing inside the circle. The interference fringes were measured in the defect free specimen under different temperature changes: (c) ΔT ; (d) $2\Delta T$. The interference fringes were recorded for the specimen with defects at different temperature changes: (e) ΔT ; (f) $2\Delta T$. The circular and rectangular red regions are the initiating point and arrest point of crack extension, respectively [197].

4. Ultrasonic testing

The Ultrasonic Testing (UT) characterizes the physical condition of an object using high frequency sound waves and can identify surface, subsurface and in volume defects, depending on its variant. The frequencies used for UT are higher than the limit of human hearing, usually between 0.5 and 25 MHz, and the chosen frequency depends on the material being inspected and the information needed [206].

Ultrasonic technology is used in safety and quality-related applications, for example additive manufacturing [207,208], aerospace industry [41,209], weld inspection [210,211], and in the biomedical field for diagnostic imaging and research [212,213].

Ultrasonic waves propagate via the mechanical vibration of the elementary particles that constitute the material. They can propagate through solid, liquid and gas mediums but not through a vacuum. The basic types of sound wave propagation are longitudinal waves, where the trajectory of the waves is parallel to the direction of its oscillation and can propagate through solids, liquids and gases; and transverse waves, where the trajectory of the waves is at perpendicular angles with the direction of its oscillation and can propagate only through solids [214]. In solids, there are more possible modes of wave propagation than in liquid and gas mediums, useful for UT, such as Rayleigh waves (or surface acoustic waves) [215], and Lamb waves (or guided waves) [216]. As the waves propagate in the material, when encountering an interface between mediums with different acoustic properties, there are three possible physical evolutions: (1) part of the sound wave is reflected and part is transmitted to the other medium, establishing a relationship between reflected and transmitted sound energy dependent on the relative acoustic impedance between the mediums; (2) the transmitted energy beam undergoes refraction, with variation in angle and velocity of propagation, and conversion into longitudinal and transversal wave (in the case of solids); and (3) diffraction at the edges of discontinuities, or when the wave encounters a discontinuity (e.g. opened crack) smaller than twice the wavelength of the incident wave [29]. Other characteristics of sound waves are used and explored depending on the purpose of the inspection and material of the specimen, such as attenuation via scattering and absorption phenomena.

The traditional UT equipment is composed of transducers, of which there are many types depending on the incident angle, transmission/reception of the signal, coupling and damping. Piezoelectric-based transducers [217], and Electromagnetic Acoustic Transducers (EMAT) [218], are the most commonly used. Different types and combinations of these transducers have been developed as dedicated solutions for the inspection purpose [219,220]. The equipment is also composed of a pulser emitter/receiver, that is an electronic device that produces high-voltage electrical pulses (e.g. for piezoelectric-based transducers at a frequency near the resonance frequency of the piezoelectric element), and a signal analyser for display of results. In the case of piezoelectric-based transducers, during the inspection, these are typically separated from the object by an ultrasonic couplant, which facilitates the transmission of the energy between the transducer and the object, to minimize attenuation effects and changes in acoustic impedance.

Besides the conventional application of UT with normal and angular piezoelectric transducers, this technique encompasses many different variants, namely: Creeping, Phased Array (PA), Guided Waves, Time of Flight Diffraction (ToFD), Air-coupled Ultrasound, Laser Ultrasound and Scanning Acoustic Microscopy (SAM).

Type of defects		Inclusions		HTHA							
				HTHA 1 Early stage (grade b)		HTHA 2 Moderate (grade b)		HTHA 3 Confirmed (grade c)		HTHA 4 Severe (grade d)	
Defects size (μm)		avg. ϕ	\pm	avg. ϕ	\pm	avg. ϕ	\pm	avg. ϕ	\pm	avg. ϕ	\pm
		35	15	10	5	35	20	380	120	> 500	NA
Detectability	PA LIN LW 0° 7.5 MHz					(1)					
	LW 0° 10 MHz										
	TFM 7.5 MHz										
	TOFD 4 MHz										
	TOFD 7.5 MHz										

	Detectable : Signal to noise ratio >12dB
	Not detectable: Signal to noise ratio <12dB
(1)	Detectable with optimized probe characteristics and tuning

Fig. 31. Results obtained for different UT techniques from inspection of High Temperature Hydrogen Attack (HTHA), at different damage stages, on samples taken from reactor shells (material A204 Gr B) [223].

Among UT’s typical advantages are the wide testing range of applications, including the inspection of thick metallic samples, with three-dimensional positioning of imperfections, and possibility of automated inspection. However, this NDT technique is sensitive to the coupling conditions, material’s internal features, such as grain size, microstructural texture in metals, attenuation in polymers and powder metallic-based components, and the defect size needs to be some orders bigger than the wavelength used to be detectable with reflected waves [29,221].

Kim et al. [222], conducted Ultrasonic Phase Velocity (UPV) measurements, in a pulse-echo configuration, to correlate the UPV with the pore number density, size, aspect ratio, and texture at low porosity levels (0–5%), in $5 \times 5 \times 5 \text{ mm}^3$ stainless steel 316L samples produced by Laser Powder Bed Fusion (LPBF). The results were also validated using X-ray CT, Electron Backscatter Diffraction (EBSD), and uniaxial tensile tests. The results indicate that there is a dependence between UPV and pore shape, porosity density and texture, which depends on the hatch spacing of the additive manufacturing process, and UPV can distinguish between texture and different pore aspect ratios as well as differences in number density of pores. Additionally, the uniaxial tensile tests indicate that yield strength, ultimate strength and elongation are sensitive to hatch spacing and orientation, and UPV could distinguish between different directions of the imperfections.

Le Nevé et al. [223], compared the capability of different UT techniques to detect High Temperature Hydrogen Attack (HTHA) damage on samples taken from reactor shells (material A204 Gr B). The techniques employed were PA, TOFD and Total Focusing Method (TFM). The results obtained are summarised in Fig. 31. Only TFM and TOFD 7.5 MHz are able to detect early damage.

4.1. Scanning acoustic microscopy

Scanning Acoustic Microscopy (SAM) is an imaging technique where its images are formed by changes in elasticity, density and acoustic damping of the sample rather than the reflection, transmission or diffraction of electromagnetic radiation (light in the case of optical microscopy) [224]. SAM allows the detection and visualization of surface and subsurface discontinuities and inclusions, can provide high-resolution three-dimensional information of the discontinuities in a material at sub-micron thicknesses, and has high detection efficiency. It is a suitable NDT technique for small complex devices, for example, electronic devices [46,225], and structural materials such as metals, ceramics, and composites [226]. SAM is also an appropriate technique for quick identification and localization of defects in multi-layered structures but it is typically limited to thin samples [227]. Moreover, it is expensive, time-consuming and a complex technique that requires skilled operators. SAM has a low lateral resolution (as opposed to great resolution in-depth direction) and is highly dependent on surface condition [23,225].

In reflection mode, SAM can detect laminar cracks with less than 50 μm and voids as small as 125 μm in diameter [46]. Fig. 32 shows an example of SAM inspection, via C-scan, of the top layer and interface layer of an adhesive composite structure. The surface presents no defects although the epoxy-metal interface layer shows incomplete adhesion (marked by the arrows) due to adhesive sub-curing and density variations [228].

Zhang et al. [229], proposed a sparse reconstruction technique for the detection of micro defects using SAM, which proved to improve the detection accuracy and Signal-To-Noise (STN) ratio compared to the original C-scan, as shown in Fig. 33. The sample dimensions are about $10 \text{ mm} \times 10 \text{ mm} \times 500 \mu\text{m}$ and the artificial microdefect was etched with the depth of about 50 μm by inductive couple plasmas (ICP) etching. The frequency used was 230 MHz and the step length of the scanning imaging used was 1 μm . The Target-to-Clutter Ratio (TCR) evaluates the effect of deblurring after the ideal image is calculated by the algorithm. The authors also

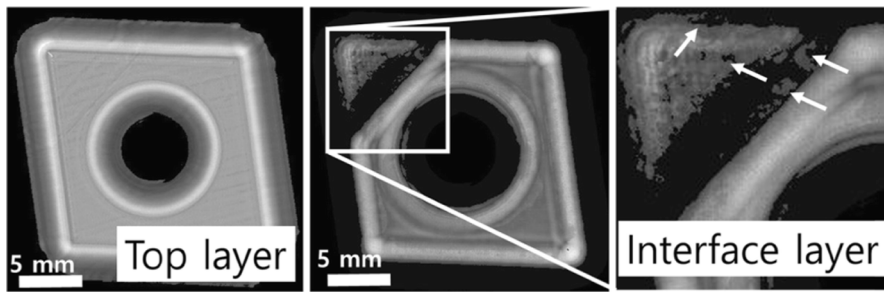


Fig. 32. Images of adhesive joints of tungsten carbide inserts obtained from a C-scan using SAM. Incomplete adhesion is indicated by arrows in the image of the interface layer (right) (110 MHz transducer, lateral resolution of about 15 μm , 512×512 px) [228].

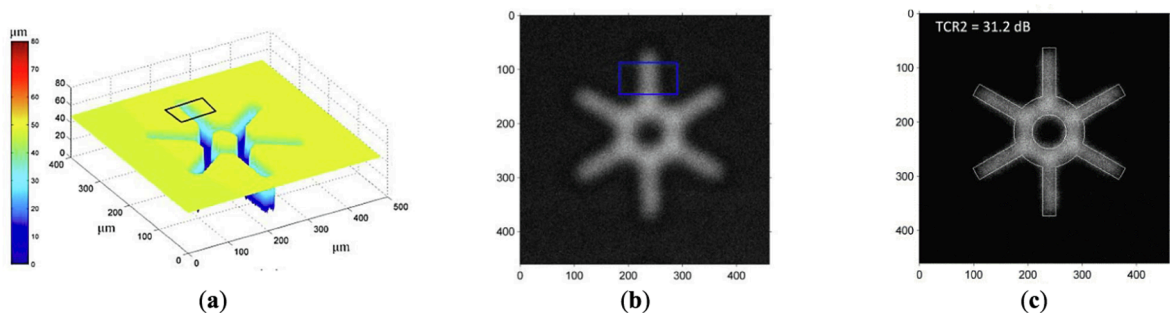


Fig. 33. Results of complex defect inspection using SAM (unit in μm): (a) The topography of the defect measured by laser scanning confocal microscopy; (b) Original C-scan image; (c) The reconstructed image superimposed with the mask [229].

proposed a sparse reconstruction method based on the blind estimation (post processing algorithm) for the detection of micro defects [230]. The sample dimensions are $1 \text{ mm} \times 1 \text{ mm} \times 500 \mu\text{m}$ and the artificial microdefect was also created using ICP. The frequency used was also 230 MHz and the step length of the scanning imaging used was also $1 \mu\text{m}$. The results show that compared to the original C-scan image after imaging process (Fig. 34a) and non-blind estimation image (Fig. 34b), that the blind sparse reconstruction method (Fig. 34c) had an improved resolution of 39.2% and 3.9%, respectively.

4.2. Guided waves, electromagnetic acoustic transducer and ultrasonic phased array

Ultrasonic guided waves can travel long distances without suffering much signal attenuation, because of being confined by the boundaries of a structure, enabling to inspect long sectors of tubular components including curved zones [231]. Guided waves are Lamb waves, used for NDT at frequencies between about 50 kHz and 10 MHz, for example, to detect microcracking at the surface of a material: it has been shown to work for a triangular notch with 15 mm in base and 25 mm in height [232], to evaluate the surface properties of components coated by electrodeposition [233], or for corrosion screening [234]. These types of waves enable the detection of imperfections in full thickness, but the omnidirectional dissemination disable to localize or characterize the imperfections.

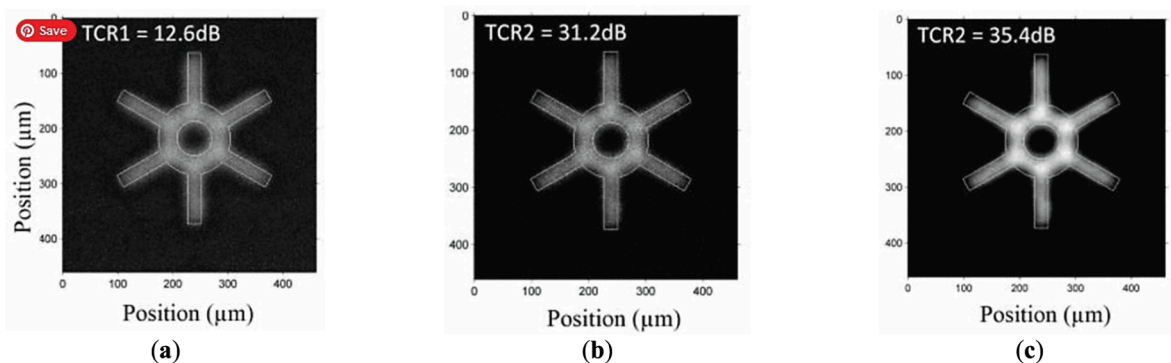


Fig. 34. TCR comparison of different processing of SAM inspection image: (a) Original C-scan after image processing; (b) Nonblind sparse reconstruction image (corresponds to Fig. 33c); (c) Blind sparse reconstruction image [230].

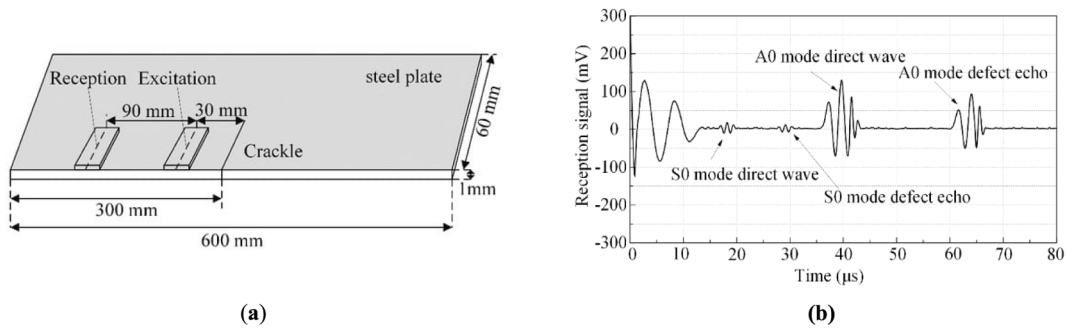


Fig. 35. High-Energy Pulse EMAT Defect Detection: (a) Schematic view of the steel and defect; (b) A0 and S0 modes Lamb waves defect detection [237].

Electromagnetic Acoustic Transducer (EMAT) is a hybrid technique merging fundamentals of conventional UT with Eddy Current Testing (ECT) technique (see §6.1), that generates and receives ultrasound waves in conductive materials. When a high frequency Alternating Current (AC) flows through a planar coil positioned in the vicinity of the surface of components to be inspected, a primary magnetic field is induced. This primary alternating magnetic field generates an opposing secondary magnetic field and the inherent eddy currents in the surface of the specimen. These eddy currents interact with the bias static magnetic field from the EMAT permanent magnet and generate an alternating Lorentz force, normal to the eddy currents and the bias magnetic field, which produces sound waves in the specimen. The signal pick-up by the transducer is obtained from the ultrasonic waves interacting with the bias magnetic field, affecting the primary alternating magnetic field and inducing a modification of the impedance across the coil terminals. EMAT does not require direct contact, neither couplants [235,236].

Liu et al. [237], developed a high-energy acoustic excitation system without a static bias magnetic field, common in conventional EMAT, which has a reduced transducer size with higher ultrasonic signal intensity, and can detect high-temperature steel plates at higher lift-off distances. Instead of the static bias magnetic field, it is used a LC oscillator circuit, composed of inductive coil L and a capacitor C, that generate the dynamic magnetic field, which combined with the pulsed eddy currents, generate the Lorentz force.

The authors inspected a $600 \times 60 \times 1 \text{ mm}^3$ steel plate with a crack defect with 0.4 mm width, 30 mm length and 1 mm depth (see Fig. 35a) and concluded that antisymmetric (A0) mode Lamb waves have higher STN ratio than the symmetric (S0) mode Lamb waves and can accurately locate the crack, as shown in Fig. 35b.

Park et al. [238], used nonlinear ultrasonic guided waves generated by EMAT to qualitatively detect micro defects in three different steel wire rods, SWOSC-V, SWOSC-VHV and SWOSC-VHS, with diameter of 3.2 mm and length of 322 mm. This technique identifies changes in material properties and micro defects through harmonic components, dissimilar to the conventional technique. The authors inspected 9 rod wires, three per material. Fig. 36 shows the results of comparing the relative nonlinearity of each material, which according to the authors tends to increase with increased propagation distance (between 1 and 60 and 121–180 mm). In the case of SWOSC-V, it decreases with propagation distance of 181–240 mm because of the material properties. However, it can be seen in Fig. 36b that SWOSC-VHV #2 has a different tendency than SWOSC-VHV #1 and #3 wire rods, which indicates some irregularity inside the material that is further proved by experiments that indicate micro defects in SWOSC-VHV #2 at a propagation distance of 180 mm and by acquiring SEM micrographs of wire rods SWOSC-VHV #1 and #2, shown in Fig. 37.

Isla et al. [239], presented an 8-element EMAT phased array, operating at 1 MHz and generating shear waves at about 60° angle, that can detect defects in surfaces opposite to the array transducer’s interacting surface. These small surface cracks can be found in welded components submitted to fatigue. The probe consists of a permanent magnet and a coil, whose schematic representation is shown in Fig. 38 and prototype is shown in Fig. 39a. The coils of the array overlap under a ferromagnetic core, which is bordered by magnets with like poles facing the core to increase the magnetic flux density [239,240]. The experimental setup performed on an aluminium block with a slot in the opposite wall, with 0.2 mm width and 0.8 mm depth, is shown in Fig. 39b. The closest coil of the

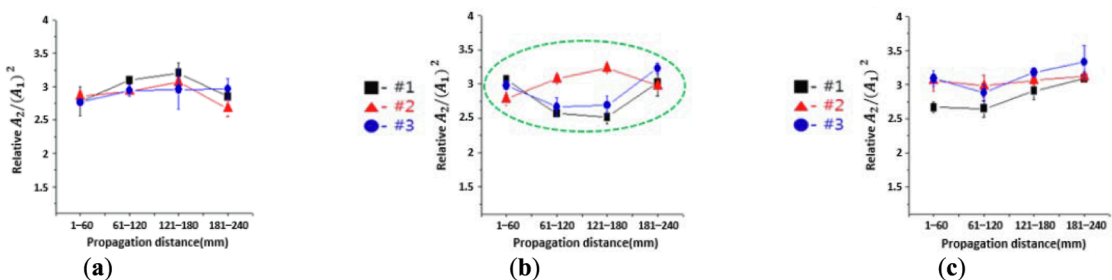


Fig. 36. Relative nonlinearity for each detection area (a) Results of the three-specimen test in SWOSC-V; (b) Results of the three-specimen test in SWOSC-VHV; (c) Results of the three-specimen test in SWOSC-VHS [238].

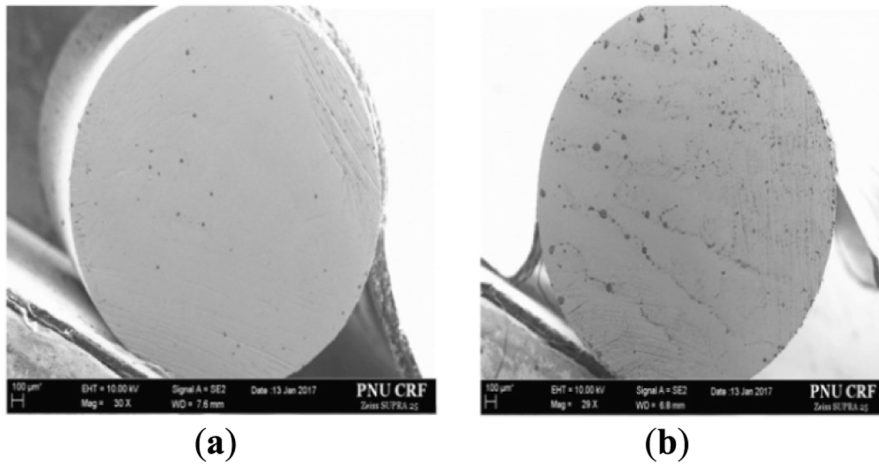


Fig. 37. Comparison of SEM micrographs for steel wire rods: (a) SWOSC-VHS #1: non-defect area; (b) SWOSC-VHS #2: defect area [238].

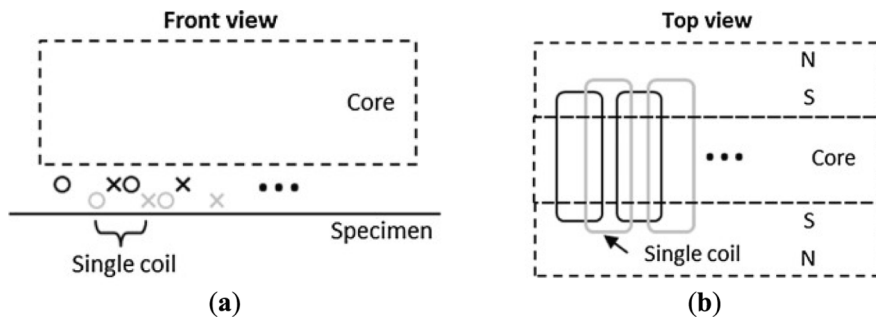


Fig. 38. Sketch of proposed EMAT array showing the overlapping pattern of the coils and the ferromagnetic core abutted by magnets with like poles facing the core: (a) Front view; (b) Top view. The circles and crosses in the top view indicate that the currents in the coils leave and enter the plane of the figure respectively [239].

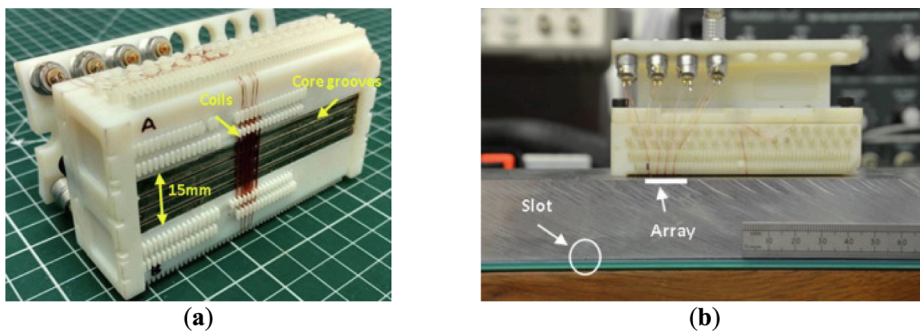


Fig. 39. An 8-element EMAT phased array: (a) Prototype; (b) Experimental setup placed over an aluminium block with a slot of 0.2 mm width and 0.8 mm depth on the back wall [239].

array to the slot is 22.5 mm. Fig. 40 presents the simulation and experimental results obtained.

Phased Array Ultrasonic Testing (PAUT, or simply PA) is a NDT technique where the transducer is composed of multiple small elements, each being excited or pulsed individually. The excitation can be simultaneous for normal inspection, or with constant or continuously variable time delay for angular scans. The period of each pulse for delayed excitation is set according to the wave velocity, frequency, size of the element and focal domain and position, enabling e.g. to modify the inspection domain, with same PA transducer [241]. This technique can be used to inspect complex geometries, in a variety of different materials, and can create detailed cross-sections of a component.

Wang et al. [242] proposed a phased array ultrasonic testing, with high detection accuracy and resolution, to characterize sub-millimeter artificial deep bottom holes, with 0.8 mm diameter and 5.0 mm depth, in additive manufactured TC18 titanium block.

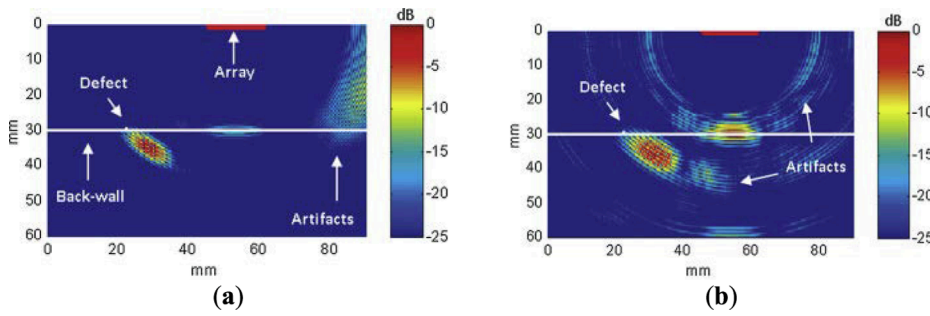


Fig. 40. Focused image that corresponds to a 30 mm aluminium block that has a slot (defect): (a) 2D simulation; (b) Experimental results. The array consists of 8 elements, which have a width of 3.2 mm and a pitch of 2.1 mm. The central frequency of the excitation is 1 MHz. The white and red horizontal lines correspond to the back wall of the aluminium block and the location of the array respectively. [239].

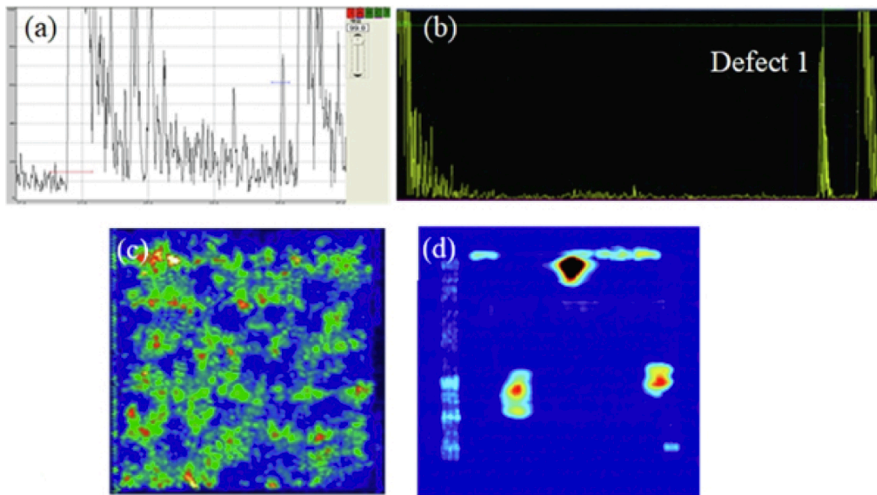


Fig. 41. Detection results by conventional UT and linear array PA on printed TC18 titanium block surface: (a) A-scan of conventional UT; (b) A-scan of linear array PA; (c) C-scan of conventional UT; (d) C-scan of linear array PA [242].

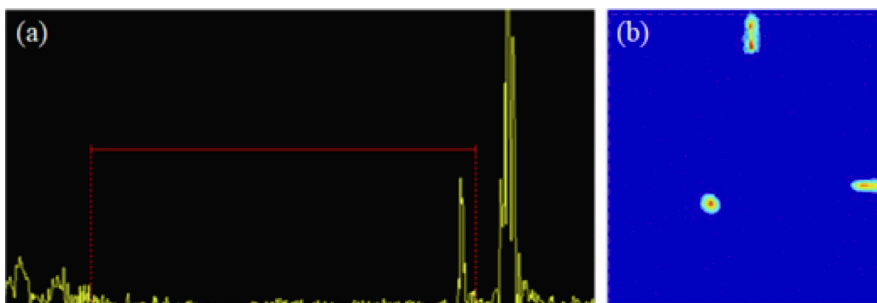


Fig. 42. Detection results by annular array PA on printed TC18 titanium block surface: (a) A-scan; (b) C-scan [242].

Both linear and annular array transducers (with a ring circular shape) are used, the latter integrated with a TFM-based post-processing algorithm. As shown in Fig. 41, linear array PA performed better than conventional UT, that can't characterize the defects due to high attenuation characteristics of sound waves in the additive manufacturing titanium block. Annular array PA presented higher detection accuracy (i.e. higher STN ratio) and resolution than the linear array PA, as shown in Fig. 42 [242].

Javadi et al. [243], inspected aluminium samples with 20 layers and 300 mm long, made by Wire Arc Additive Manufacture (WAAM), having artificial drilled-holes with 0.5 to 3 mm in diameter, using 5 MHz and 10 MHz PA transducers in conjunction with the TFM. The system was able to detect holes down to 0.5 mm in diameter and up to 45 mm deep, as shown in Fig. 43.

Li and Cho [244], proposed a nonlinear Rayleigh surface wave tomographic technique that combines nonlinear ultrasonics and guided wave tomography for locating, sizing and imaging micro defects. The authors inspected $500 \times 500 \times 10$ mm³ aluminium

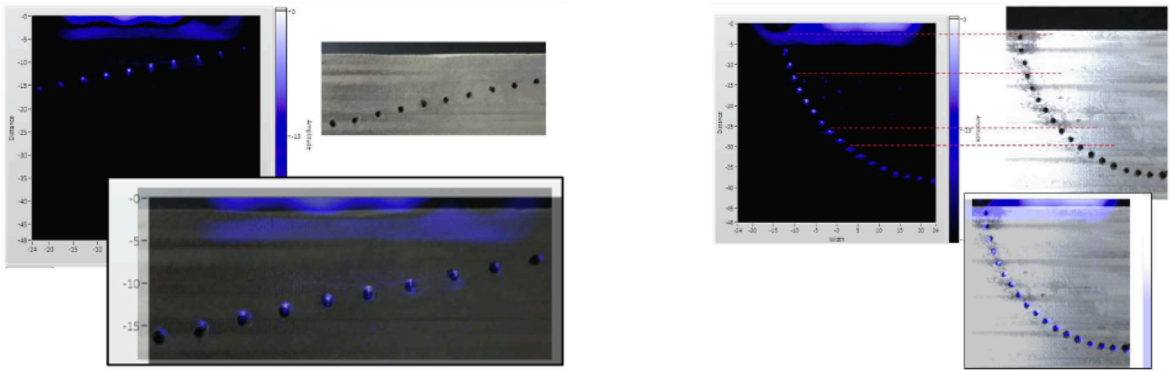


Fig. 43. Near-surface defects scanned by the 10 MHz array placed over the WAAM top surface [243]. This illustration first appeared in the paper: 'Ultrasonic phased array inspection of wire + arc additive manufacture samples using conventional and total focusing method imaging approaches', by Y Javadi et al, Insight, Vol 61, No 3, pp 144-147, March 2019 and is published here with the kind permission of The British Institute of Non-Destructive Testing and the authors.

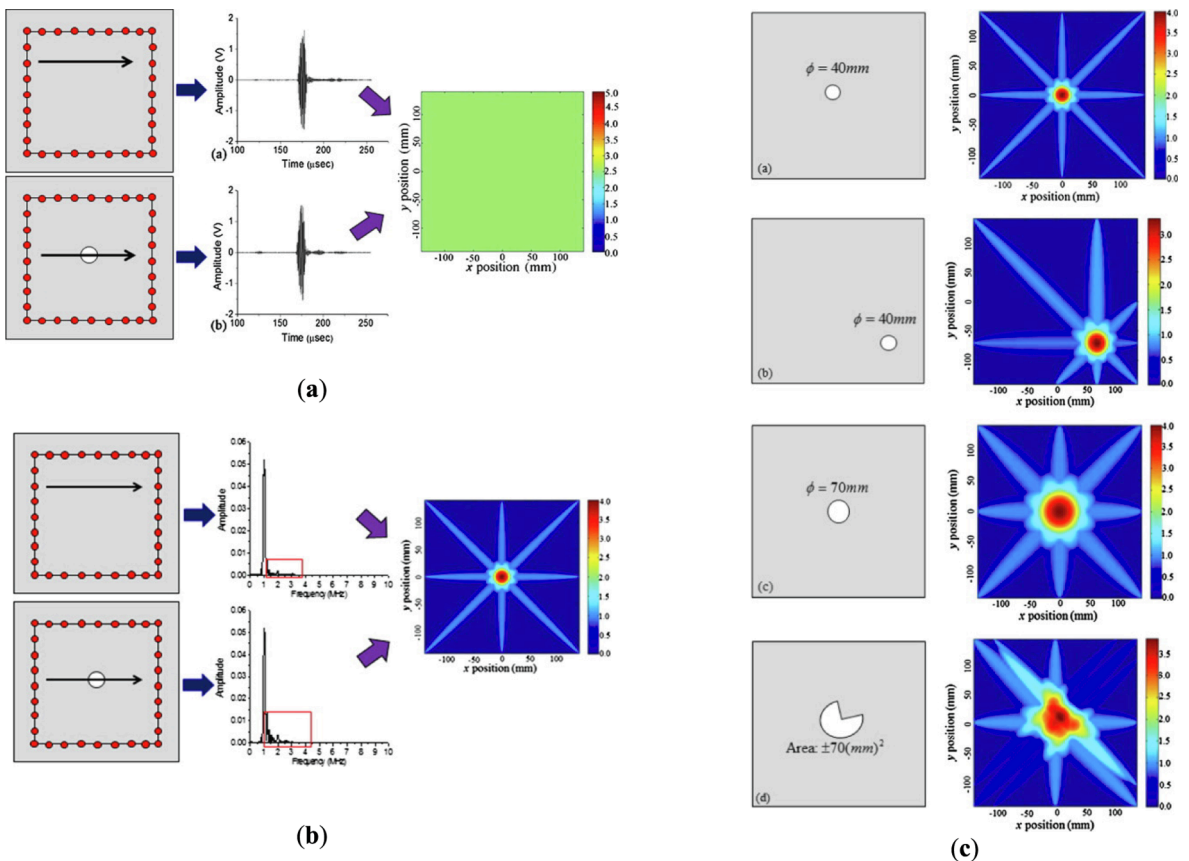


Fig. 44. Results from: (a) Conventional ultrasonic tomography based on linear time domain signals; (b) Modified nonlinear ultrasonic tomographic image based on frequency domain signals; (c) Modified nonlinear ultrasonic tomographic image based on frequency domain signals of different damaged regions with different location, size and shape [244].

plates, each with one artificial chemical corrosive area whose diameters range between 40 and 70 mm, as shown in Fig. 44. Each damage area contains micro-pits and cavities with sizes in the order of 10 μm . As shown in Fig. 44, the new technique successfully characterizes the damaged region, which is the main source of nonlinearity, when compared with conventional linear ultrasonic tomography.

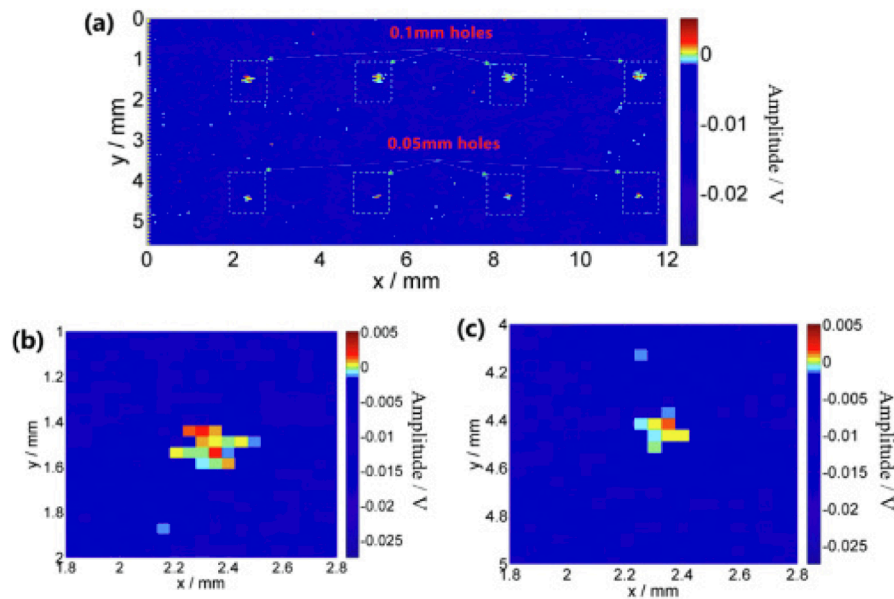


Fig. 45. Laser ultrasonic testing C-scan imaging of the array holes at $t = 0.83 \mu\text{s}$: (a) C-scan image of all holes; (b) Image of hole with diameter of 0.1 mm; (c) Image of hole with diameter of 0.05 mm [248]. Reprinted with permission from [248] © The Optical Society.

4.3. Laser ultrasonic testing, advanced ultrasonic backscatter and other ultrasonic imaging techniques

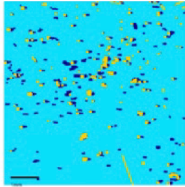
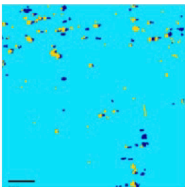
Laser Ultrasonic Testing (LUT) is a non-contact NDT technique for surface characterization where a laser Doppler interferometer is used to produce and measure ultrasonic waves in components. The focal diameter of the laser beam is smaller than the ultrasonic wavelength which enables the acquisition of acoustic field information in the presence of small discontinuities [245]. The technique can be used in high-temperature applications, such as welding, and for irregular geometries and restricted areas through fibre optics. It can also detect very small defects due to its high frequency, e.g. 50 μm artificial flat-bottomed holes in a 0.3 mm thick aluminium sample [246]. However, the technique only works for thin subsurface layers and is highly influenced by the state of the surface and microstructure [2,247].

Yang et al. [248], inspected $30 \times 30 \times 5 \text{ mm}^3$ AISI 316L stainless steel samples produced by SLM, with surface defects and different surface roughness, using laser ultrasonic C-scan imaging system. The steel powder diameter ranged between 30 and 60 μm . As shown in Fig. 45, the technique was able to detect the surface defects, which consisted of artificial notches made by Electron Discharge Machining (EDM) with width and depth ranging between 50 and 100 μm , and a length ranging between 1 and 3 mm.

Smith et al. [249], inspected $10 \times 10 \times 10 \text{ mm}^3$ titanium alloy samples produced by SLM with a powder size ranging between 15

Table 4

Pore size results from 140 W and 190 W samples [249].

SLM laser Power (W)	Difference Plot of Pores	Mean pore diameter (μm)	Standard Deviation of pore diameter	Total Pore Count	
140	Optical		115	44	126
	Velocity		137	56	182
190	Optical		119	47	70
	Velocity		134	63	95

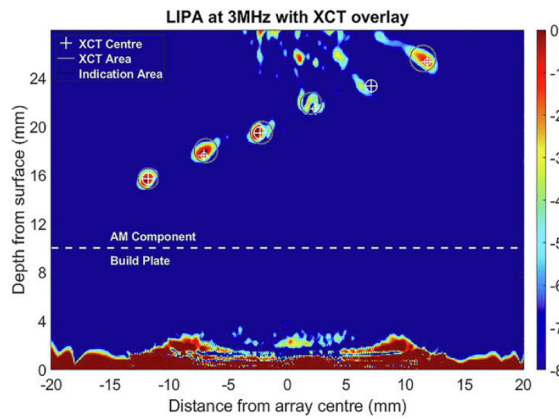


Fig. 46. Normalized TFM image using shear-shear wave arrival. Black circles mark the centre of the indications and are proportional to the area. White cross hairs mark the centres located using CT and white circles represent the area based on the XCT measured diameter. The white dashed line illustrates the separation between the build plate and the part built on top of it [250].

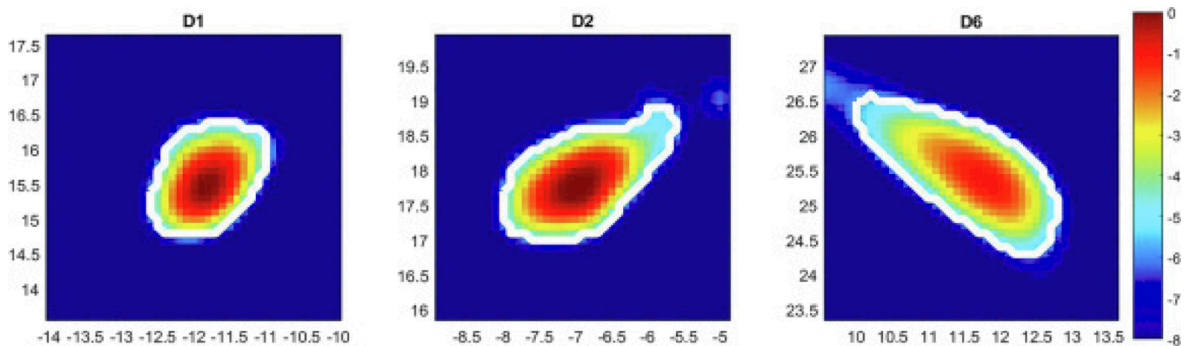


Fig. 47. Close-up TFM images of Fig. 46, showing mock side drilled holes: D1, D2 and D6. A 3 MHz digital filter was used for all figures and the dynamic range is shown (dB scale). The white outline shows the boundary of -6 dB drop in image pixels [250].

and $45 \mu\text{m}$, using Spatially Resolved Acoustic Spectroscopy (SRAS) which uses surface acoustic waves. The technique allowed the identification of surface and subsurface defects (porosity) with sizes between 134 and $137 \mu\text{m}$, as summarized in Table 4.

Pieris et al. [250], inspected a $20 \times 40 \times 10 \text{ mm}^3$ AlSi10Mg sample produced by SLM, with holes up to 26 mm in depth with diameters of 0.2 mm and 0.7 mm , using Laser Induced Phased Arrays (LIPA). Fig. 46 shows the normalized TFM image using shear waves (3 MHz frequency, effective wavelength of 1 mm in aluminium) and Fig. 47 shows a close up of features D1 (0.7 mm in diameter, 2 mm in depth), D2 (0.2 mm in diameter, 2.8 mm in depth) and D6 (0.2 mm in diameter, 3.4 mm in depth). The discrepancy between the CT and LIPA measurements is due to having regions of low sensitivity due to the angular dependency of the shear wave and because of the sample's internal roughness. LITA can detect very small defects but can't properly size them, as shown in Fig. 46.

Additionally, Guo et al. [251], studied the mechanism controlling the interaction between LUT waves and micro defects on an aluminium plate via numerical simulation and experiments, providing information on the relationship between defect depth and signal

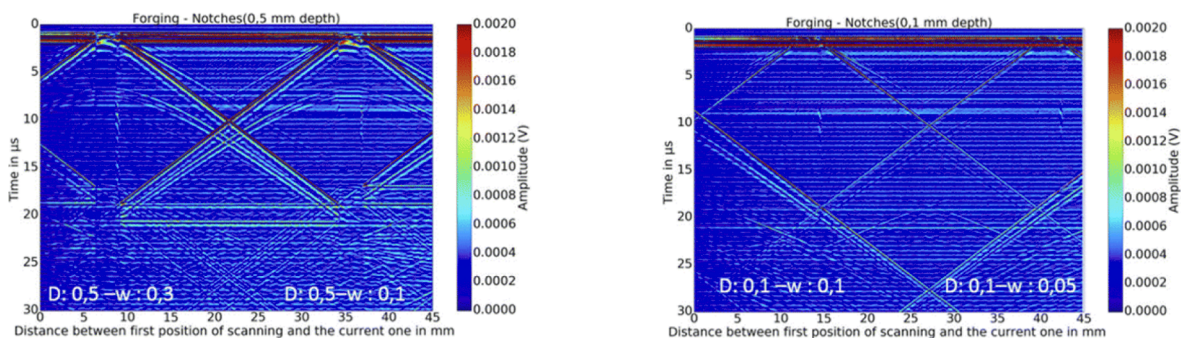


Fig. 48. LUT B-scans for AM samples (D stands for depth and w stand for width) [253].

amplitude. Manzo et al. [252], developed a LUT system with laser heterodyne displacement sensing that was able to detect holes of size between 10 and 20 μm . Millon et al. [253], inspected surface notches created by EDM on $80 \times 20 \times 25 \text{ mm}^3$ additive manufactured 316L stainless steel sample by means of LUT. The smallest detectable defect has a depth of 100 μm and a width of 50 μm , as shown in Fig. 48.

Advanced Ultrasonic Backscatter Technique (AUBT) is a tool used to inspect microstructural features like grain boundaries, inclusions, cavities and microcracks, because they reflect the ultrasonic wave, and through frequency analysis, it's possible to understand the state of the material [2]. There exist several ways to establish the cause of backscattering signals, such as velocity ratio, spectral analysis, spatial averaging and frequency-dependent backscatter. One example of the use of this variant is for the inspection of micro defects in areas affected by hydrogen attack [254]. Similar to LUT, the technique only works for thin subsurface layers and is influenced by the state of the surface and microstructure, and is reported to only detect HTHA defects bigger than 500 μm [2,223].

Ultrasonic Infrared Thermography (UIT), also known as thermosonics or vibro-thermography, is a thermographic technique where vibrations are induced in a sample that cause frictional heating and allow to identify defects using an infrared camera [40,255–257]. Park et al. [258], used Ultrasound Lock-in Infrared Thermography (UIRT) to detect SCC micro defects in a nuclear power plant pipe welded with dissimilar metals, carbon steel SA106 B Gr. b and stainless steel STS 304. UIRT uses lock-in thermography, including an infrared camera, alongside an ultrasonic vibrator (output of 250 W and frequency of 19.8 kHz), and the experiments were performed inside an insulated chamber. The pipes rotated in four directions by 90° during the inspection. The ultrasound tool contacted the upper part of STS 304 and vibrated at 50 mHz for 3 min. Fig. 49 shows the results for the directions 0° and 90° . At 0° and 90° , hot spots (D1 and D2) are detected. In Fig. 49c and d, temperature graphs of before and after ultrasonic vibration is applied are presented, evidencing that the hot-spot patterns in the UIRT images were produced based on the detection of actual temperature differences caused by the ultrasonic vibration.

Favro et al. [259], employed high frequency pulsed UIT to detect small fatigue cracks (0.8 mm long) in aluminium (Fig. 50a) and delaminations in a CFRP composite (Fig. 50b).

Ni et al. [260], combined an interference-based image acquisition method with a joint image reconstruction algorithm that they claim can achieve accurate ultrasound images at 250 μm resolution with strong SNR and structural similarity index (SSIM) of 0.998. Fig. 51 shows results of different techniques used to inspect a nylon wire, including the proposed novel technique. Fig. 51a-c have side lobes caused by reflections of ultrasound waves that affect the image scanline during the beamforming operation, contrary to the image of the novel technique (Fig. 51d), that was reconstructed using data from a single pulse-echo transmission of a random interference wave.

Zhang et al. [147], used micro-UIT to inspect the same composite material with the same porosities as in Fig. 19 and Fig. 20. The technique can detect internal submillimetre micro-porosities (A, B and C) and provide the deepest detection depth (see Fig. 52), compared to micro-LLT and micro-LST (see §3.4), but the detection size is not accurate according to the authors.

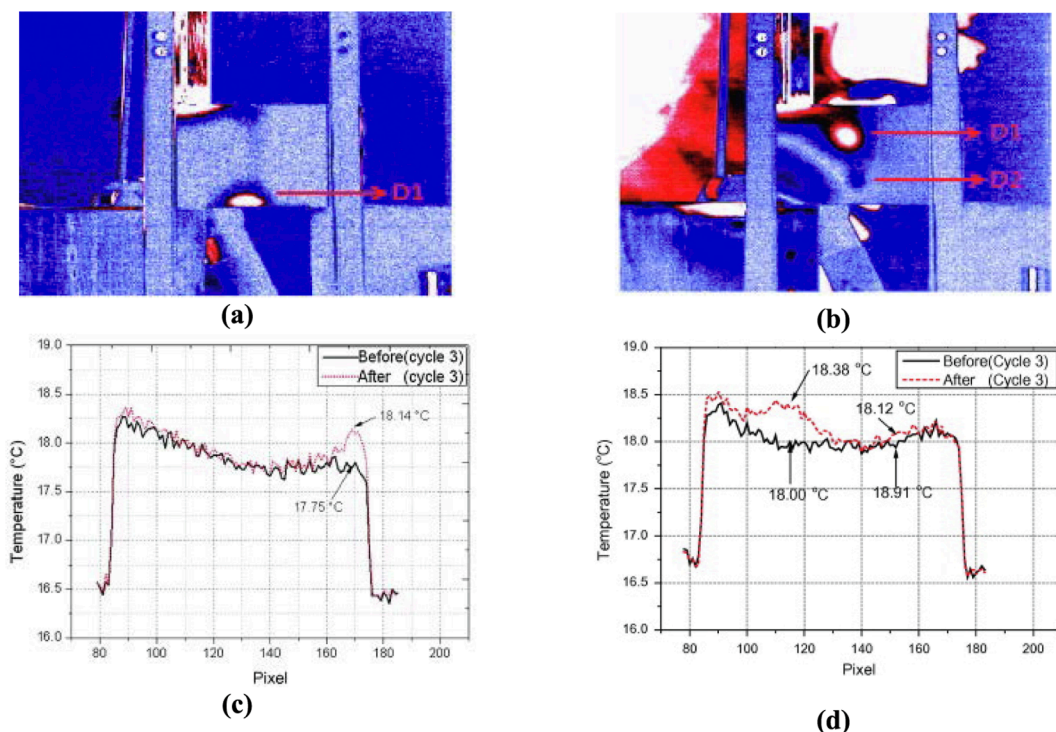


Fig. 49. Ultrasound lock-in phase infrared thermography images of dissimilar metal weld specimen: (a) 0° ; (b) 90° ; and temperature graph of dissimilar metal weld specimen by detection direction: (c) 0° , (d) 90° [258].

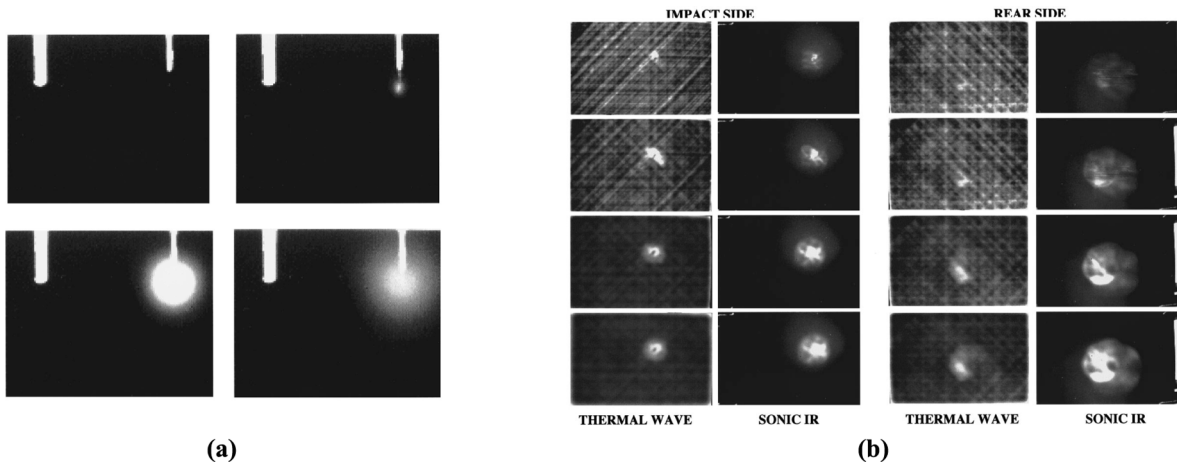


Fig. 50. Results of UIT for: (a) Aluminium samples - selection of four frames from a sequence of sonic IR images of a fatigue specimen containing two saw cuts, but with only one (right) having been used to initiate a fatigue crack; (b) Comparison of thermal wave images with sonic IR images of a thick (1.1 cm) CFRP slab containing interply delaminations from impact damage. The four rows of images were taken at progressively later times following flash (surface) or sonic (internal) heating. The left pair are images taken from the impact side, and the right pair from the rear side. [259].

Another common technique is ultrasound coded excitation, or harmony imaging, a signal processing technique where the high-pressure part of the ultrasound beam, by travelling faster than the low-pressure part, causes a nonlinear distortion in the shape of the wave which generates harmonics in the inspected component [261,262]. This technique has higher resolution than conventional UT because, as Uppal explains [261], since harmonics are multiples of the fundamental frequency, by transmitting a band of frequencies centred at 3 MHz, the resulting harmonic frequency bands will be centred at 6 MHz, 9 MHz, 12 MHz, and so on. This technique is commonly applied to inspect macro and micro defects [261,263–268]. Solodov et al. [269], presented case studies of the applicability of nonlinear ultrasonics (from where higher harmonic generation is included) for the detection of micro defects, like impact damage and delaminations in fibre-reinforced plastics, fatigue micro-cracking and cold work in metals, delaminations in laminates and fibre-reinforced concrete. Lines et al. [270], investigated and concluded that Golay-coded excitation can achieve and maintain SNR in the presence of high signal attenuation for UT using Full Matrix Capture (FMC) and TFM. Tang et al. [271], combined Lamb-wave-based Air-Coupled UT with coded excitation and pulse compression to locate blind-holes with diameters ranging from 3 to 7 mm in light-weighted plate structures. Deng et al. [272], proposed a 13-bit Barker code-based Magneto-Acousto-Electrical Tomography (MAET), that combines the high resolution of ultrasound imaging with the high contrast of electrical impedance tomography, to improve imaging quality and time. Sun et al. [273], proposed a 3D MAET based on a 1D ultrasound transducer and 13-bit Barker code excitation technology with the aim of providing more comprehensive understanding of the conductivity distribution of an object.

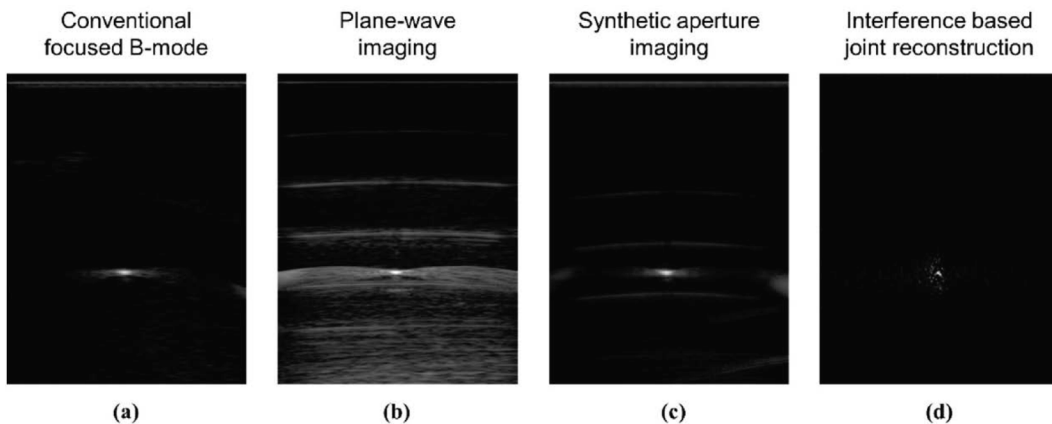


Fig. 51. Experimental results using a nylon wire submerged into a water tank: (a) an image reconstructed using the conventional focused B-mode; (b) an image reconstructed using plane-wave imaging; (c) an image reconstructed using synthetic aperture imaging; (d) an image reconstructed using the interference-based joint reconstruction method using data from a single pulse-echo transmission [260].

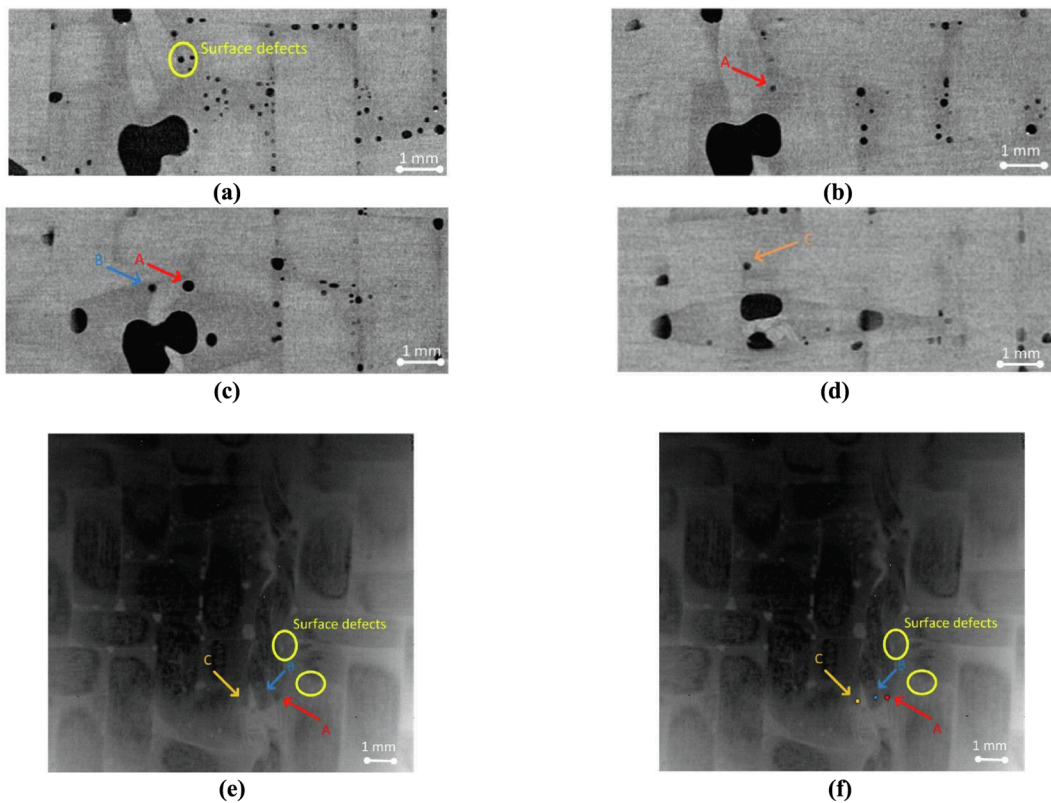


Fig. 52. The micro-CT results: (a) Surface; (b) Depth: 90 μm ; (c) Depth: 0.18 mm; (d) Depth: 0.414 mm. The micro-vibrothermography results: (e) Pulse: 10 s; (f) Pulse: 10 s (defects marked) [147].

5. Acoustic emission testing

Acoustic emission (AE) is a NDT technique based on the phenomenon that when external stimulus is applied to a material, e.g. temperature, loads and pressure, exceeding locally its mechanical resistance capacity, sudden local internal damage or micro-failure release high frequency stress waves or elastically stored energy. This energy propagates as mechanical waves within the material, which can be converted to electrical signals through the use of sensors, typically piezoelectric ones, e.g. made of ceramic elements like lead zirconate titanate (PZT). This phenomena and procedure allows the detection of small-scale damage in the material [274–277] at the moment of their formation, or evolution, although nor their positioning nor their dimensioning. Similar to UT, the mechanical waves can be longitudinal, shear, Rayleigh and Lamb waves [274]. Several mechanisms within a material can induce stress waves, like plastic deformation-induced dislocations and distortions, matrix cracking and fibre breakage in composites, phase transformations, precipitation fracture, cooldown cracking and thermal stresses [274,278,279].

There are two types of AE inspection, transient and continuous. The former assesses the condition of the material when the signal exceeds a defined threshold, i.e. when singular energetic events occur, like crack formation and growth in fatigue and crystalline distortion (twinning). The latter assesses the condition of the material within a time span, when there is plenty of low-level, background AE signal, which allows to detect leakages or plastic deformation, for example [274,280].

The signal parameters usually analysed in the AE signal waveform are peak amplitude, threshold to filter out background noise, duration, risetime, energy, counts (number of amplitude peaks greater than the threshold value), average frequency, ratio between risetime and amplitude (RA), and b-value and Ib-value (commonly used in seismology) [275,281].

AE is applied in fields like civil infrastructures [282–284], aerospace [285,286] and power plants [287–289], to monitor fatigue damage [290–294], corrosion and oxidation [278,295], creep [296–298], and machining tool wear [299], among others [300]. It can identify surface, subsurface and in volume defects, in materials like concrete [284,301], polymer matrix composites [302,303], ice [304–306] and steel [278,295]. The frequencies used for AE are usually between 20 kHz and 1 MHz, depending on the mechanisms that induce the stress waves [279].

AE can be conducted in-situ (laboratory and in-service inspection), to both small and large components; can be performed in short periods of time (few hours) or long periods of time (weeks); can detect a wide range of damage mechanisms, especially in their early stages, e.g. fatigue crack initiation [307]; can be applied in hazardous conditions like corrosive and nuclear conditions and in high temperatures. However, it can only detect defects that emit energy as they move or grow and it can only estimate qualitatively the damage, so the size and location of the defects are not quantified with this technique alone [307–309].

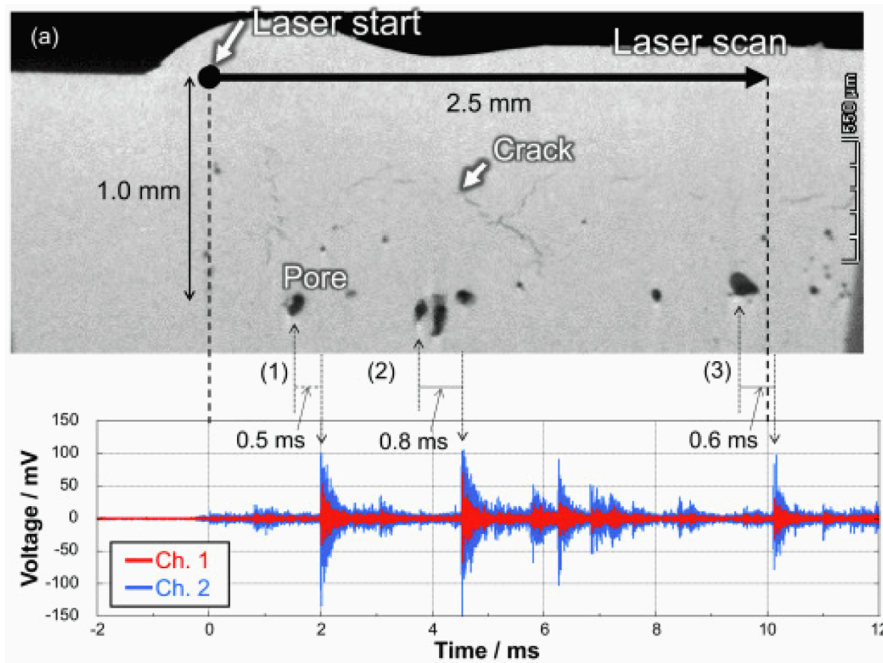


Fig. 53. Validation of AE measurements: (a) X-ray CT image after single-track test (4th specimen) and AE continuous waveform corresponding to the laser scanning speed. . Adapted from [310]

Kaita et al. [310], used a wireless AE process-monitoring equipment to inspect specimens made of Hastelloy X powder (Ni-alloy) and produced by SLM with different laser power, scanning speed (in the case of single-track test conditions) and hatch distances (in the case of multiple-track test conditions). Piezoelectric AE sensors were used with a resonant 250 kHz frequency. The authors were able to detect transient AE occurrences related to pores and microcracks in single-track tests, and to detect laser irradiation-induced cracks in multi-track tests. As shown in Fig. 53 (selected results for single-track test), the inspection using X-ray CT demonstrate the AE great capability to detect the formation of microcracking during additive manufacturing process (including an error position of few millimeters of AE events when compared to X-ray CT).

Calabrese et al. [311], studied martensitic stainless steel X12Cr13 submitted to five stress cracking corrosion tests, using three AE piezoelectric transducers with resonant 150 kHz frequency. Each test took between 300 and 400 h. The specimens used were dog-bone shape tensile test specimens, with a surface roughness of $0.3 \mu\text{m}$, and two transducers were placed at the two ends of the specimen, while the third was connected to an independent block to acquire the background noise. The results show five temporal regions related to different corrosion mechanisms, or corrosion damage stages, like initiation stage, activation stage (which may be linked to activation of local surface defects like pits, usually in the range of about $50 \mu\text{m}$), pre-quiescence stage, quiescence stage (which suggests cracking formation leading to the final failure) and re-activation stage. As shown Fig. 54, the use of b and I_b values trends allowed to differentiate the transition between corrosion stages. The plots are related to the different specimen regions, which have their own temporal division, denoted by the vertical lines, to indicate the b and I_b value trend during corrosion damage evolution. The increase of these values may render a good source to detect micro-crack formation and evolution.

Deschanel et al. [291], performed uniaxial strain-controlled tension-compression and stress-controlled cyclic fatigue tests on aluminium, 304L austenitic stainless steel, copper alloy and pure copper cylindrical specimens. Two AE piezoelectric transducers were placed at each head of specimens. The results indicate acoustic emission multiplets, i.e. repeated stress wave releases with highly correlated waveforms that are activated by consecutive loading cycles at close stress levels. This behaviour occurred in the different materials studied and may represent the incremental fatigue crack propagation (stage II). Examination by scanning electron microscopy (SEM) after interrupted test revealed signs of crack nucleation (after 600 cycles) that were not correlated with AE multiplets (multiplets were only detected after 1200 cycles). However, as shown in Fig. 55, there are some AE bursts in the first tens of cycles which correlates to dislocation motion corresponding to the cyclic-hardening stage, proving the high-sensitivity of AE to detect early-stage damage mechanisms.

As mentioned, AE is a widely applied technique and numerous reviews have been made on this concern, for instance, by Carrasco et al. [274], by Calabrese et al. [275], by Verstryngne et al. [312], and by Gholizadeh et al. [281].

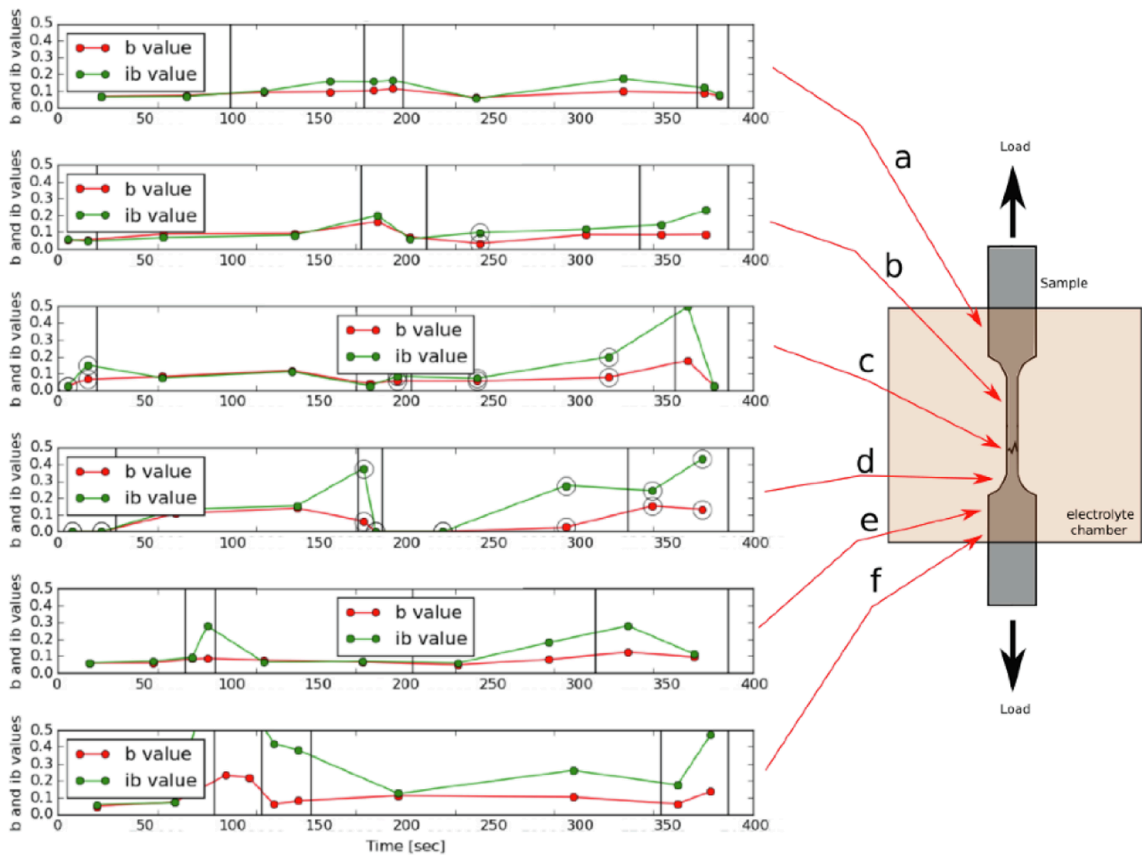


Fig. 54. B-value and ib-value trends for different regions of the dog bone shape specimen [311].

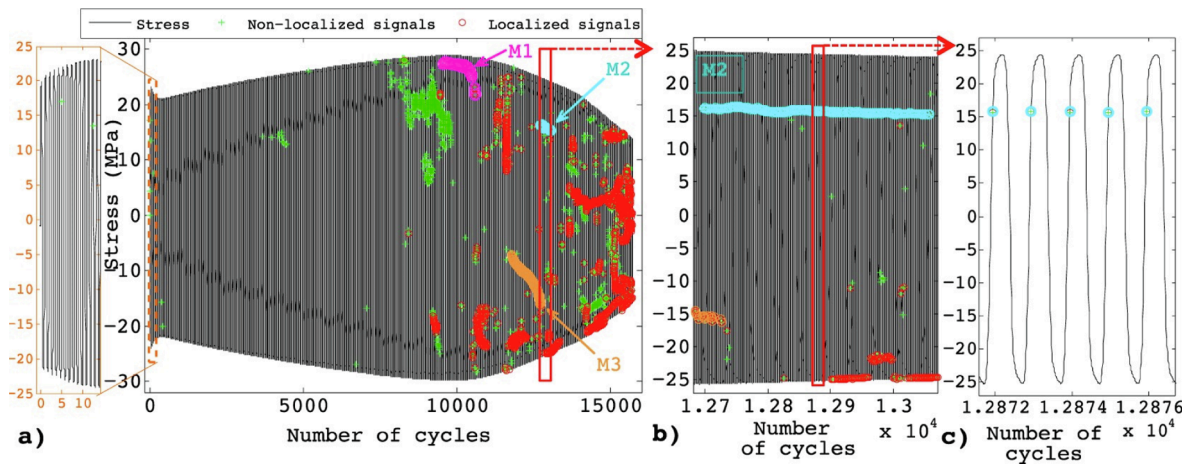


Fig. 55. Acoustic activity during a fatigue test at $\Delta\epsilon = 0.5\%$ on aluminium at 0.1 Hz: (a) Stress vs number of cycles with non-localized AE signals (green crosses) and localized signals (red circles). Magenta, cyan and orange clusters correspond to typical examples of multiplets: respectively named M1, M2 and M3; (b) Enlargement on M2 and (c) Enlargement on some loading cycles [291].

6. Electromagnetism testing

6.1. Eddy currents testing

Eddy Currents Testing (ECT) is part of the family of Electromagnetic Testing (ET) techniques. ECT is a non-contact NDT technique that indirectly inspects the surface and subsurface of an electrically conductive material, either ferromagnetic or non-ferromagnetic, based on the electromagnetic induction phenomenon [29,313].

In conventional ECT, an AC is applied in the excitation coil/filament, producing a primary magnetic field. When near a conductive material, this primary magnetic field generates an opposing secondary field and the inherent electric field, or eddy/Foucault current. This secondary magnetic field interacts with the primary one, affecting the electrical impedance in the excitation coil, in the case of absolute probes, or inducing an electric field in secondary sensitive coils, in the case of differential probes. For example, when there's a discontinuity, change in crystal orientation and/or chemical composition in the material, there's a local modification in the induced electrical field, which means that a different power is drawn from the excitation coil and therefore, the coil's electrical impedance is affected. This variation in the phase and magnitude of the electric impedance can be detected via monitoring the current and/or voltage [313]. Eddy current's intensity relies on the electrical conductivity and magnetic permeability of the material, influenced by the microstructure of the material, the distance between the excitation coil, the surface of the inspected object and the AC frequency of excitation of the coil. The intensity of the field of eddy current decays gradually with the penetration depth, which depends on the frequency of the probe, magnetic permeability and electrical conductivity of the material [29,314].

ECT is a highly sensitive technique to detect defects, and other properties, in the surface and subsurface of planar, tubular and other complex-shaped objects. ECT enables both manual and automated scanning, in a large temperature range, while it is tolerant to the presence of some level of dust, oils and dielectric materials. The ECT can be used in for different purposes, like measurement of material thickness, coating thickness, material electric conductivity, detection of superficial and sub-superficial discontinuities and heat damage (eg. grain coalescence in metals) [315]. ECT is commonly used in industries like aerospace [316], nuclear [317,318], automotive [319,320], and in monitoring the quality of advanced manufacturing applications, such as friction stir welding [321,322].

Overall, the ECT spatial resolution ranges from millimeter scale, with conventional probes, to micrometer scale, with advanced variants, e.g. by an optimal choice of probe type, geometric architecture and operation frequency. The size of the inspected area and depth of penetration are limited and depend on the coil's geometry, which is limited by the operating frequency [95,315]. As main limitations, the technique is very dependent on probe lift-off, sensitive to surface roughness and is influenced by the discontinuities' orientation, e.g. small cracks with the same direction as the flow of the eddy current result in negligible disturbance in the flow [315].

Hoffman et al. [323], developed an imaging technique, Eddy Current Microscopy (ECM), based on Magnetic Force Microscopy (MFM), to generate and detect eddy current, which is possible through mapping the variation of local electrical conductivity and magnetic properties. This technique can detect surface and subsurface discontinuities, with a spatial resolution of about 100 nm, and its sensitivity depends on the magnetic field strength of the tip and elastic constant of the spring cantilever [314]. Fig. 56 shows the contact-mode topographic results obtained for an Al₂O₃ matrix (70 %) with TiC precipitates (30 %).

Magnetic sensors detect changes in magnetic fields either created or modified by objects or other conditions, due to the magnetoresistance of the sensors' material, i.e. the ability to change the value of electrical resistance upon an induced external magnetic field. When small magnetic sensors are placed in arrays on a chip, they may detect small magnetic fields with high spatial resolution. Magneto Resistive (MR) sensors have good sensitivity and higher spatial resolution than inductive sensors [324]. Superconducting Quantum Interference Device (SQUID) sensors are magnetometers that measure magnetic fields based on the effect of Josephson junctions containing superconducting loops. Although with good sensitivity (they can detect artificial cracks with length of 50 mm and

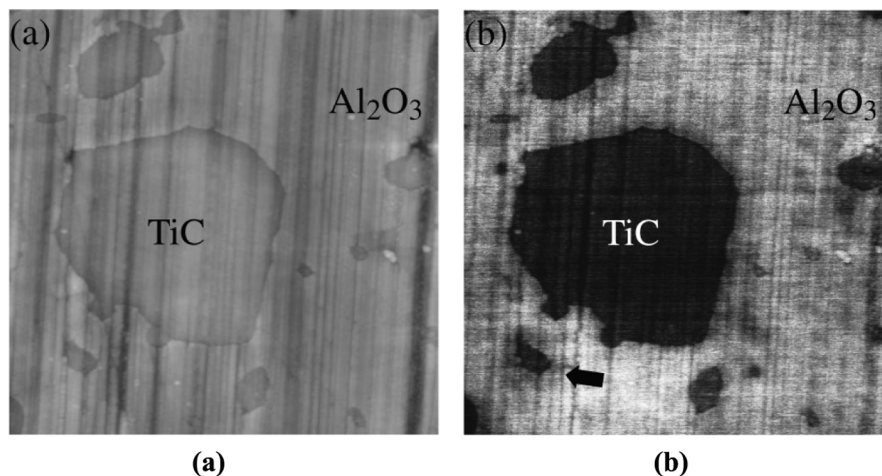


Fig. 56. Inspection of TiC precipitates in Al₂O₃ (5 × 5 μm²): (a) Topography; (b) Eddy current image. The arrow marks TiC underneath the surface [323].

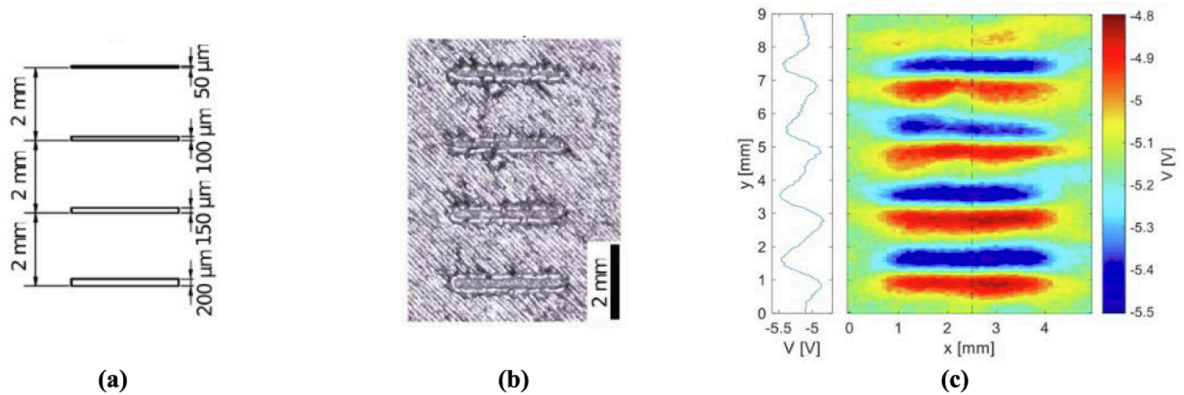


Fig. 57. GMR probes inspection: (a) CAD drawing of desired defect geometry (depth 200 μm); (b) Microscopic picture of artificial surface defects in 316L-SLM-200 specimen; (c) ECT data of artificial surface defects in 316L-SLM-200 specimen [323].

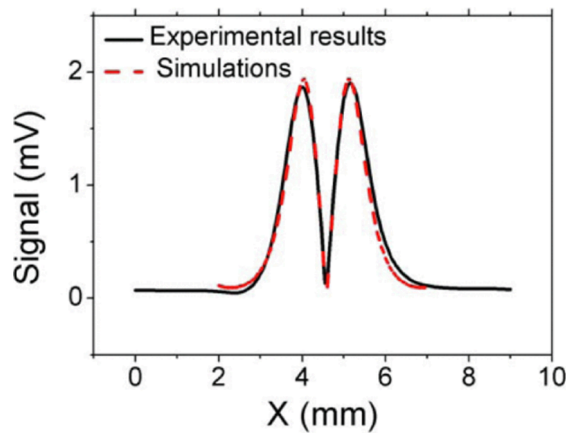


Fig. 58. Experimental sweep result (9 mm was achieved with 100 μm steps) when the probe was moved over the 400 μm width and 500 μm depth, and comparison with simulation preview [324].

width 0.3 mm [325]), the sensors are expensive and require a rather large inspection system and structure [326]. Giant Magneto Resistive (GMR) sensors are based on the GMR effect, where a multilayer pile of magnetic layers, separated by a thin non-magnetic film, induce a change in electrical resistance [327]. In one research, GMR probes were able to detect artificial defects in the order of 100 μm in 316L stainless steel produced by laser powder bed fusion [328]. Fig. 57 shows the CAD drawing and microscopic image of the defects as well as the GMR probe measurements, where all (four) artificial defects were distinguishably detected. The technique shows sensitivity for the variation in width of the defects and allows also to separate in space the defects, as the voltage values in free-defect zone are slightly higher than the ones in the defect area. In other related developments, such as the inspection of PCBs, GMR sensors provided inspections with micrometer spatial resolution [326,329,330].

Tunnel Magneto Resistive (TMR) sensors are based on the effect caused by tunnelling current through an insulating barrier, which is sensitive to temperature, voltage, thickness, and energy height of the barrier; and by scattering mechanisms. Cardoso et al. [324], optimized a Magnetic Tunnel Junction (MTJ) sensor that detected an artificial defect with a width of 400 μm and a depth of 500 μm in an aluminium block, as shown in Fig. 58. Pelkner et al. [331] developed an ECT probe (coils of 0.5 mm in diameter) using TMR arrays and Application-Specified Integrated Circuits (ASICs). The probe detected artificial defects with diameters between 440 and 445 μm , with varying spacing distances, in titanium and aluminium specimens, as shown in Fig. 59 (for the aluminium plate inspection). Zhang et al. [332], developed an Array ECT (AECT) probe with two rows of three-phase excitation coils and an integrated array of TMR sensors. The AECT probe was able to detect defects as small as $1 \times 0.2 \times 1 \text{ mm}^3$ (length \times width \times depth) corresponding to defect 5 in sample #1 of Fig. 60a, compared to a coil array probe (Fig. 60b and c).

Very small-sized critical defects, such as root defects in Friction Stir Welding (FSW) of aluminium alloys, have zero volume, and in the case of oxides and second-phase particles alignment, are not fully continuous. These type of physical material discontinuities have very low energy reflection for UT-based techniques and are even difficult to be detected by high-resolution techniques, such as CT [333,334]. For this purpose, a differential planar ECT probe was proposed, entitled as IONic probe. This probe is composed of a driver trace element in the middle (excitation filament) and two pickup planar coils wired on opposite directions (detector or sensitive coils) [335]. When an AC excites the driver trace, it induces 3D shape magnetic field, generating eddy currents on the material, which are

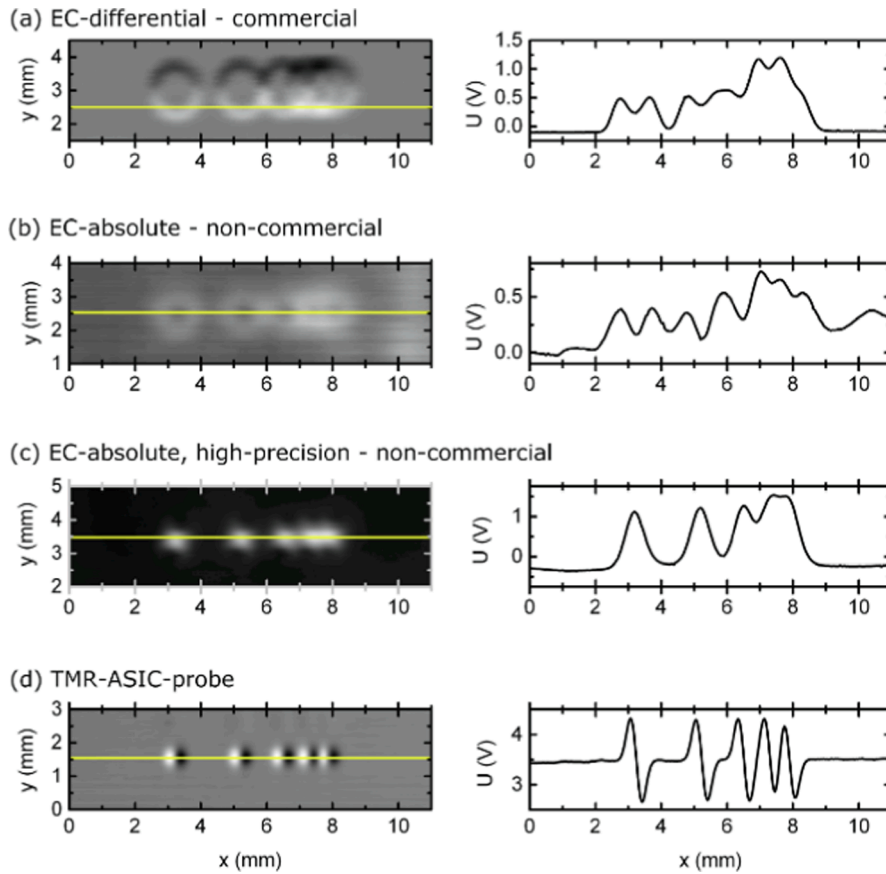


Fig. 59. ET-data of aluminium-sample Al-FN-22 for different probes (as grey-scaled plots on the left and as line cut across defect signals on the right): (a) Differential probe “KDS 2–2” of Rohmann GmbH; (b) Absolute probe BAM-made “A05”; (c) Absolute, high-precision probe BAM-made “AN05”; (d) TMR-ASIC-probe of the IMAGIC consortium for surface breaking defects [331].

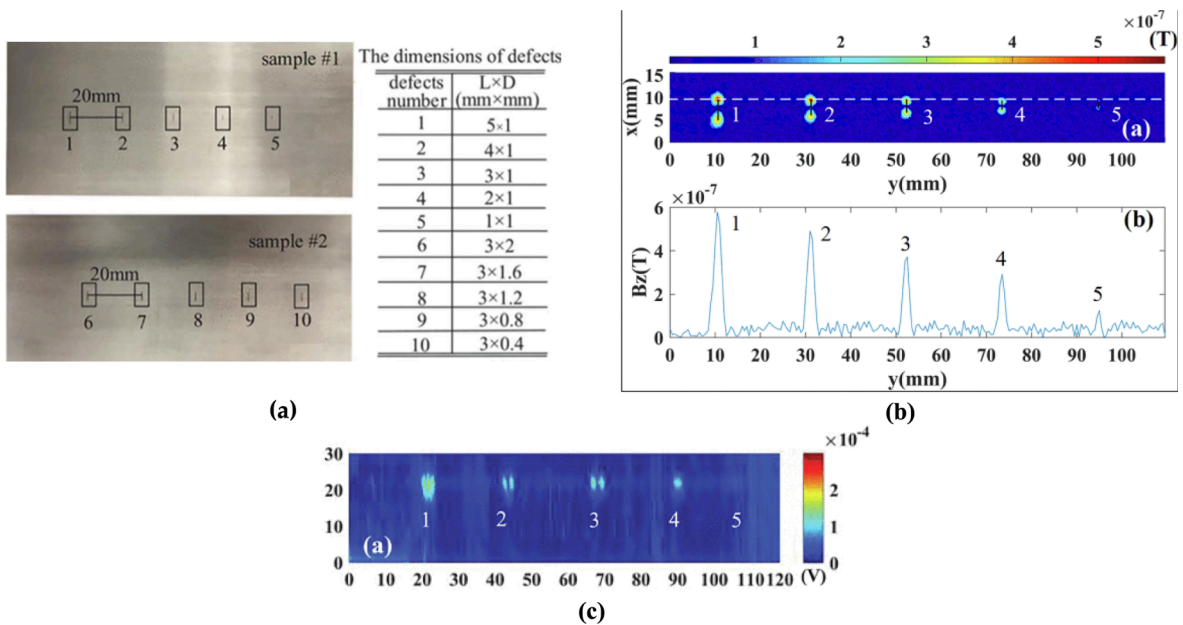


Fig. 60. Aluminum sample inspection: (a) Samples with machined defects; (b) AECT results for sample #1 with defects orientated in the vertical direction and the line scan of the defects along the white dash line; (c) Coil array probe results for sample #1 using 30 kHz.

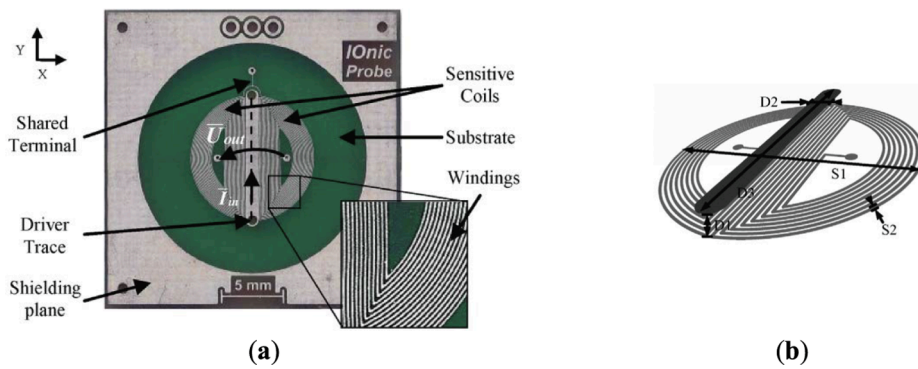


Fig. 61. Fundamentals and representation of an ECT planar differential ECT probe, identified as “Ionic Probe”: (a) Printed probe with nomenclature of main components; and (b) Representation of probe’s tested geometric parameters, namely D1-Driver vertical displacement to the sensitive coils plane (0, 0.15, 1.6 mm); D2-Driver trace width (0.5, 1, 1.5 mm); D3-Driver trace length ratio with parameter S1 (0.5, 1, 1.5 mm); S1- Sensitive coils external diameter (6, 10, 14 mm); S2-Sensitive coils windings width and clearance (0.05, 0.1 mm) [335].

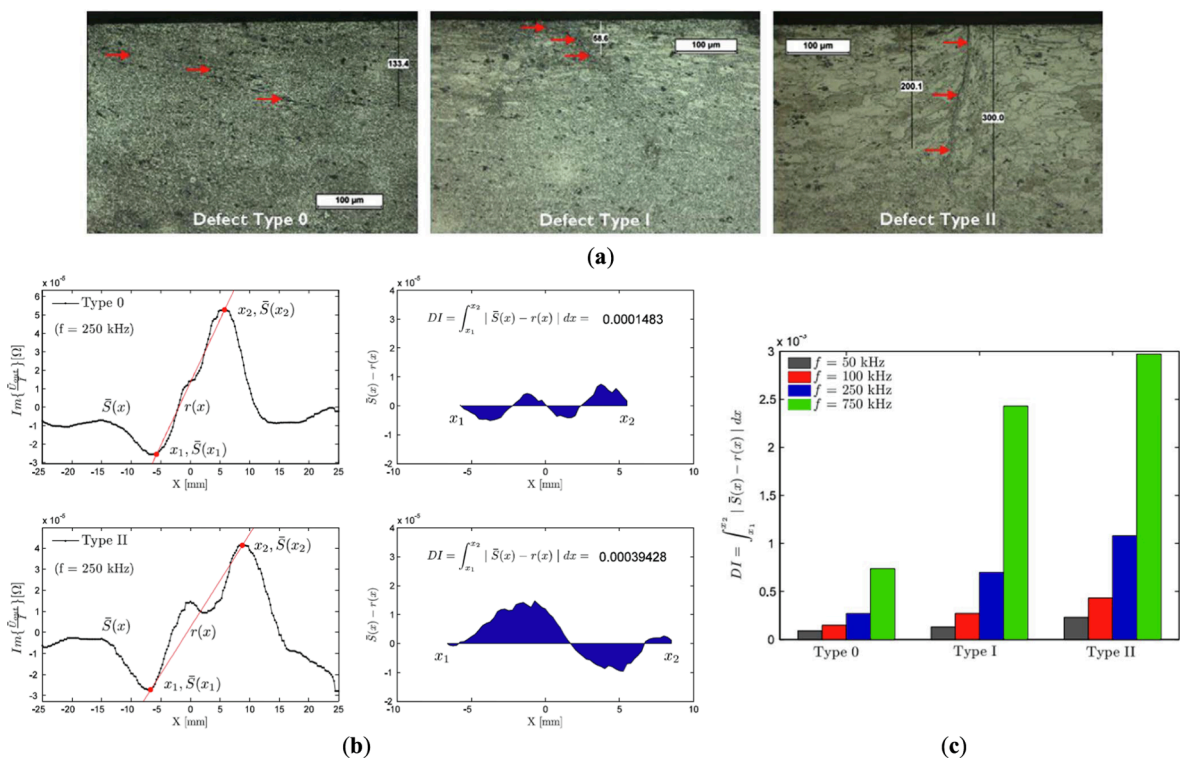


Fig. 62. Application of the ECT planar differential ECT probe, identified as “Ionic Probe” to inspection of different types of defects at the root of a friction stir welding (FSW) of an aluminium alloy AA2024 (plate thickness of 3.8 mm): (a) Transversal micrographs of three different FSW defective joints, namely defect type 0 (non-continuous oxide particles alignment), defect type I (about 58 μm), defect type II (about 200 μm); (b) formulation and graphical meaning of the defect index; and (c) establishment of the defect index for the three defects types and four different test frequencies [333].

also sensed by the pickup coils. A discontinuity or overall perturbation in the component can be detected by the modification of electric field balance between the two pickup coils [333]. The operation fundamentals of this IONic probe was modelled and geometric features were parameterized and optimized, as depicted in Fig. 61, by L. Rosado et al. [335]. This probe exhibits low leakage inductance and creation of heat, enabling it to be printed in flexible substrate material with enhanced sensitivity for NDT of small defects in complex shapes [321,336]. It can distinguish defects at depths below 60 μm on FSW joints of AA2024 alloy (Fig. 62); up to 500 μm on stainless steel AISI 304 alloy; between 100 and 3000 μm in graphite and up to 2.5 mm on GLARE® composite material [322,333,337,338]. One study was conducted in AA2024-T351 plates with 3.8 mm thickness and three different laboratory-induced root defects: defect type 0 consisting of residual particles alignment along a path of approximately 150 μm; defect type I with 60 μm of size, approximately; and

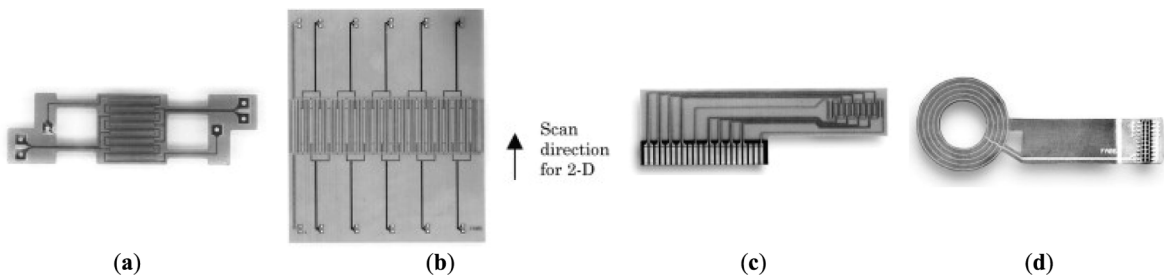


Fig. 63. Typical MWM sensor and MWM-Arrays: (a) MWM sensor; (b) Scanning five-element MWM-Array; (c) Eight-element MWM-Array for detection on fatigue initiation; (d) Four-element MWM-Rosette for detection and monitoring of fatigue cracks at fasteners (note that (c) and (d) are examples of MWM-Arrays designed for permanent mounting) [340].

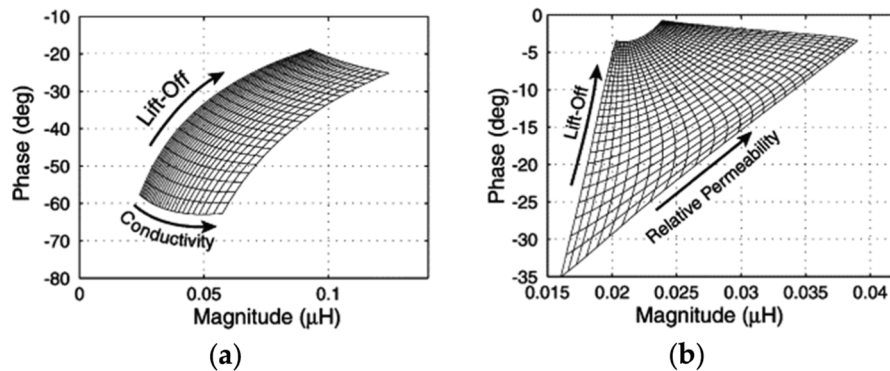


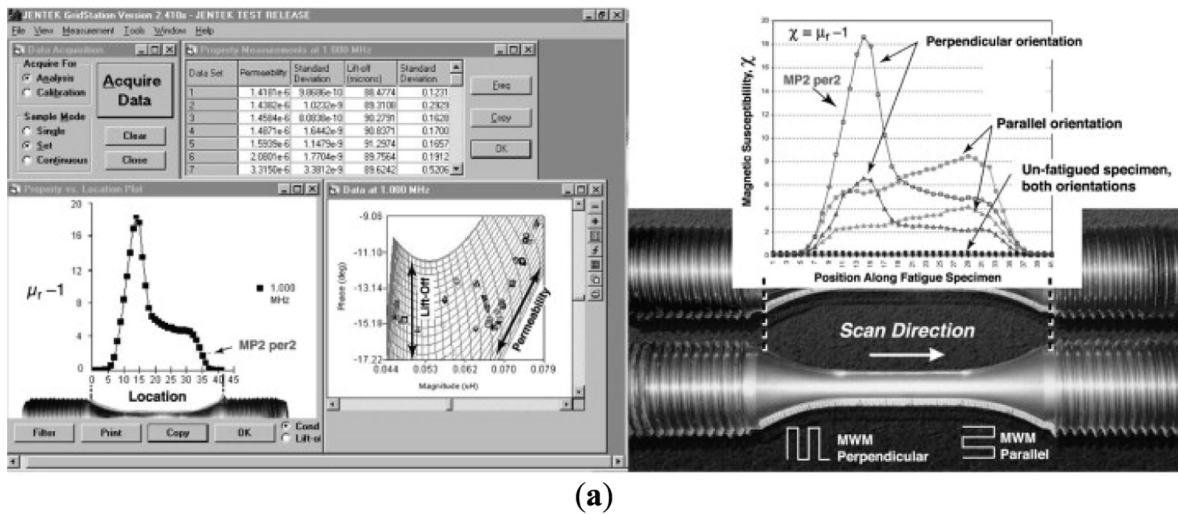
Fig. 64. Examples of representative measurement grids for (a) aluminium and (b) low alloy steel [340].

defect type II with 200 μm of size approximately. As shown in Fig. 62, the IOnic probe identified different levels of FSW root defects, and an evident relation between the defects size and the signal perturbation can be observed [336].

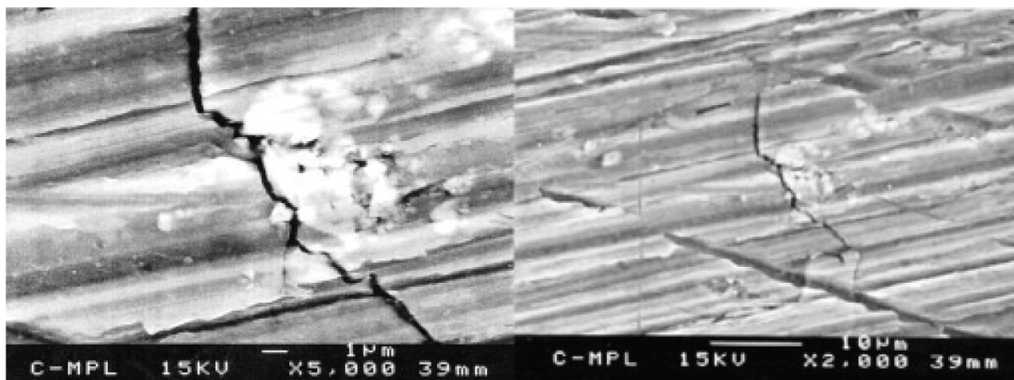
Another advanced ECT technology is Meandering Winding Magnetometer-Array (MWM-Arrays) probes, where the primary and secondary windings in the sensor have a square wave pattern, as shown in Fig. 63. This allows the creation of spatially periodic magnetic field when a current is applied in the primary winding, and to measure the response of the signal (voltage) in the secondary winding [339]. By using arrays of secondary windings, individual or combined signal responses can be used for one primary winding. The sensors are produced via micro-fabrication, resulting in highly reliable and highly repeatable identical sensors at low unit costs [339,340]. MWM-Arrays can be supported by grid measurements, which are two-dimensional databases of the sensor responses that relate two measured parameters (e.g. lift-off and conductivity/permeability, as shown in Fig. 64), that don't depend upon calibration and instrument set-up, as opposed to conventional ECT. By using grid measurements, it becomes easier and more efficient to convert the response in the secondary winding into geometric and material properties, like layer thickness, electrical conductivity and magnetic permeability measurements, which contribute to characterize stress, porosity, crack length, cold work, and microstructural changes in the material due to manufacture and in-service damage mechanisms, e.g. fatigue [339–341].

As presented by Zilberstein et al. [340], MWM-Arrays can detect early fatigue damage and short cracks (less than 50 μm long and less than 25 μm deep) in austenitic stainless steels components and aluminium alloy components under tension–tension cyclic loading, respectively. They have also shown that this technique is capable of on-line monitoring and detection of crack initiation and growth during fatigue tests of coupons, components and/or areas of difficult access (e.g. fuel tanks on aircraft) [340,341]. Another study proved the capability of MWM-Arrays to detect lack of penetration defects, as small as 0.75 mm, in aluminium alloys joined by FSW [342,343]. Fig. 65 shows two examples of MWM-arrays fatigue damage assessment.

Ma et al. [344], proposed a novel flexible eddy current sensing system that incorporates double square winding excitation with a multi detection flexible array for cracks inspection (mm range down to 0.5 mm width). Yang et al. [345], developed an electromagnetic in-pipe detector based on passive resonance-enhanced differential planar coils, that detected corrosion pits and cracks with defect size in the millimeter range. Daura et al. [346], proposed a ECT inspection technique with integration of a transmitter–receiver (Tx–Rx) Flexible Printed Coil (FPC) array with dual resonance response Wireless Power Transfer (WPT), to inspect a pipeline sample with a dented area due to metal loss and corrosion. Long et al. [347], proposed a resolution enhanced ECT array probe to detect machined defects, in the μm –mm range, in a 304 stainless-steel sample. Sondhi et al. [348], developed a multilayer flexible screen-printed coil that can be used to generate low-frequency magnetic fields for applications such as WPT. Marchand et al. [349], developed two innovative flexible ECT probes composed of 64 and 96 micro-coils etched on a flexible film, which were able to detect defects as small as 100 μm on an Inconel and aluminum plate. Zhang et al. [350], proposed a flexible ECT probe with front-end differential setting to detect defects in the mm range in CFRP components. Camerini et al. [351], proposed an EC system using coils with orthogonal



(a)



(b)

Fig. 65. MWM-arrays fatigue damage assessment: (a) Detection of fatigue damage in Type 304 stainless steel by MWM bi-directional permeability measurements [340,341]; and (b) Detection of a 40- μ m-long crack detected by MWM with grid methods. This test was stopped when a significant reduction in MWM monitored conductivity occurred [340].

configuration connected in differential model that successfully detected fatigue cracks (mm range) in clad pipelines.

Eddy Current Pulsed Thermography (ECPT), also known as induction thermography, is a NDT technique that combines ECT and thermography, where eddy currents generate heat, by resistive losses that release heat, directly to the surface of the component. This generated heat can be detected by an infrared camera [40,352]. ECPT is usually applied to inspect metals and composites [353–359]. Genest et al. [360], applied ECPT to a Thermo-Mechanical Fatigue (TMF) test uncoated specimen to detect cracks, as small as 0.25 mm, and to a high temperature tensile test (HTTT) uncoated specimen to obtain the Strain to Crack (SC) information (strain at which the first crack occurs), as shown in Fig. 66. They also employed an algorithm to enhance the crack contrast and obtain accurate crack measurements.

Liang et al. [361], inspected a CFRP sample with damage produced by 4 J low energy impact, using ECPT alongside PCA combined with wavelet transform. Fig. 67 presents the results, where visual damage was not found using stereomicroscopy, but can be detected using ECPT (Fig. 67b) and further enhanced with thermal image processing (Fig. 67c).

Li et al. [362], proposed a multiphysics structured ET and ECT in moving mode, with a novel L-shape ferrite magnetic yoke surrounded with array coils, that was able to inspect artificial cracks with a length of about 50–60 mm. Liu et al. [363], proposed a method of using the skewness of ECPT, under stationary and scanning conditions, to quantify the depth of rolling contact fatigue cracks, ranging between 0.35 and 8 mm. Yi et al. [364], proposed a Eddy Current Pulse-Compression Thermography (ECPuCT) that combines Barker code modulated eddy current excitation and pulse-compression technique, to characterize delamination on CFRP materials with defects in the mm range. Wang et al. [365], developed a new ECPT signal feature, Dynamic Apparent Time Constant (D-ATC), that associates the dynamic behaviour of the induced eddy current with the geometric dimensions of the test pieces by the time and amplitude signatures of the D-ATC curve, to detect the sub-millimeter thickness of non-ferromagnetic conductive plates under large lift-off conditions. Xie et al. [366], combined ECPT and a stacked autoencoder (SAE) model, called a Stacked Autoencoder - Eddy Current Pulsed Thermography (SAE-ECPT), to visualize internal artificial debondings, delaminations and cracks, in the mm range, in

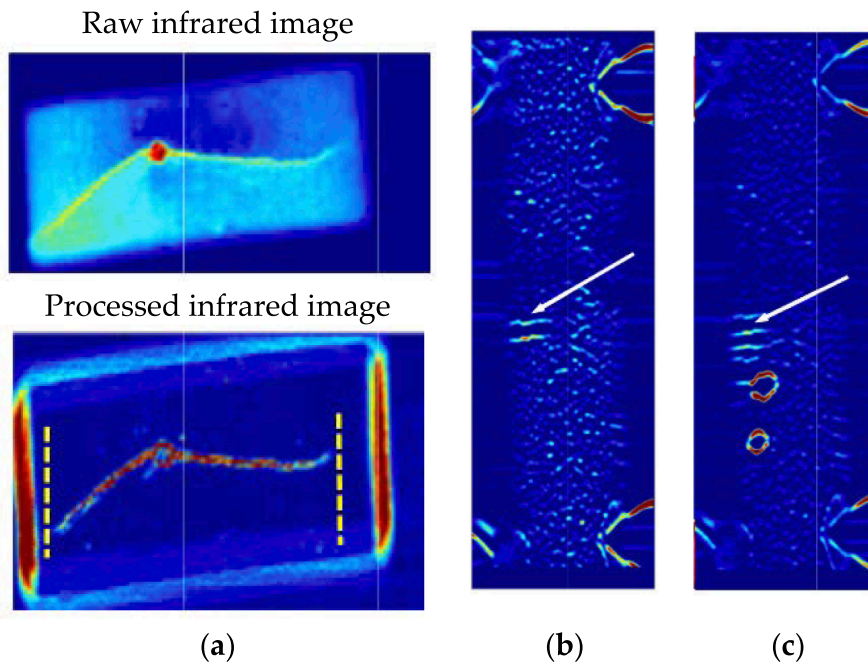


Fig. 66. ECPT measurements: (a) Raw and processed infrared images at cycle 240 of TMF; (b) Processed in-situ infrared image of first crack in HTTT; (c) Post-test processed infrared image in HTTT [360].

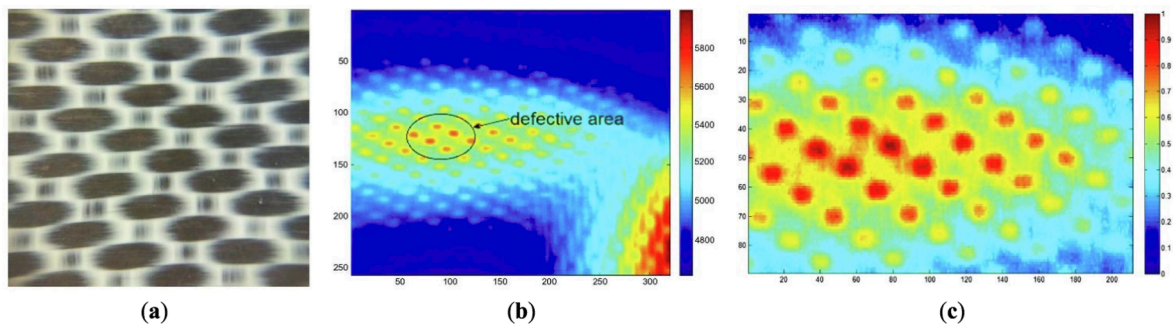


Fig. 67. Inspection of low energy impact damage in CFRP: (a) Stereomicroscopy surface image; (b) 75th frame thermal image; (c) 75th frame thermal image after wavelet transformation combined with PCA [361].

CFRP-reinforced steel structures. Tong et al. [367], proposed using ECPT with hybrid post-processing strategy combining PCA and 2D wavelet transformation to characterize the depth profile of artificial fatigue cracks. Tu et al. [368], applied ECPT to successfully detect conductive defects in composite insulators, alongside algorithms like fast Fourier transform (FFT), PCA, independent component analysis (ICA), and partial least-squares regression (PLSR), to enhance the features of defects and/or separate different transient thermal patterns. Hernandez et al. [369], applied ECPT to inspect in-service corrosion in a painted aluminum aircraft panel. Defects as small as 0.4 mm were detected using phase, amplitude, and temperature contrasts, the former one being more suitable for defects smaller than 2 mm. Additionally, Sophian et al. [370], wrote a literature review paper about ECPT.

6.2. Alternating current field measurements

Alternating current field measurements (ACFM) is an electromagnetic technique used for the detection and sizing of surface opening defects, based on the alternating current potential drop (ACPD) technique [371–373]. The ACFM inducer probe introduces an AC locally into the component that generates electromagnetic fields close to the surface. The ACFM detecting probe measures the associated electromagnetic fields. If a crack is present, the electromagnetic field around the crack is disturbed. Components of the magnetic field in the x direction (B_x) will produce a dip along the crack that allows the measurement of the depth of the defect, while components in the z direction (B_z) will produce a strong peak and a trough near the end of the crack allowing the measurement of the length of the defect [371–373]. ACFM is applied in fields like railways [371,374,375], underwater structures [376,377], and oil

Table 5
The sensitivity of RACFM and ACFM experiments [372].

Crack angle /degree	ACFM results		RACFM results	
	Sx / (%)	Sz / (%)	Sx / (%)	Sz / (%)
0	31.7	72.2	32.6	69.5
10	29.3	70.2	32.2	68.6
20	21.6	52.4	31.6	69.1
30	8.2	17.4	30.7	66.5
40	2.9	6.6	28.1	61.5
50	–	–	27.3	59.7
60	–	–	27.6	62.3
70	–	–	28.0	65.2
80	–	–	27.8	69.5
90	–	–	28.1	73.8

industry [375].

Li et al. [372], proposed a rotating alternating current field measurement (RACFM) method for the detection of arbitrary-angle cracks with high sensitivity (mm range). Table 5 shows the sensitive parameters (Sx and Sz) from the experimental results of RACFM and traditional ACFM, for a Q235 mild steel sample with a 45 mm length and 7 mm depth artificial EDM notch, with the angles between the scanning path and crack varying from 0° to 90°. The results suggest that compared to conventional ACFM, the new technique can inspect defects at different directions, with the minimum sensitivities of Sx and Sz being 27.3% and 59.7%, respectively, for crack angle of 50°, and that RACFM can achieve high detection sensitivity for underwater cracks.

6.3. Magnetic particles testing

Magnetic Particles Testing (MT) is a NDT technique that inspects surface and subsurface discontinuities in components made of ferromagnetic material. The MT is based on the phenomenon that when an object with high magnetic permeability is subjected to a magnetic field, a magnetic flux leakage may occur in the presence of defects in the component. The detectability and resolution of MT depends on the intensity of the eventual magnetic flux leakage, and on the mobility (depends on the particle shape and mass) of strongly ferromagnetic particles which are attracted to the regions with magnetic flux leakage. The technique's procedure consists of cleaning the surface of the inspected object, magnetizing the component following by the application of magnetic particles, and then proceeding with the inspection of defects. After the inspection, the component is demagnetized and any residue of magnetic particles is cleaned [378]. The component can be magnetized either by permanent magnets, electromagnets, or electric AC or DC-induced methods. The magnetic particles can be applied either through a wet suspension or as a dry powder, and their size can range between 10 and 30 μm . When using MT, the magnetic flux should be correctly misaligned with the defects so that they can be detected. Magnetic particle inspection does not give information on the defect depth and components with complex geometries may present areas with little or no magnetic flux [379].

As state of the art on the detection of small-scale defects, Vasylenko et al. [380] developed a technique for detecting micro defects based on luminescent ferrofluids derived from CoFe₂O₄ nanoparticles, ranging in sizes between 5 and 11 nm. Luminescent ferrofluids were able to detect an artificial ring defect of 10 mm diameter with an opening width of 1.2 μm , invisible to the naked eye, in a steel

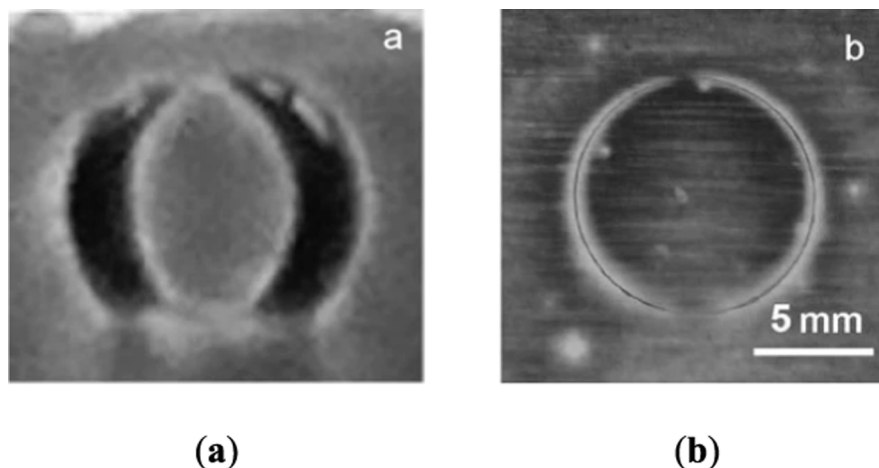


Fig. 68. Visualization of the artificial ring defect using: (a) Ferrofluids; (b) Luminescent ferrofluids. .
Adapted from [380]

plate. Fig. 68 shows the authors' results when using ferrofluids, see Fig. 68a, and luminescent ferrofluids, see Fig. 68b. Using luminescent ferrofluids with a concentration of 3.1 g/L presents a better contrast than simply ferrofluids, which can be perceived even with quality differences in the images, maybe due to the use of different dyes and the effect of the dye concentration on the image contrast, as mentioned by the authors.

6.4. Magnetic flux leakage

Magnetic flux leakage (MFL) is an electromagnetic NDT technique that also inspects surface and subsurface discontinuities in components made of ferromagnetic material. MFL is based in the same phenomena as MT, however it is composed of a probe with a magnetic detector, like Hall sensors, placed between the poles of the permanent magnet and yoke, where it can detect the leakage field [381].

Li et al. [382], proposed a Micro Magnetic Bridge Probe (MMBP) to be used in MFL in order to detect micro-cracks. As shown in Fig. 69a, a magnetizing coil is used to generate an AC magnetic field and the U-shaped magnetic yoke is used to generate a magnetic bridge. In the testing magnetic circuit, a magnetic sensor measures magnetic flux changes. The sample tested is a Q235A plain carbon structural steel and the defects have length of 6 mm, width between 60 and 80 μm and depth between 7 and 60 μm. All the defects were detected, including the one with smallest depth of 7 μm (S6 in Fig. 69b).

Pham et al. [383] developed a planar Hall magnetoresistive (PH-MR) sensor, in an exchange-biased multilayer structure, for MFL detection. The authors claim that PH-MR has the advantages of high SNR, of small thermal drift due to the orthogonal arrangement of its output voltage and supplying voltage bars, and of being able to answer to a wide range of a bipolar magnetic field. Fig. 70 shows the

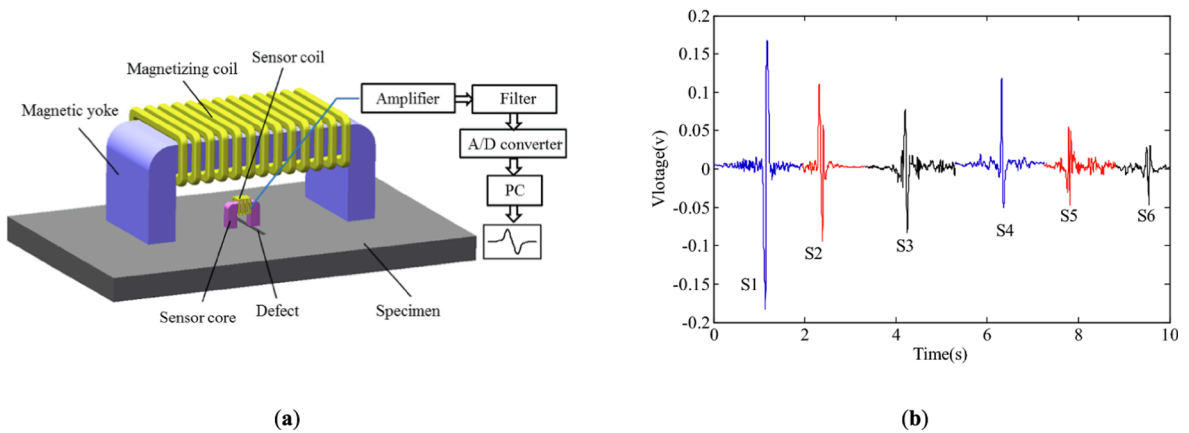


Fig. 69. Micro-magnetic bridge probe in MFL defect detection: (a) MMBP in MFL schematic representation; (b) MFL testing signals using MMBP [382].

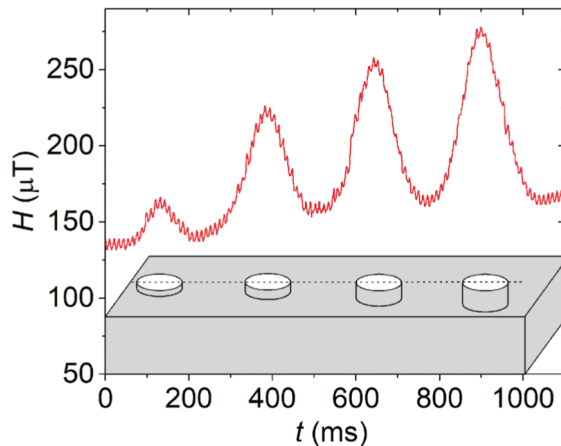


Fig. 70. MFL signal measured in real time using a PH-MR sensor prototype on a sample having four cylindrical-hole defects with an identical radius of 2 mm and different depths of 0.5, 1, 1.5, and 2 mm [383].

inspection results done for a carbon steel with artificial cylindrical-hole defects with radius of 2 mm and different depths of 0.5, 1, 1.5, and 2 mm.

Additionally, Gao et al. [384], compared MFL and ECPT for the inspection of multiple cracks (mm range), and proposed a new technique, ferrite-yoke-based pulsed induction thermography, that combines the ferrite-yoke structure of MFL and the high current and high frequency pulsed excitation of ECPT. This technique may prove suitable in the future to detect micro surface and subsurface defects in ferromagnetic materials. Ru et al. [385], proposed a new coupling sensor that merges ACFM and MFL, consisting of a rectangular-shaped ferrite magnetic excitation structure of coupling electromagnetic sensing that induces an uniform Eddy current field and a primary magnetic flux field, and that is able to detect surface and subsurface defects in the mm range. Hosseingholizadeh et al. [386], proposed a MFL system to increase the accuracy of defect characterization in the mm range that can distinguish different defect shapes located on the far side of a steel plate and that uses a sensor lift-off compensation scheme based on AC signal phase.

6.5. Other electromagnetic techniques

Magnetic Barkhausen Noise (MBN) is a magnetic measurement technique that evaluates the surface and subsurface of a sample of ferromagnetic material and can detect the microstructure (lattice strains and imperfections), stress field, chemical inhomogeneities, grain size, and surface or near-surface residual stresses [387,388]. The Barkhausen effect consists of sudden movements and changes in the size and orientation of magnetic domains, i.e. small order magnetic regions that exist in ferromagnetic materials, that occurs when these materials are continuously magnetized or demagnetized by an alternating magnetic field. This changes in magnetization can be detected because the transitions of the magnetic field of the material induce an electrical pulse in an inductive coil placed near the specimen, affecting its magnetic field, and a signal resembling noise, the Barkhausen noise, is generated. Material characteristics such as the distribution of elastic stresses and microstructure affect the movement of domain walls which affects the electrical pulses produced by these movements and therefore, affect the MBN signal output [389].

Although there are no standard designs for the equipment, it typically consists of a probe or sensor with a magnetization coil connected to a measurement device and a computer [390]. There exist many different probes that are suitable for different applications, for instance, in welding [391], aeronautic [387], and transportation [392,393]. The resolution of the technique is related to the coil's sensitivity, which in turn depends on the coil's geometry. Other challenges of the technique include its complexity, the domain walls are very narrow, and the timescales involved in these phenomena are extremely short.

Even though a technique not yet employed for very small defects, it has been shown that localized peaks in the MBN results when scanning the surface of a martensitic stainless-steel plate subjected to controlled fatigue load revealed the presence of surface flaws with a dimension of 10 mm, as well as the stress pattern in the beginning and ahead of the crack tip. Furthermore, an assessment of the smallest size crack that can be detected through the variation of the different parameters is suggested for future works [389]. Liu et al. [394], investigated the correlation between Domain Wall (DW) motion and MBN under different tensile tests to successfully quantitatively analyse micro-macro magnetic properties and variations.

Metal Magnetic Memory Testing (MMM) is an emerging weak-field detection technique which uses the geomagnetic field, such as Earth's magnetic field, rather than an artificial magnetic field, to measure the self-magnetized leakage field and detect damage in ferromagnetic components [395,396]. MMM is used mainly for detecting early damage, e.g. micro-crack and fatigue damage, due to the magnetic flux leakage signal of stress concentrations owing to the geomagnetic field excitation [397–404]. Shi et al. [405], have written a review concerning the current status and challenges of the technique.

The 3MA technique (Micromagnetic Multiparameter Microstructure and Stress Analysis) is a micromagnetic multiparameter NDT technique that combines different micromagnetic and electromagnetic measuring quantities, like the magnetic Barkhausen noise, harmonic analysis of the tangential magnetic field strength, multifrequency eddy current analysis and incremental permeability analysis. It uses regression analyses or pattern recognition algorithms for the quantitative determination of material properties for ferromagnetic materials [406,407]. The use of multiparameter avoids any disturbance that may affect stress measurement, like surface treatment and microstructure, and allows predicting several features at once, like residual stresses, hardness, and hardening depths. 3MA has been shown to help understand early material degradation [408].

7. Motion of matter at the inspected surface

7.1. Dye penetrant testing

Dye Penetrant Testing (PT) is a NDT technique that inspects the surface of an object. It can be applied to many different materials, such as ferrous and non-ferrous metals, including powdered-metal objects, glass, ceramics and some types of plastics, but not on materials with a rough or porous surface. It is commonly applied to inspect surface cracks, at both face and root domains of weld joints.

The procedure consists of cleaning the targeted surface zones of the inspected object, applying a dye penetrant to the surface and allowing some dwell time for it to penetrate the surface discontinuities, removing the penetrant's excess and applying a developer. There are different penetrants for different desirable sensitivities, depending on their capillarity and viscosity, and are also classified based on dye fluoresces, e.g. under black light or white light, and based on the type of dye removal, e.g. water or other solvents. The

developer applied can be a dry power developer, or a powdered material suspended in water or a volatile solvent, known as a wet developer [28,409].

According to Carvalho et al. [410], PT allows the identification of some defects with approximately $0.9\ \mu\text{m}$, but only when the defect depth is larger than its superficial open area, since its physical principle is exclusively based on the high capillarity and low viscosity of the penetrant.

The chemical products may be harmful to the operators and the handling and disposal of the oil-based products impacts negatively the environment [411,412]. However, more ecological alternatives have been proposed, for instance, the use of bacterial suspension as penetrant, like *Rhodococcus erythropolis* DCL14 strain [413] and *Escherichia coli* bacteria [414], semiconductor quantum dots (Qdots) [412] and radiolabelled Qdots [415]. The application of these, and other, advanced technological dye penetrant solutions, are further addressed in §7.2 and §7.3.

7.2. Driven bacterial cells testing

A NDT technique based on bacterial cell suspensions was proposed by Santos et al. [413,416–420]. This technique consists of applying a non-pathogenic bacterial suspension-based penetrant to materials to identify micro-surface defects. Bacterial cells have properties that are a great asset for NDT purposes, such as small dimensions (some smaller than $1\ \mu\text{m}$), high penetration capacity due to biosurfactants production, motility, adherence, fluorescence (either natural or by addition of chemical compounds), reproducibility and death, endothermic and exothermic properties and response to electric and magnetic fields [413,416]. Even though the application and steps may be similar to dye penetrant, some of the bacterial properties, which are not present in the former, allow an improved sensitivity to detect surface defects. Additionally, according to the study, the bacterial cells penetrated and adhered preferentially to defects, controlled by the capillarity, wettability and viscosity of the suspension, even after removing the excess bacteria and without the application of magnetic or electric fields [417]. In order to avoid the creation of biofilms, which may be harmful to the materials [416], the penetration time needs to be well reduced and controlled and the sample needs to be properly cleaned after the inspection. Under these controlled steps, the technique is innocuous and environmentally friendly, since no harmful liquids need to be disposed or recycle nor are aerosols formed.

Santos et al. [413] used *Rhodococcus erythropolis* DCL14 strain, with dimensions between 0.9 and $1.5\ \mu\text{m}$, to study stainless steel AISI 304L, aluminium alloy AA1100 and electrolytic copper. Under the conditions of the tests, the detection limit for the artificial micro-indentations was $2.9\ \mu\text{m}$ depth in steel, $4.3\ \mu\text{m}$ depth in aluminium and $6.8\ \mu\text{m}$ depth in copper with a penetration time of 4 min, 4 min and 3 min, respectively. In a following study [417], it was applied a magnetic field and used the same *Rhodococcus erythropolis* DCL14 strain to study micro indentations in a stainless steel AISI 316L and aluminium alloy AA1100. These new conditions resulted in a new enhanced detection limit of $1.8\ \mu\text{m}$ depth and $8.8\ \mu\text{m}$ side length for aluminium and $1.4\ \mu\text{m}$ depth and $6.8\ \mu\text{m}$ side length for AISI 316L stainless steel. Additionally, through the application of nanoindentations on the steel, with loads between 125 and 50 mN, this technique was able to detect defects with $0.6\ \mu\text{m}$ depth and $5.3\ \mu\text{m}$ side length. Fig. 71a shows the matrix of nanoindentations under SEM and Fig. 71b shows the matrix under fluorescence optical microscopy, after applying the bacterial cells and without the application of magnetic or electric fields. The suspension was also used to successfully detect $0.5\ \mu\text{m}$ wide and $10\ \mu\text{m}$ depth artificial cracks in a reference test block Type 1 ISO 3452–3, as shown in Fig. 72. The authors also concluded that it is possible to distinguish zones with different roughness. These articles show the potential of this technique for detecting sub-micron and nano surface defects.

In another study [414], it was shown that Fluorescein Isothiocyanate (FITC) conjugated *Escherichia Coli* (*E. coli*) bacteria used as fluorescent penetrant can be used for the inspection of small defects in different test materials, with the width and depth ranging between 200 and $400\ \mu\text{m}$. Fig. 73 shows the inspection results on a PSM-5 panel using FITC-*E. coli* and commercial dye penetrant.

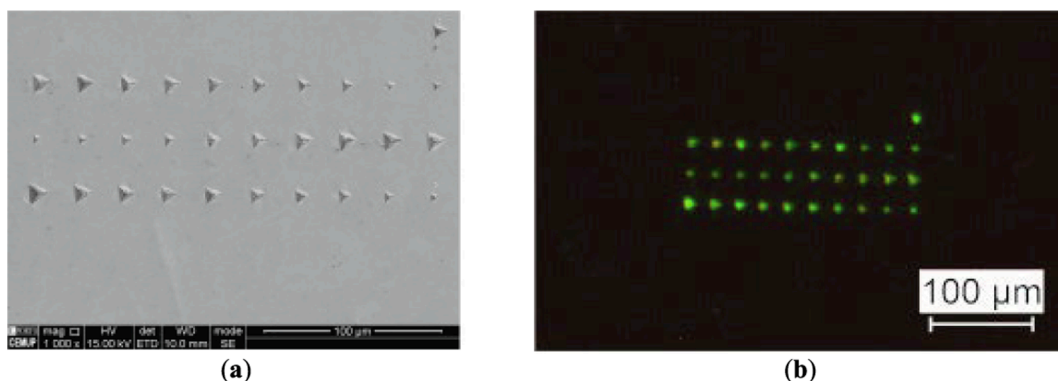


Fig. 71. Matrix of nanoindentations produced in AISI 316L, using *Rhodococcus erythropolis* bacterial cells (DCL14 strain), observed by: (a) SEM; (b) Fluorescence optical microscopy [417].

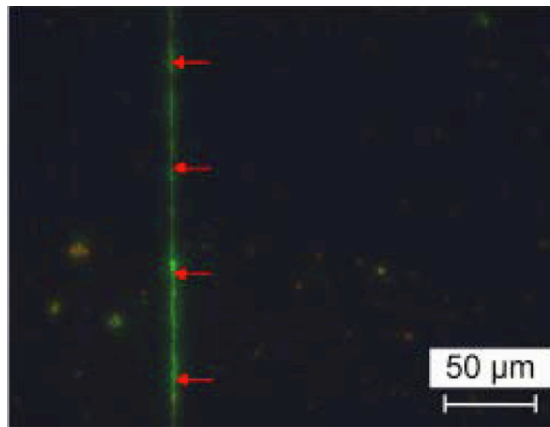


Fig. 72. Results of the test in the reference block Type 1 ISO 3452-3 using *Rhodococcus erythropolis* bacterial cells (DCL14 strain) [417].

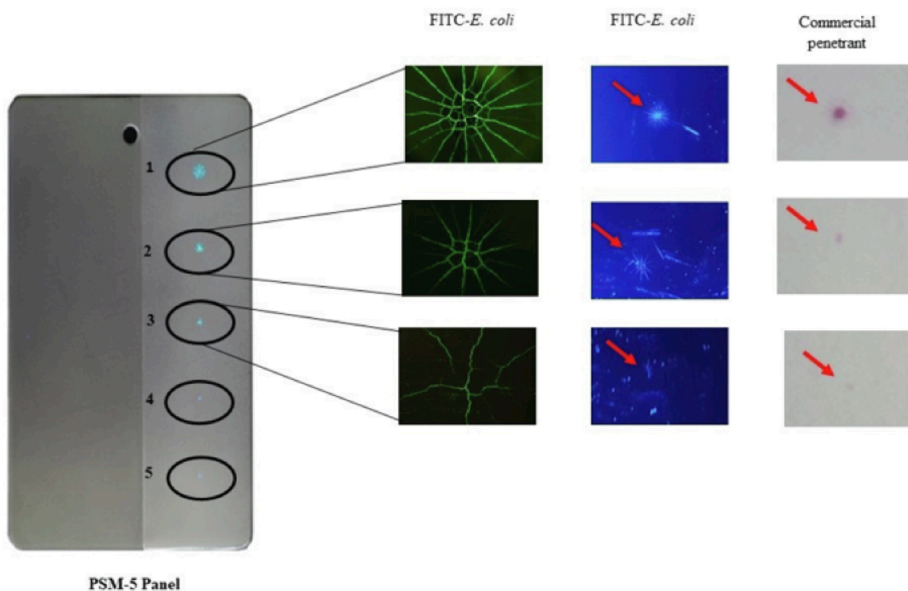


Fig. 73. PSM-5 panel with cracks and inspection results using FITC-E. coli and commercial dye penetrant [414].

7.3. Quantum dots fluorescent-penetrant testing

Quantum dots (Qdots) are semiconductor nanoparticles with optoelectronic properties that can transport electrons [421], used in fields like biomedical [422,423], and electronics [424].

According to Daneshvar et al. [412], quantum dots used as a fluorescent dye penetrant can detect cracks that are equal or bigger than 5 μm in weld joints. The authors created artificial cracks with widths between 5 and 10 μm and separated by 5 mm, in a 10 cm^2 aluminium plate. The surface of the sample was cleaned, then wetted by a colloidal solution, which stayed in the sample until the solvent evaporated. Then, excess material was removed, and the sample was analysed under an UV laser with emission line at 240 nm. Fig. 74 shows the scratched lines under UV light, which are clearly visible. Sezgin et al. [415], proposed the use of radiolabeled Qdots, i.e. synthesized Qdots (CdSe/ZnS) radiolabeled with $^{99\text{m}}\text{Tc}$ tracer, commonly used in medical analysis, to inspect weld beams, where radioactivity measurements are done by using a CdTe detector after radiolabeled Qdots are applied to the surface of the weld defect sample.

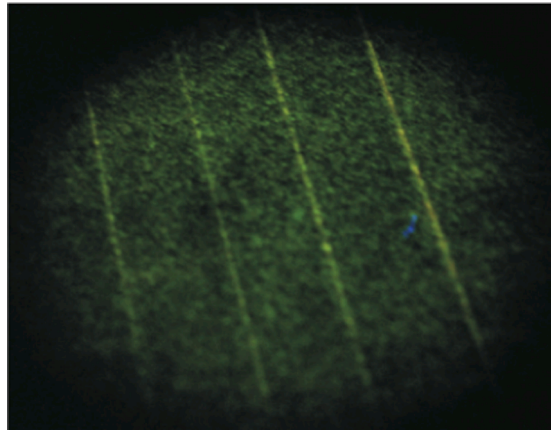


Fig. 74. Quantum dots used as fluorescent dye penetrant in detection of artificial cracks (with widths between 5 and 10 μm) exposed to a 240 nm UV light [412].

8. Replication metallography testing

Replication metallography is a technique of replicating the topography of a surface by applying a material, like a film, onto the surface. Replication techniques include surface replication and extraction replication, both are considered NDT techniques. The former provides an image of the surface topography of the material, while the latter gathers particles from the surface of the specimen. In the case of surface replication, the process consists of polishing and etching the surface of the specimen under inspection, followed by the application of a thin film onto the surface, which after removal is mounted in a support and examined under a microscope.

Surface replication is used in fields like power plants and petrochemical components to determine the component's remaining life. It is used for in-situ microstructural analysis, such as precipitate analysis, crack determination and creep damage, and can quantify defects, like voids, with less than 1 μm . An example of in-service creep cavitation damage in an X20 steam line, observed from a surface replica, is presented in Fig. 5 of Table 1 (§2.1). The advantage is that, unlike metallographic inspection, there is no need to cut and extract large samples from the component. However, crucial microstructural information is not available to help evaluate the component's remaining life, and this variant is only suitable for surface defects, having in mind that most early damage starts below the surface and is only detected on the surface shortly before fracture. Besides, some voids may form as a consequence of surface preparation procedures [2,425]. With extraction replication, there is the possibility to cut a small sample of the component if the following reparments, in order to not compromise its integrity, are not costly, or repairment is not necessary [426–430].

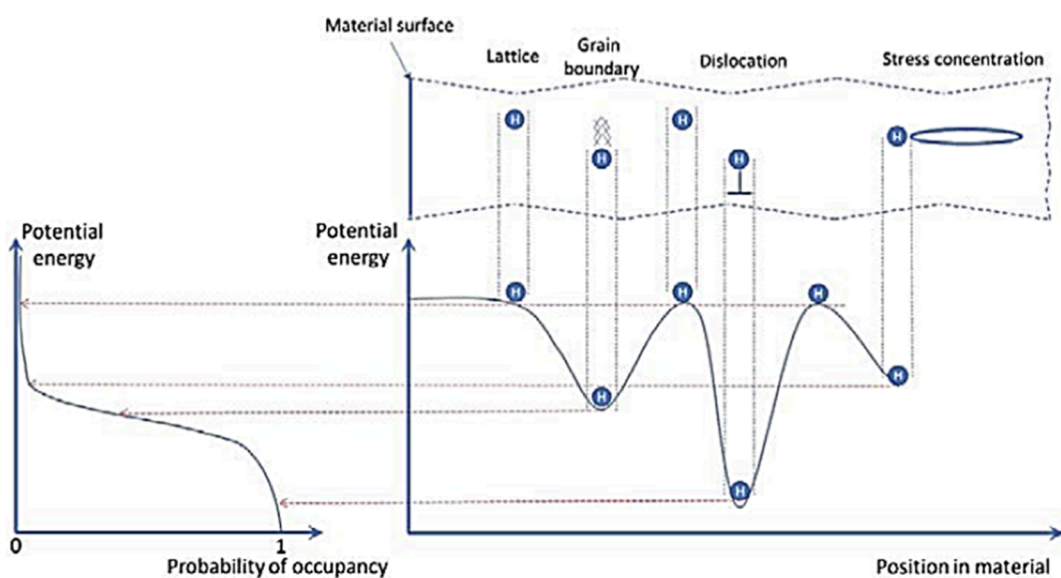


Fig. 75. Energy levels of hydrogen at different trapping sites [434].

9. Hydrogen-as-a-probe for testing

Hydrogen is known to be trapped by material imperfections, namely: vacancies, substitutional atoms, dislocations, grain boundaries, phase interfaces, second phases, precipitates, micro voids and cracks [63,431]. For a component's sample or replica, the concept of using hydrogen-as-a-probe for inspection of the material condition is based on scanning the hydrogen desorption over temperature, e.g. via Thermal Desorption Spectroscopy (TDS) technique. As different imperfections (or group of imperfections) will release the trapped hydrogen at different levels of activation energy (see Fig. 75), upon validation of the TDS results versus known imperfections, the hydrogen-as-a-probe is an ultimately sensitive NDT technique for small-scale defects. This technique takes advantage of the significant existing knowledge in the hydrogen-to-metal interaction. This phenomenon has been investigated since several decades ago, mostly on the scope of the hydrogen-to-metal interaction with respect to hydrogen embrittlement problem, reporting about the role of hydrogen trapping and diffusion on hydrogen-induced fracture mechanisms [432–438].

Fig. 76 presents the underlying mechanisms that lead to trapping of hydrogen and time-dependent fracture, with potential energy lower than in normal interstitial sites which slows down the diffusion of hydrogen [63,434].

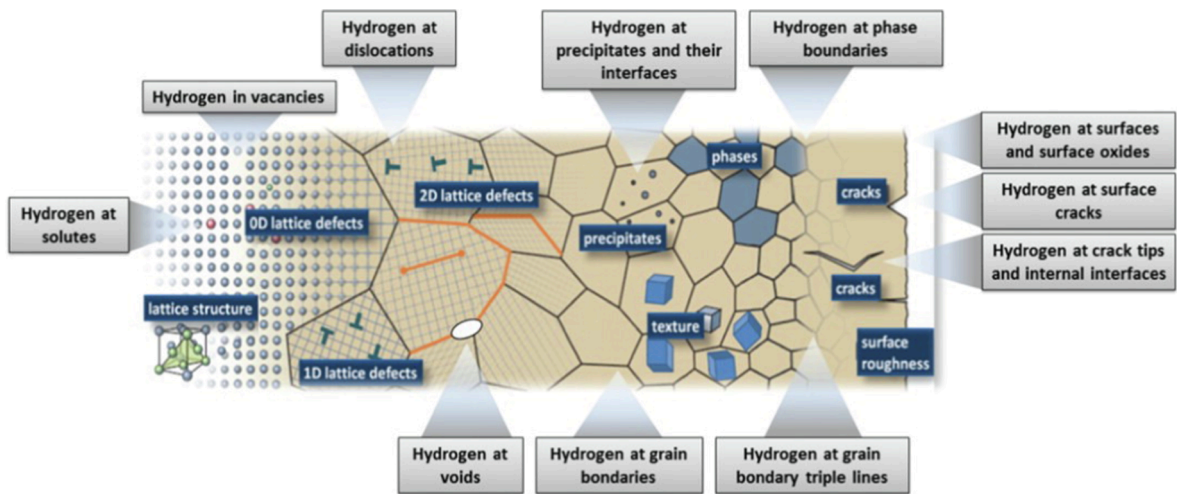


Fig. 76. Underlying mechanisms that lead to trapping of hydrogen and time-dependent fracture [63].

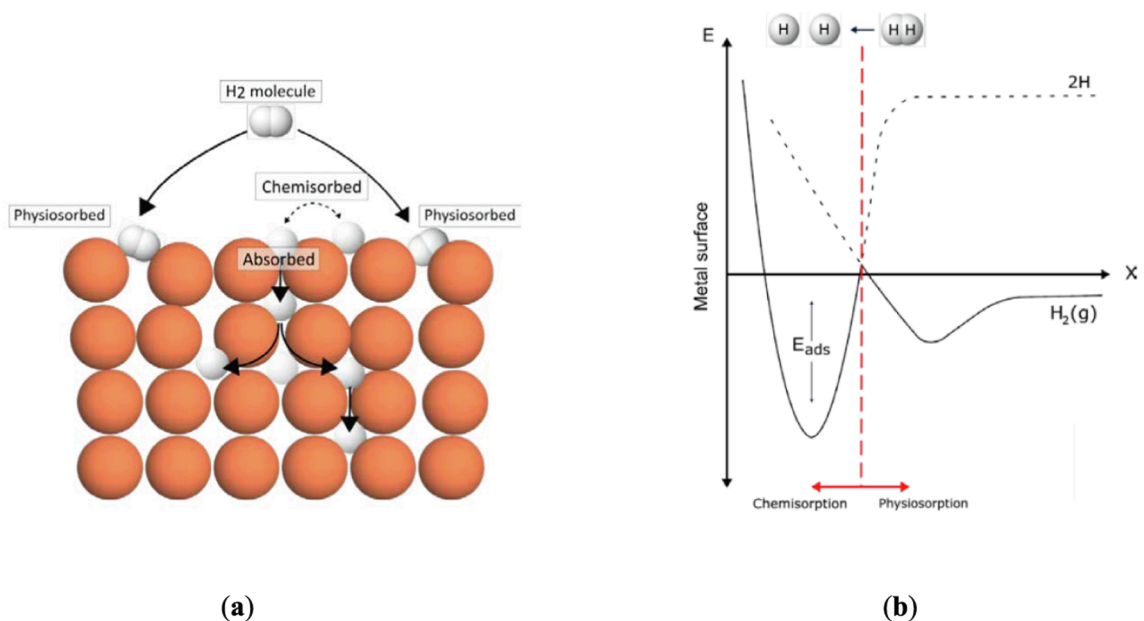


Fig. 77. Mechanisms that allow hydrogen entry into a material: (a) Schematic illustration of the chemisorption and physisorption process; (b) The energetic landscape, E, that a H2(g) molecule encounters when approaching a metal surface with a distance x [434].

Hydrogen interaction with metals is frequently defined by its permeability, diffusivity and solubility. These parameters are controlled by temperature and microstructure of the studied material with a significant impact from chemical composition, crystal structure, microstructural features and defects [439–443]. State of the art experimental techniques in combination with computation modelling allow to interpret the hydrogen behaviour in a multiphase structure evidencing a significant impact of interphase morphology on hydrogen diffusion and permeation leading to a potential application of the research method for analysis of material's condition [439,443].

The hydrogen uptake in metals can originate from the manufacturing process and from service environment exposure, e.g. via cathodic charging/protection, galvanic coupling, exposure to humid air, exposure to corrosive environments, use of long-life lubricants, palladium (Pd) plating process, electrochemical permeation technique, exposure to chloride solution in the case of AA7xxx aluminium alloys, during welding and when storing high-pressure gaseous hydrogen [441,444,445]. Besides, hydrogen's entry is dependent on factors like surface conditions, pressure and temperature [434]. For using hydrogen-as-a-probe as inspection technique, the TDS of the component's sample or replica can be applied to evaluate the hydrogen in as-original condition (i.e. hydrogen uptake from manufacturing and/or service), or in pre-charged condition.

Concerning the permeability, the mechanisms that allow hydrogen to enter a material are adsorption (surface phenomenon) and absorption (internal phenomenon). The adsorption stage is composed of the physisorption and chemisorption mechanisms, presented in Fig. 77a, and in which pressure plays an important role. Physisorption consists of a weak intermolecular force, van der Waals force, that occurs between the hydrogen molecule and the metal surface atoms, which increases slightly the potential energy as the molecule reaches out the surface, as shown in Fig. 77b [434,446]. Dissociative chemisorption happens when covalent bonds are formed between adsorbate (hydrogen atom) and adsorbent (metal surface atom), which is further simplified when the molecular hydrogen (hydrogen forms molecules in its natural state) dissociates into atoms, reducing the energy required to reach the surface [434,446]. Only in its atomic form can hydrogen diffuse interstitially into the materials.

The adsorption of hydrogen from a gaseous hydrogen source differs from that of an electrolytic hydrogen system source, the later expressed by the Hydrogen Evolution Reactions (HER) [434].

Following the adsorption stage, in the absorption phase the hydrogen assimilates into molecules in the bulk of the absorbent (metal), either through the interaction of the adsorbed hydrogen atom with water molecules or through the combination of two adsorbed hydrogen atoms. Not all atoms at the surface of the absorbent follow the process of absorption, e.g. they can recombine in the surface or subsurface of the material [434].

At elevated temperatures hydrogen has a high rate of transport within a metal, so it easily occupies a new interstitial site over great distances inside the bulk material.

Existing methods to analyse hydrogen content can be divided depending whether they allow to visualise the hydrogen distribution or to measure the absorbed hydrogen concentration [447]. Some methods are able to obtain information about lattice defects that would trap hydrogen, provide high spatial resolution, multi-scale microstructural mapping, quantify local hydrogen content, provide kinetic resolution and kinetic local analysis, and/or have a three-dimensional characterisation of the hydrogen distribution [63]. For instance, direct observation of hydrogen by Atom Probe Tomography (APT) analysis allows precise detection of crystallographic defects and grain boundaries, as shown by Tweddle et al. [448], for multicrystalline silicon. However, the method has a significant limitation in size of the sample (about $1 \mu\text{m}^3$) that obstructs the large volume defect analysis. Volume effect of dislocation density change on hydrogen diffusion and trapping was effectively measured by Scanning Kelvin Probe Force Microscopy [449]. Kelvin probe analysis shows to be effective for detection of hydrogen in the lattice, that modify the sample surface potential, with spatial resolution of about 50 nm, mapping the hydrogen escape intensity with 2D plot of specimen microstructure [449–451]. The direct volume defects characterization, as that in APT method, is however impossible. In order to assess the hydrogen trapping, effective hydrogen diffusivity, or desorption and binding energies, the TDS analysis is used, in combination with the previous methods or individually

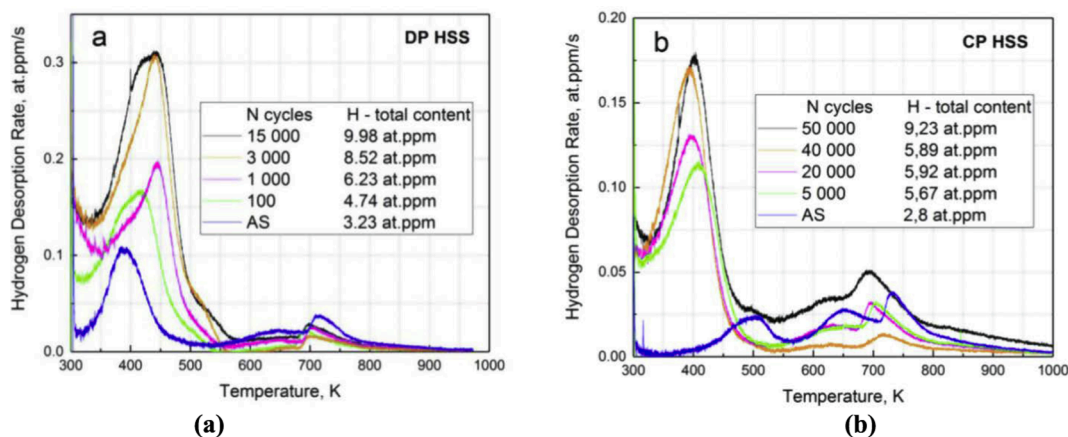


Fig. 78. TDS curves of hydrogen desorption rate from sheet metal steels measured in as-supplied state and after fatigue loading: (a) Dual phase steel; (b) Complex phase steel [435].

[436,451,452]. TDS is a technique that gives information about desorbed hydrogen from a sample bulk as a function of temperature.

The effect of microstructural variation of steels and alloys on hydrogen thermal desorption behaviour was studied widely during the last two decades, with the aim of understanding the relationship between specific microstructure features and the associated local hydrogen content. Nagumo et al. [453], considered the TDS as a promising tool for evaluation of defects produced by plastic deformation showing thermal desorption spectroscopy change as a function of deformation applied to pure iron and eutectoid steel caused apparently by increased dislocation density and vacancy clusters formation. Additional peak of hydrogen desorption at elevated temperatures for eutectoid steel studied after high plastic deformation (above 25%) is attributed to defects within cementite phase or supersaturated carbon in ferrite [453]. The phenomena of TDS change caused by plastic deformation was often attributed to vacancy/dislocation complexes and defects formation, and phase change affecting the hydrogen trapping and diffusivity [453–460]. In metastable TRansformation Induced Plasticity (TRIP) steels, the TDS shape variation is related to the deformation induced (from 5%) phase transformation enabling the quantitative approach in hydrogen behaviour prediction according to the steel phase fraction change [454,457]. Considering the complex structure of metastable S30408 austenitic stainless steel, the TDS reveals a complex relationship with applied deformation controlled by dislocations and stress-induced martensite [455]. The TDS of hydrogen is sensitive also to microstructural change caused by heat treatment procedures and alloying [442,447,457,461–467]. Thus, tempering at high temperatures decreases markedly the hydrogen trapping ability of Fe-0.2C steel, however, an increase of hydrogen concentration was observed at 600°C associated with recrystallization process and formation of new boundaries [461]. Microstructural change of high-strength steels caused by increase of austenizing temperature results in decrease of hydrogen uptake, measured by TDS and associated with refinement of grain size, and increase of Nb content in solution, as postulated by Liu et al. [464]. Materials subjected to the complex loading conditions, like creep and fatigue, reveal also unique hydrogen trapping behaviour [432,435,468]. Malitckii et al. [435] investigated the trapping of hydrogen accumulated into dual-phase and complex-phase High-Strength Steels (HSS), with strength of about 1200 MPa, under fatigue loading. The measurements reveal a complicated hydrogen trapping behaviour driven by hydrogen interaction with deformation defects and retained austenite. Hydrogen concentration seems to increase in the studied steels during the fatigue testing in the air without preceding hydrogen charging, as depicted in Fig. 78.

Creep-associated TDS shape variation was observed by Yamashita et al. [468], for heat resistant ferritic stainless steel (18Cr-2.5Si), that comprises apparently the creep damage with microstructural change such as precipitation/coarsening of NbC and change in dislocation density. Defects created during rotational bending fatigue of martensitic HSS were analysed by Nagumo et al. [432], using hydrogen-as-a-probe. The results evidence the formation of TDS peaks attributed to the point defects, presumably vacancies, at the final stage of the fatigue, and increased dislocation density at the early stage of the fatigue test [432]. Presence of high-density non-metallic inclusions (NMI) changes significantly the hydrogen uptake and trapping of steels [469–474]. Addition of Y₂O₃ nanoparticles (10–20 nm) to ferritic-martensitic matrix with intension to increase the material strength causes increased hydrogen content and TDS shape change from single to twin peak shape, as shown by Malitckii et al. [474]. Hydrogen trapping correlates with NMIs size and effective NMIs surface area rather than its volume fraction, as studied by Turk et al. [473], for ferritic steel with vanadium carbide precipitates of size 7.9 nm and 5.5 nm. No effect on the hydrogen trapping was observed in presence of W₂C in martensite steel matrix with size above 20 nm, as shown by Depover et al. [472], due to, probably, incoherent NMI interfaces. However, Wallaert et al. [469] reveals that the proper charging procedure, like charging in gaseous environment at elevated temperature, results in formation of high temperature TDS peak (450°C–650°C) of hydrogen release from incoherent interfaces of NbC and NbN particles with size up to 200 nm.

As these methods offer such microstructural sensitivity for small features and allow to understand the dependence of hydrogen diffusion and trapping on the microstructure of materials, they may render as useful allies for NDT to detect very small-scale defects in materials. Future work should address the reliability of applying the hydrogen-as-a-probe, to indicate the presence of grain-scale defects (nano- and micro-size cracks or voids) induced by in-service mechanisms, such as fatigue, creep, creep-fatigue and environmental.

10. Modelling, artificial intelligence and post-processing visualization

10.1. Analytical and numerical modelling

Both analytical and numerical modelling are useful tools to understand and predict the performance of NDT techniques in a specific component in order to save time in the inspection and increase the test's reliability. Analytical modelling is typically used for fast assessment and more fundamental support in application of NDT techniques, including ECT [475,476], and UT [477]. Numerical modelling enables modelling of nonlinear problems and complex geometries and boundary conditions, but has high computation time and requires software user expertise, especially in application of commercial software [478]. However, it's a powerful tool to aid in setting the inspections procedures, parameters and other conditions for demanding NDT techniques, such as ECT with array of probes and PAUT techniques, and even supporting in the development of dedicated solutions for new techniques aiming at small-scale defects [251,479]. For example, ANSYS software has been used to understand the thermal transient phenomena in active transient thermography [480,481], CIVA software has been used to simulate the UT inspection of planar backwall breaking defects [482] and complex component geometries [483], and COMSOL software has been used to simulate UT inspection in fiber reinforced materials [484] and high-energy pulse EMAT inspection [237].

Numerical modelling can be usually found applied for simulation of electromagnetic techniques [79,485–488], ultrasonic testing [239,251,489–491], infrared thermography [480,481,492], radiography [493,494], etc. There are even coupled analytical–numerical methods, such as the one presented by Mahaut et al. [495]. Additionally, these types of models are also used to estimate the critical size of defects, for instance, in the nuclear power industry [496]. For example, when modelling a MFL technique to predict defects,

Table 6
Recent articles about the application of artificial intelligence in NDT inspection.

Algorithm	Article	Inspection techniques / Defects	Material / Application
Multilayer perceptron	[524]	Transient Thermography	Aluminium / FSW
	[525]	UT and ECT	Aluminium
Single-hidden layer NN	[526]	UT	Low-carbon steel / Welded joints
Deep Learning	[527]	Acoustic Emission (AE)	Aluminium / Naval and Aerospace, etc
	[528]	PT / thermal fatigue cracks	Titanium alloy
	[529]	MFL	Magnetic material not specified
	[530]	Radiography / Weld defects	Welds on water pipes
	[531]	Ultrasonic Phase Array Imaging	Aluminium
	[514]	PT / Cracks, linear and healthy indications	Aerospace application
	[510]	UT / Thermal fatigue flaws	Austenitic 316L stainless steel
Recurrent NN	[532]	UT	Piezoelectric ceramic samples
CNN	[533]	AE	Thermal power plants
	[510]	UT	Austenitic 316L stainless steel
	[534]	X-ray microtomography	Polymer matrix composites
	[535]	Guided waves / Cracks	Aluminium
	[516]	Industrial camera / Surface micro defects	Stainless steel
	[536]	SEM images	Wafer
	[537]	PAUT	AISI 316L stainless steel
	[538]	Radiography	Aeronautics Engine
Region-based Convolutional Neural Networks (R-CNN)	[539]	Radiography	Aluminum Conductor Composite Core
	[540]	Edge collapse, corner collapse, white spots, glaze bubbles, glaze collapse, ink dripping	Ceramic tile
	[541]	Pin defects	Transmission line fittings
Genetic algorithm-back propagation NN	[542]	Crazing, inclusion, patches, pitted surface, rolled-in scale and scratches	Hot-rolled steel plates
	[543]	Laser UT	Aluminium alloy
Support Vector Machine	[544]	Ultrasonic guided waves	Glass/epoxy cross-ply laminated composites
	[545]	Defects in Resistance Spot Welding	High-strength steels / Automotive
	[517]	Microwave imaging	Multiple materials
	[546]	ECPT	Steel
	[547]	ECT	Ex-service reformer tube
	[548]	UT	Aircraft structures
K-Means Clustering	[549]	Microwave NDT	Glass Fibre Reinforced Polymer
	[550]	Enhanced truncated-correlation photothermal coherence tomography (eTC-PCT) / blind hole and cracks	Industrial materials
	[551]	UT	Aluminium and CFRP plates
Linear Discriminant Analysis	[552]	Resonant acoustic technique	Co-Cr additively manufactured lattice structures
Logistic Regression	[553]	Visual Inspection	Laminated composites / Aerospace
	[554]	Corrosion damage	Concrete
Random forest	[555]	Air permeability test, electrical resistivity test, UT / internal damage (corrosion)	Reinforced concrete
	[556]	Fluorescent PT	Titanium alloy plates
	[557]	MBN, magnetic incremental permeability (MIP) and ECT	Automotive plate steels
Generative Kernel Principal Component Thermography	[558]	Pulsed thermography	Carbon Fiber Reinforced Polymer
Mixed algorithms	[559]	UT	Balsa wood covered with fiberglass in a polymer matrix
	[560]	Wafer Bin Map images	Wafer
	[561]	Welding defects: stomatal, slag and incomplete penetration	Q345R standard defect test block
	[562]	THz	Ceramic matrix composite
	[563]	UT	Cast austenitic stainless steels
	[564]	ECT / corrosion	Aircraft structure
	[565]	UT	Aluminium and CFRP
	[566]	Thermography	Polylactic Acid (PLA) and Nylon (PA-12)
	[567]	Barker coded thermography	CFRP
[568]	Acoustic Emission	Composite	

(continued on next page)

Table 6 (continued)

Algorithm	Article	Inspection techniques / Defects	Material / Application
	[569]	AE	CFRP
	[570]	UT / fatigue damage	CFRP
	[571]	IRT	Electrofusion polyethylene joints
	[572]	AE	Fe250
	[573]	Laser UT	Metallic components
	[574]	CT	Ti-6Al-4 V
	[575]	Radiography	Aluminium

numerical modelling solves Maxwell's equations with appropriate boundary conditions in order to obtain the leakage field; analytical modelling gives a simple analysis and closed-form solution by assuming that defects are magnetic dipoles developed at the walls of the defect and whose magnetic field enables the calculation of MFL signals [478]. One study analysed the influence of the inducing frequency on characteristic vectors of the induction electromagnetic field, in order to design an ACFM prototype system with a U-shaped probe [497]. Yeom et al [498], used FEM simulation to study the phenomenon and characteristics of leaky Rayleigh waves. Tang et al. [499], used FEM to successfully simulate the detection of micro-crack defects in semiconductor silicon wafers using linear frequency modulated continuous laser. Su et al. [500], used FEM (COMSOL Multiphysics coupling software) to mimic the microdefect detection process using high frequency UT, i.e. acoustic microscopy imaging, and to calculate the acoustic propagation map for analysing the acoustic energy transmission. Yu et al. [501], also modelled the interaction mechanism between micro defects and high-frequency ultrasonic pulse method.

10.2. Machine learning, data fusion and post-processing visualization

Machine Learning (ML) is a technique of data analysis and a branch of artificial intelligence, based on the idea that systems can learn from data, identify patterns and make decisions with minimal human intervention, i.e. machines are trained how to learn. In statistical learning, most problems fall into one of two categories: supervised and unsupervised learning. In supervised learning, a statistical model is built to predict an output based on inputs and their associated outputs/labels, i.e. correct answers, from historical data to predict future events. In unsupervised learning, the inputs used have no supervising outputs, i.e. the real answer is not known, but as a statistical model, still allows to understand relationships in the data [502].

ML is being implemented in NDT inspections to aid in detecting and understanding signals and outputs from the performed inspections and help the evaluation process [503]. Examples include CT [504–506], infrared thermography [507,508], ultrasonic testing [210,509–511], eddy currents [512,513] and ACFM [376]. Artificial Neural Networks (ANN), a type of machine learning architecture modelled after biological neurons, are commonly used to aid in the detection of defects [514]. Throughout the article, many applications of PCA for post-processing of the output signal has been presented [188,361,515].

Other examples of studies regarding the application of artificial intelligence in NDT are presented in Table 6. For instance, Song et al. [516], has implemented Convolution Neural Networks (CNN) for the detection of micro defects on metal screw surfaces based on images taken by an industrial camera. Hoshyar et al. [517], proposed a Support Vector Machine-based (SVM) technique to identify cracks formed in the early stages, in civil structures, in order to reduce the risk of failure. Tripathi et al. [518], were able to differentiate microdamage with sizes ranging between 500 and 900 μm from time-domain and frequency-domain UT signal feature types, using several machine learning algorithms, and proposed a hybrid feature that can distinguish damages as small as 100 μm . Niu et al. [519], proposed a Surface Defect-Generation Adversarial Network (SDGAN), that uses generative adversarial networks (GANs), to generate images with defects in industrial defect-free images. Additionally, Taheri et al. [520], wrote a literature review paper about ML techniques for NDT inspection. Uhlig et al. [521], wrote a literature review about synthetic and augmented UT training data in NDT. Liu et al. [522], wrote a literature review about machine learning approaches for pipeline anomalies. Sun et al. [523], wrote a literature review about ML for the automated analysis of weld flaws from UT inspection.

Table 7

Recent articles about the application of data fusion in NDT inspection.

Algorithms	Article	NDT	Material / Defects
Average, difference, weighted average, Hadamard product, Dempster–Shafer rule of combination	[581]	UT, Induction thermography	Carbon fiber-reinforced epoxy / Artificial debonding defects
Regression, Neural network, ANFIS model	[582]	Rebound number, UPV	Bricks
Logistic regression	[554]	Ground penetrating radar (GPR), half-cell-potential, Wenner resistivity, microwave moisture	Reinforced concrete / Corrosion-based defects
Maximum amplitude, ensemble averaging, weighted averaging, Bayesian analysis, Dempster–Shafer theory	[583]	ECT, IR	Carbon fibre reinforced composite / low energy impact damage
Ordered weighted averaging	[584]	Hysteresis loop, Hall effect, ECT	Powder metallurgical steels
Tippett's method, Fisher's method, best view and variants, matched filter and variants	[554]	Multi-element ultrasonic arrays	Copper / Voids
Fuzzy logic with inference operators	[578]	Eddy currents, Ultrasound	Aluminium, FSW defects

Data fusion is the process of combining different data sources, that vary in information, size, and behaviour, into a single model to create more coherent and useful information than that provided by the individual data sets [576,577]. In NDT, data fusion uses data from complimentary techniques, like ECT, Radiography and UT, to not only create diverse and redundant data sets but to avoid uncertainty, lack of precision, and conflicts of information [578].

Data fusion can also work as way of gathering different information from ML models. For example, Cormerais et al. [579], combined data from UT and ECT inspections on an aluminium block with side drill holes by means of ANN in order to apply a data fusion algorithm to these NDT techniques and take advantage of their different assets. Oesch et al. [580], developed a framework to identify

Table 8

Existing NDT techniques with micro and/or nano spatial resolution and type of location of the targeted defects.

Technique	Surface defects	Subsurface defects	Internal defects
X-ray CT			[105,106,111,112,114–119,122]
X-ray CL			[123,128,132]
Micro-LLT, micro-LST, TTI, SThM, BCLIT, FMT		[141–149,151–153,159,499]	
Micro-Raman spectroscopy	[23,154,156–158]		
Digital holography, ESPI		[188,189,197,198]	
THz imaging			[174,178]
SAM		[46,224,225,228–230]	
UPV, Ultrasonic guided waves, EMAT, PA, AE			[222,223,237,239,240,242–244] [274–312]
LUT, AUBT, UIT, UIRT		[2,242,246,247,249–254,258–260]	
ECM, GMR, TMR, IONic probe, MWM-Arrays, ECPT, ACFM, MFL	[314,321–325,327–329,331,333,336–342,344,360,361,372,382–384]		
Magnetic particles - ferrofluids		[380]	
Driven bacterial cells, Qdots, Replication metallography	[2,413,414,416,417,425,426,428–430]		

Table 9

Existing NDT techniques with micro and/or nano spatial resolution regarding the material and size of the component, types of defects and applications.

Technique	Materials	Types of defects	Smallest order of size of detected defects
X-ray CT	Composites, wood-based materials, metals	Pores, voids, cracks, infiltrations	~1 µm
X-ray CL	Metals used in small electronic devices, composites, polymers	Pores, voids, cracks	Order of ~ 10 µm
Micro-LLT, micro-LST TTI	Steel, polymer, composites Metals like copper, lithium, nickel and aluminum, and some plastics (materials used in electronic devices)	Micro-porosities, cracks Hotspots caused by micro-defects	Order of ~ 100 µm Order of ~ 1 µm
SThM, Micro-Raman spectroscopy	GaN	Thermal conductivity, heat dissipation, residual stresses	Order of ~ 50 nm
BCLIT	Silicon crystal, mild steel	Micro cracks, artificial blind holes	Order of ~ 1 mm
Digital holography, ESPI	Polymer, glass, materials used in PV cells	Micro fibres, line scratches and digs	Order of ~ 10 µm
THz imaging	Copper, PLA	Small protrusions, air gaps, water infiltrations, artificial square defects	Order of ~ 10 µm
UPV, TOFD, TFM	Stainless steel, A204 Gr B	Porosity, pore shape and texture	Order of ~ 10–100 µm
SAM	Materials used in electronic devices	Laminar cracks, voids, delaminations, solder joints	
Ultrasonic guided waves, EMAT, PA	Steel, Aluminium, Titanium	Micro-cracks, deep bottom holes, corrosion	Order of ~ 100 µm
LUT, AUBT	Aluminium, steels	Flat-bottomed holes, porosity, surface notches, micro-cracks, HTHA-induced defects	Order of ~ 10 µm
UIT, UIRT	Carbon steel, stainless steel, aluminium, polymer, composites	SCC micro defects, fatigue cracks, porosities	Order of ~ 100 µm
AE	Steels, concrete, composites, ice	Fatigue damage, corrosion damage, matrix cracking and fibre breakage in composites, phase transformations, precipitation fracture, cooldown cracking and thermal stresses	Order of ~ 10 µm
GMR, TMR	Stainless steel, titanium, aluminium	Cracks, surface notches and holes	Order of ~ 100 µm
IONic probe, MWM-Arrays	Aluminium, stainless steel, graphite, GLARE® composite	FSW root defects, fatigue damage, cold work	Order of ~ 10–100 µm
ECPT, ACFM	CFRP, Q235 mild steel	Cracks, low impact damage, cylindrical hole defects	Order of ~ 100 µm–1 mm
MFL	Ferromagnetic materials, carbon steel	Micro-cracks, artificial cylindrical-hole defects	Order of ~ 10 µm
Magnetic particles - ferrofluids	Magnetic materials	Surface indentation (ring defect)	Order of ~ 10 µm
Driven bacterial cells	Stainless steel, aluminium, copper	Micro and nano indentations, cracks	Order of ~ 10 µm
Qdots	Aluminium	Cracks	Order of ~ 10 µm

crack-like structures and measuring their characteristics such as crack extension (relative surface area) and surface connectivity, from large CT scan data from different sample types. Hu et al. [515], proposed a multi-feature fusion deep network to enhance the detection rate and extract both the spatial and temporal information for automated IRT. Table 7 presents a selection of other recent studies regarding the application of data fusion to NDT applications.

As mentioned in the beginning and throughout this article, after the applied energy interacts with the material properties and condition, the resulting output signal is processed and evaluated. Many processing algorithms have been mentioned so far, apart from PCA, like sparse reconstruction [229,230], Fourier transform method [147], and modified Feldkamp–Davis–Kress (FDK) reconstruction method [111].

Mosavi et al. [585–587], proposed an ultrasonic-based imaging technique, Temporal-enhanced Ultrasound (TeUS), that uses machine learning approaches to extract information from a temporal sequence of radio frequency (RF) data captured from a fixed material, using conventional ultrasound imaging data. Tang et al [588], applied inter-frame difference-multi-frame cumulative average, PCA, Fourier transform, and logarithmic polynomial fitting to process a sequence of FMT images. Subbarao et al. [589], applied a correlation-based pulse compression system for enhancing the detection of defects like voids, inclusions and cracks, using FMT. Arora et al. [590], applied a Gaussian Weighted Chirp (GWC) approach to FMT data to detect subsurface flat bottom holes. Lakha et al. [591], proposed a pattern recognition image processing using Singular Value Decomposition (SVD) that can aid interferometry NDT techniques. Petrov et al. [592], developed a Synthetic Aperture Focusing Technique (SAFT) to improve the accuracy and precision of detection of flaws in welds, using UT. Kreidl et al. [593], addressed algorithms for noise reduction of UT signal based on cross-correlation function.

11. Overview analysis

Table 8 presents a list of articles that address NDT techniques with micro and/or nano spatial resolution, most of them reviewed in this article. Table 9 gives a review of the NDT techniques presented in this article and their application regarding the material and size of the component, types of defects and applications.

12. Conclusions

Based on a large pool of peer-reviewed scientific publications, this work investigates the multiphysical challenges and need for detecting and characterizing small-scale defects in a wide range of engineering materials. Although some case-studies include larger defect thresholds, the main focus is on the few micrometre and nanometre range. The reliable identification of these small-scale defects contributes for structural safety of critical components in high-value applications. The sensitivity and reliability in detecting these defects is explored for large set of multiphysical-based Non-Destructive Testing (NDT) techniques, including emergent solutions and digital toolsets of modelling and signal processing. From this in-depth literature review work, the following conclusions are drawn:

12.1. Nature of small-scale defects in different engineering materials and need of reliable detection

The detrimental effect of defects, from their critical size, morphology and location, depends on the material properties, component geometry, system-level design features, and application conditions. As shown in chapter 2, defects as small as 10 μm already decrease the component's performance and/or lead to its fracture under certain conditions. The main multiphysical challenges for NDT-based detection and characterization of small-scale defects are:

- for metallic components, the small size in-length of zero-volume defects, e.g. micro cracks, where the surface asperities are closed together, and small volume of early creep damage, and other micro-voids, at grain boundaries. The quasi-zero volume condition of these defects, with negligible mass, prevents relevant amount of absorption of electromagnetic radiation energy. The small size dimension of all these defects, namely equal or smaller than grain size, prevents relevant sensitivity of ultrasonic waves and electromagnetic energy, without excessive scattering and attenuation, inherent to the high-frequency-based energy propagation. The in-service generated early damage and small-scale defects (e.g. early creep, creep-fatigue and oxidation), whose generation rate are inversely proportional to defect size in the early stages (i.e. the early damage spreads out before growing in size), emits too small energy waves to be detected by conventional acoustic emission.
- for other engineering materials, such as polymeric-based materials and ceramics, the negligible electric conductivity and magnetic permeability, prevent fully, or at least straightforward, application of electromagnetic energy-based techniques. Additionally, for polymeric materials and composites, there is a significant attenuation of the sound waves, that decreases the amplitude of ultrasonic signal and makes it difficult to detect small defects. In the polymeric-based materials, micro-voids, micro-sized delamination, matrix cracking, debonding, fibre breakage, and high-contrast variation between different fibres in composites, makes small size defects in this group of materials challenging to detect with electromagnetic radiation energy.

12.2. Outstanding NDT solutions addressing the need for reliable inspection of small-scale defects

Among the considered solutions for the reliable inspection via NDT of small-scale defects, the outstanding technological approaches and digital methods are now emphasized, within the following groups advanced and emerging stand-alone NDT techniques; approaches based on hybrid NDT techniques; NDT techniques paired with advanced post-processing digital algorithms; and Machine

Learning-aided NDT.

Advanced and emerging stand-alone NDT techniques:

- Time-of-Flight Diffraction (TOFD) at 7.5 MHz, that detected early damage (10 μm diameter) induced by High Temperature Hydrogen Attack (HTHA), with a signal-to-noise ratio above 12 dB;
- Thermoreflectance Thermal Imaging (TTI), that detected a defect of less than 1 μm in a polysilicon micro-resistor;
- Advanced eddy currents probes, like the IOnic probe, that detected non-continuous Al_2O_3 particles alignment along a path of approximately 60 μm of length, within a dynamically recrystallized Al-alloy domain;
- Micro Magnetic Bridge Probe (MMBP) used in Magnetic Flux Leakage (MFL) that detected micro-cracks with width between 60 and 80 μm and depth as small as 7 μm ;
- Novel surface techniques like driven-bacterial cells, that were able to identify micro and nano-hardness indentations (as small as 0.6 μm depth and 5.3 μm side length) and micro-cracks (0.5 μm wide and 10 μm depth), and Quantum dots (Qdots), that identified micro-cracks with width between 5 and 10 μm ;
- Hydrogen-as-a-probe, a recently proposed and trending technique, that may prove suitable for the inspection of small-scale defects, as it offers microstructural-level sensitivity, e.g. defects induced by plastic deformation, cyclic loading and heat treatment procedures, with the aid of quantitative and qualitative methods for detection of hydrogen desorption.

Approaches based on hybrid NDT techniques:

- Computed Tomography (CT) with Computed Laminography (CL), to take advantage of the resolution of CT in each direction (μm and nm) of the specimen and the better resolution of CL images along the plane parallel to the specimen's face;
- Scanning Thermal Microscopy (SThM) with Raman Spectroscopy, that detected the heat dissipation in GaN nanowires with diameters between 40 and 60 nm;
- Barker Code Laser Infrared Thermography (BCLIT) and other infrared thermography variants, like Ultrasonic Infrared Thermography (UIT) and Eddy Current Pulsed Thermography (ECPT), when paired with coded signals during the acquisition phase to improve the signal-to-noise ratio and increase sensitivity (mm- μm range).

NDT techniques paired with advanced post-processing digital algorithms:

- CT with a modified Feldkamp–Davis–Kress (FDK) reconstruction method;
- Scanning Acoustic Microscopy (SAM) with a blind sparse reconstruction method;
- Ultrasonic Phased Array (PA) with Total Focusing Method (TFM)-based post-processing algorithm;
- Micro-laser with lock-in method paired with signal processing using principal component thermography (PCT) and Fourier transform;
- Ultrasound Lock-in Infrared Thermography (UIRT) with an interference-based joint reconstruction method.

Machine Learning-aided NDT:

- Machine learning algorithms have also been shown to significantly aid NDT techniques like CT, Infrared Thermography, Ultrasonic testing and Electromagnetism testing, in analysing and interpreting complex data patterns in the micrometre range.
- The Machine Learning algorithms found to be used include Deep Learning (DL), Convolutional Neural Networks (CNN), K-Means Clustering (KMC), Random Forests (RF), Support Vector Machine (SVM), Principal Component Analysis (PCA), K-Nearest Neighbour (KNN) and Artificial Neural Networks (ANN).

Several proposed techniques already reach the envisaged threshold of detectability for small-scale defects, in the most used engineering materials. Best solutions are mostly provided by integration of advanced NDT techniques aided by advanced post-processing of signal. In terms of reliability, more case studies for these groups of outstanding NDT approaches should be published, especially targeting in-service defects, aiming for safer and more sustainable use of high-value engineering systems.

Funding

This research was funded by the Academy of Finland, via project no. 325108 (New high-resolution non-destructive methods for assessment of early damage in advanced welded steels for high-temperature applications with extended life: EARLY), and by the Portuguese Fundação para a Ciência e a Tecnologia (FCT - MCTES), via the projects UIDB/00667/2020 and UIDP/00667/2020 (UNIDEMI).

CRedit authorship contribution statement

Maria Inês Silva: Conceptualization, Data curation, Writing – original draft, Writing – review & editing. **Evgenii Malitckii:** Data curation, Writing – review & editing. **Telmo G. Santos:** Supervision, Writing – review & editing. **Pedro Vilaça:** Conceptualization, Supervision, Writing – review & editing.

Declaration of Competing Interest

The authors declare that they have no known competing financial interests or personal relationships that could have appeared to influence the work reported in this paper.

Data availability

Since this is a review article, the availability of the data depends on the original paper policy.

Acknowledgments

The authors would like to thank the Academy of Finland for its financial support via project 325108 and Fundação para a Ciência e a Tecnologia (FCT - MCTES) for its financial support via the projects UIDB/00667/2020 and UIDP/00667/2020 (UNIDEMI).

References

- [1] Simandjuntak S, Shibli A. Practical use of defect assessment procedures for industrial component integrity assessment. *Mater High Temp* 2011;28(3):245–53. <https://doi.org/10.3184/096034011X13124750650714>.
- [2] Sposito G, Ward C, Cawley P, Nagy PB, Scruby C. A review of non-destructive techniques for the detection of creep damage in power plant steels. *NDT E Int* 2010;43(7):555–67. <https://doi.org/10.1016/j.ndteint.2010.05.012>.
- [3] Holdsworth S. Creep-fatigue failure diagnosis. *Materials* 2015;vol. 8(no. 11) MDPI AG, pp. 7757–7769, 2015, doi: 10.3390/ma8115418.
- [4] Murakami Y. Material defects as the basis of fatigue design. *Int J Fatigue Aug.* 2012;41:2–10. <https://doi.org/10.1016/J.IJFATIGUE.2011.12.001>.
- [5] Benjamin AC, Freire JLF, Vieira RD, Cunha DJS. Interaction of corrosion defects in pipelines - Part 1: Fundamentals. *Int J Press Vessel Pip Aug.* 2016;144: 56–62. <https://doi.org/10.1016/j.ijpvp.2016.05.007>.
- [6] International Atomic Energy Agency, “Non-destructive testing: A guidebook for industrial management and quality control personnel;” 1999. Accessed: 04, 2021. [Online]. Available: http://inis.iaea.org/Search/search.aspx?orig_q=RN:31005449.
- [7] Guo TL, Han ZX. Repairing surface fatigue damage of the metal material by heat treatment. *Adv Mat Res* 2011;154–155:425–8. <https://doi.org/10.4028/www.scientific.net/AMR.154-155.425>.
- [8] Walker B, Walker R. Aircraft engine rotor repaired with microstructural enhancement. US10865644, Dec. 20; 2020.
- [9] Ahn TH, Kim HG, Ryou JS. New surface-treatment technique of concrete structures using crack repair stick with healing ingredients. *Materials (Basel)* 2016;9 (8):Aug. <https://doi.org/10.3390/ma9080654>.
- [10] Kumar S, et al. Effect of atmospheric pressure plasma treatment for repair of polymer matrix composite for aerospace applications. *J Compos Mater* May 2016; 50(11):1497–507. <https://doi.org/10.1177/0021998315594230>.
- [11] Wang S, Kang J, Zhang X, Guo Z. A study on the effect of ultrasonic treatment on the microstructure of Sn-30 wt.% Bi Alloy. *Mater* 2018; Vol. 11, Page 1870, vol. 11, no. 10, p. 1870, Oct. 2018, doi: 10.3390/MA11101870.
- [12] Riedel E, Horn I, Stein N, Stein H, Bähr R, Scharf S. Ultrasonic treatment: A clean technology that supports sustainability in casting processes. *Proc CIRP* 2019; 80:101–7. <https://doi.org/10.1016/j.procir.2019.01.110>.
- [13] Eskin GI. Principles of ultrasonic treatment: application for light alloys melts. *Adv Perform Mater* 1997; 42, vol. 4, no. 2, pp. 223–232, 1997, doi: 10.1023/A: 1008603815525.
- [14] Liburdi J, Lowden P, Ellison K. Powder metallurgy repair technique. US5156321A, Aug. 27; 1990.
- [15] Spitaler J, Estreicher SK. Perspectives on the theory of defects. *Front Mater* Dec. 2018;5:70. <https://doi.org/10.3389/fmats.2018.00070>.
- [16] Planck M, Debye PJW, Nernst W, Smoluchowski M, Sommerfeld A, Lorentz HA. *Vorträge über die kinetische theorie der materie und der elektrizität*. Berlin: B. G. Teubner; 1914.
- [17] Peierls R. Zur kinetischen Theorie der Wärmeleitung in Kristallen. *Ann Phys* 1929;395(8):1055–101. <https://doi.org/10.1002/ANDP.19293950803>.
- [18] Rodriguez P. Sixty years of dislocations. *Bull Mater Sci* 1996;19(6):857–72.
- [19] Acar P. Recent progress of uncertainty quantification in small-scale materials science. *Prog Mater Sci* 2021;117:100723. <https://doi.org/10.1016/j.pmatsci.2020.100723>.
- [20] Di Gianfrancesco A. Technologies for chemical analyses, microstructural and inspection investigations. In: *Materials for ultra-supercritical and advanced ultra-supercritical power plants*, Elsevier Inc.; 2017. p. 197–245.
- [21] Hsu JWP. Near-field scanning optical microscopy studies of electronic and photonic materials and devices. *Mater Sci Eng R Reports* 2001;33(1):1–50. [https://doi.org/10.1016/S0927-796X\(00\)00031-0](https://doi.org/10.1016/S0927-796X(00)00031-0).
- [22] Huckabay HA, Armendariz KP, Newhart WH, Wildgen SM, Dunn RC. Near-field scanning optical microscopy for high-resolution membrane studies. *Methods Mol Biol* 2013;950:373–94. https://doi.org/10.1007/978-1-62703-137-0_21.
- [23] Yin JF, Bai Q, Zhang B. Methods for detection of subsurface damage: A review. *Chin J Mech Eng (English Ed.)* 2018; vol. 31, no. 3, pp. 1–14, doi: 10.1186/s10033-018-0229-2.
- [24] Meola C, Boccardi S, maria Carlomagno G. Nondestructive evaluation. In: *Infrared thermography in the evaluation of aerospace composite materials*, Woodhead Publishing; 2017. p. 25–56.
- [25] Crowe GV. *An introduction to nondestructive testing. Second: American Society for Nondestructive Testing; 2009.*
- [26] Bogue R. New NDT techniques for new materials and applications. *Assem Autom Jul.* 2012;32(3):211–5. <https://doi.org/10.1108/01445151211244339>.
- [27] McGonagle WJ, editor. *International Advances in Nondestructive Testing*, vol. 15. Montreux: Gordon and Breach Science Publishers; 1990.
- [28] McMaster RC. *Nondestructive Testing Handbook, Volume 1*. New York: The Ronald Press Company; 1963.
- [29] McMaster RC. *Nondestructive Testing Handbook, Volume 2*. New York: The Ronald Press Company; 1963.
- [30] Ma Z, Zhang W, Luo Z, Sun X, Li Z, Lin L. Ultrasonic characterization of thermal barrier coatings porosity through BP neural network optimizing Gaussian process regression algorithm. *Ultrasonics* 2020;100. <https://doi.org/10.1016/j.ultras.2019.105981>.
- [31] Lee CS, Zhang GM, Harvey DM, Qi A. Characterization of micro-crack propagation through analysis of edge effect in acoustic microimaging of microelectronic packages. *NDT E Int* 2016;79:1–6. <https://doi.org/10.1016/j.ndteint.2015.11.007>.
- [32] Kim DS, Čopar S, Tkalec U, Yoon DK. Mosaics of topological defects in micropatterned liquid crystal textures; 2018. [Online]. Available: <https://www.science.org>.
- [33] Lu Y, Yang C, Liu Y, Yang K, Lin J. Characterization of lattice defects and tensile deformation of biomedical Co29Cr9W3Cu alloy produced by selective laser melting. *Addit Manuf* 2019;30. <https://doi.org/10.1016/j.addma.2019.100908>.
- [34] Zhang X, Hao Y, Shangguan H, Zhang P, Wang A. Detection of surface defects on solar cells by fusing Multi-channel convolution neural networks. *Infrared Phys Technol* 2020;108. <https://doi.org/10.1016/j.infrared.2020.103334>.
- [35] Zhang XQ, Wang XL, Liu R. Effects of microfabrication defects on the performance of gas bearings with High aspect ratio in microengine. *Tribol Int* 2012;48: 207–15. <https://doi.org/10.1016/j.triboint.2011.12.003>.

- [80] Antin K-N, Laukkanen A, Andersson T, Smyl D, Vilaça P. A multiscale modelling approach for estimating the effect of defects in unidirectional carbon fiber reinforced polymer composites. *Materials* (Basel) 2019;12(12):1885. <https://doi.org/10.3390/ma12121885>.
- [81] Machado MA, Antin KN, Rosado LS, Vilaça P, Santos TG. Contactless high-speed eddy current inspection of unidirectional carbon fiber reinforced polymer. *Compos Part B Eng Jul*. 2019;168:226–35. <https://doi.org/10.1016/j.compositesb.2018.12.021>.
- [82] Tanzi MC, Farè S, Candiani G. Mechanical properties of materials. *Foundations of Biomaterials Engineering*, Elsevier 2019:105–36.
- [83] Awaja F, Zhang S, Tripathi M, Nikiforov A, Pugno N. Cracks, microcracks and fracture in polymer structures: formation, detection, autonomic repair. *Prog Mater Sci* 2016;83:536–73. <https://doi.org/10.1016/j.pmatsci.2016.07.007>.
- [84] Kaiser H, Karbhari VM, Sikorsky C. Rehabilitation of concrete structures using fibre-reinforced polymer composites: identifying potential defects. *Durab Compos Civ Struct Appl* 2007;284–323. <https://doi.org/10.1533/9781845693565.2.284>.
- [85] Hakim IA, Donaldson SL, Meyendorf NG, Browning CE. Porosity effects on interlaminar fracture behavior in carbon fiber-reinforced polymer composites. *Mater Sci Appl* 2017;08(02):170–87. <https://doi.org/10.4236/msa.2017.82011>.
- [86] Xu D, et al. Delamination analysis of carbon fiber/epoxy composite laminates under different loading rates using acoustic emission. *J Fail Anal Prev* 2019;19(4):1034–42. <https://doi.org/10.1007/s11668-019-00691-1>.
- [87] Stark G. X-ray. *Encyclopædia Britannica* 2020.
- [88] Stark G. Gamma ray. *Encyclopædia Britannica* May 2020.
- [89] Rebuffel V, Dintin JM. Dual-energy X-ray imaging: Benefits and limits. *Insight Non-Destructive Test Cond Monit* 2007;49(10):589–94. <https://doi.org/10.1784/insi.2007.49.10.589>.
- [90] Ozcete E, Boydak B, Ersel M, Kiyas S, Uz I, Cevrim O. Comparison of conventional radiography and digital computerized radiography in patients presenting to emergency department. *Turkish J Emerg Med* 2015;15(1):8–12. <https://doi.org/10.5505/1304.7361.2014.90922>.
- [91] Sima F, Ristoscu C, Duta L, Gallet O, Anselme K, Mihailescu IN. Laser thin films deposition and characterization for biomedical applications. In: *Laser Surface Modification of Biomaterials: Techniques and Applications*. Elsevier Inc.; 2016. p. 77–125.
- [92] Holbrook RD, Galyean AA, Gorham JM, Herzog A, Pettibone J. Overview of Nanomaterial Characterization and Metrology. In: *Frontiers of Nanoscience*, vol. 8, Elsevier Ltd, 2015, pp. 47–87.
- [93] Bera MK, Bu W, Uysal A. Liquid Surface X-Ray Scattering. In: *Physical Chemistry of Gas-Liquid Interfaces*. Elsevier; 2018. p. 167–94.
- [94] Martínez-Criado G, Borfecchia E, Mino L, Lamberti C. Micro- and Nano-X-ray Beams. In: *Characterization of Semiconductor Heterostructures and Nanostructures*. Second Edition, Elsevier B.V.; 2013. p. 361–412.
- [95] Villarraga-Gómez H, Herazo EL, Smith ST. X-ray computed tomography: from medical imaging to dimensional metrology. *Precis Eng* 2019;60:544–69. <https://doi.org/10.1016/j.precisioneng.2019.06.007>.
- [96] Lu X, et al. 3D microstructure design of lithium-ion battery electrodes assisted by X-ray nano-computed tomography and modelling. *Nat Commun* 2020;11(1):1–13. <https://doi.org/10.1038/s41467-020-15811-x>.
- [97] Ran A, et al. A gradient screening approach for retired lithium-ion batteries based on X-ray computed tomography images. *RSC Adv* 2020;10(32):19117–23. <https://doi.org/10.1039/d0ra03602a>.
- [98] Latief FDE, Fauzi U, Irayani Z, Dougherty G. The effect of X-ray micro computed tomography image resolution on flow properties of porous rocks. *J Microsc* 2017;266(1):69–88. <https://doi.org/10.1111/jmi.12521>.
- [99] Zenyuk IV. Bridging X-ray computed tomography and computational modeling for electrochemical energy-conversion and -storage. *Curr Opin Electrochem* 2019;vol. 13. Elsevier B.V., pp. 78–85, 01, doi: 10.1016/j.coelec.2018.1.016.
- [100] Naresh K, Khan KA, Umer R, Cantwell WJ. The use of X-ray computed tomography for design and process modeling of aerospace composites: A review. *Mater Des* 2020;190:108553. <https://doi.org/10.1016/j.matdes.2020.108553>.
- [101] Dilonardo E, Nacucchi M, De Pascalis F, Zarrelli M, Giannini C. High resolution X-ray computed tomography: A versatile non-destructive tool to characterize CFRP-based aircraft composite elements. *Compos Sci Technol* 2020;192:108093. <https://doi.org/10.1016/j.compscitech.2020.108093>.
- [102] Chaurand P, et al. Multi-scale X-ray computed tomography to detect and localize metal-based nanomaterials in lung tissues of in vivo exposed mice. *Sci Rep* 2018;8(1):1–11. <https://doi.org/10.1038/s41598-018-21862-4>.
- [103] Gregg CL, Recknagel AK, Butcher JT. Micro/nano-computed tomography technology for quantitative dynamic, multi-scale imaging of morphogenesis, in *Methods in Molecular Biology* 2015;vol. 1189:47–61.
- [104] Siddique S, et al. Computed tomography for characterization of fatigue performance of selective laser melted parts. *Mater Des* 2015;83:661–9. <https://doi.org/10.1016/j.matdes.2015.06.063>.
- [105] Salarian M, Toyserkani E. The use of nano-computed tomography (nano-CT) in non-destructive testing of metallic parts made by laser powder-bed fusion additive manufacturing. *Int J Adv Manuf Technol* 2018;98(9–12):3147–53. <https://doi.org/10.1007/s00170-018-2421-z>.
- [106] Dahmen T, Klingaa CG, Baier-Stegmaier S, Lapina A, Pedersen DB, Hattel JH. Characterization of channels made by laser powder bed fusion and binder jetting using X-ray CT and image analysis. *Addit Manuf* 2020;36:101445. <https://doi.org/10.1016/j.addma.2020.101445>.
- [107] du Plessis A, Yadroitsava I, Yadroitssev I. Effects of defects on mechanical properties in metal additive manufacturing: A review focusing on X-ray tomography insights. *Mater Des* 2020;187:108385. <https://doi.org/10.1016/j.matdes.2019.108385>.
- [108] Budiansky N, Forman J, Van Der Schijff O. The role of computed x-ray tomography in a metallurgical analysis. *Microsc Microanal* 2015;21(S3):445–6. <https://doi.org/10.1017/s1431927615003025>.
- [109] Crook C, et al. Plate-nanolattices at the theoretical limit of stiffness and strength. *Nat Commun* 2020;11(1):1–11. <https://doi.org/10.1038/s41467-020-15434-2>.
- [110] “Resolution and Size Limitations,” *UTCT - University of Texas*. <https://www.ctlab.geo.utexas.edu/about-ct/resolution-and-size-limitations/> (accessed 14, 2021).
- [111] Nikishkov Y, Kuksenko D, Makeev A. Variable zoom technique for X-Ray Computed Tomography. *NDT E Int* 2020;116:102310. <https://doi.org/10.1016/j.ndteint.2020.102310>.
- [112] Maire E, Withers PJ. Quantitative X-ray tomography. *Int Mater Rev* 2014;59(1):1–43. <https://doi.org/10.1179/1743280413Y.0000000023>.
- [113] De Chiffre L, Carmignato S, Kruth JP, Schmitt R, Weckenmann A. Industrial applications of computed tomography. *CIRP Ann - Manuf Technol* 2014;63(2):655–77. <https://doi.org/10.1016/j.cirp.2014.05.011>.
- [114] Chen C, et al. Tribological properties of Al/diamond composites produced by cold spray additive manufacturing. *Addit Manuf* 2020;36:101434. <https://doi.org/10.1016/j.addma.2020.101434>.
- [115] Ishikawa T. Accelerator-based X-ray sources: synchrotron radiation, X-ray free electron lasers and beyond. *Philos Trans R Soc A Math Phys Eng Sci* 2019;vol. 377, no. 2147, p. 20180231. doi: 10.1098/rsta.2018.0231.
- [116] “Micro- and Nano Computed Tomography,” *Fraunhofer Institute for Integrated Circuits IIS*. <https://www.iis.fraunhofer.de/en/ff/zfp/tech/hochaufloesende-computertomographie.html> (accessed Aug. 16, 2020).
- [117] “Click-CT,” *Fraunhofer Institute for Integrated Circuits IIS*. <https://www.iis.fraunhofer.de/en/ff/zfp/products/click-ct.html> (accessed Aug. 16, 2020).
- [118] “XRM-II nanoCT,” *Fraunhofer Institute for Integrated Circuits IIS*. <https://www.iis.fraunhofer.de/en/ff/zfp/products/xrm-ii-nanoct.html> (accessed Aug. 16, 2020).
- [119] “ntCT – forward thinking Nano CT,” *Fraunhofer Institute for Integrated Circuits IIS*. <https://www.iis.fraunhofer.de/en/ff/zfp/products/ntct.html> (accessed Aug. 16, 2020).
- [120] Nikishkov Y, Seon G, Makeev A. Structural analysis of composites with porosity defects based on X-ray computed tomography. *J Compos Mater* 2014;48(17):2131–44. <https://doi.org/10.1177/0021998313494917>.
- [121] “Material and damage analysis by means of computed tomography - Fraunhofer WKL.” <https://www.wki.fraunhofer.de/en/departments/hofzet/material-and-damage-analysis-computed-tomography.html> (accessed 14, 2021).

- [122] Gong H, Nadimpalli VK, Rafi K, Starr T, Stucker B. Micro-CT Evaluation of Defects in Ti-6Al-4V Parts Fabricated by Metal Additive Manufacturing. *Technologies* 2019;7(2):44. <https://doi.org/10.3390/technologies7020044>.
- [123] Zuber M, et al. Augmented laminography, a correlative 3D imaging method for revealing the inner structure of compressed fossils. *Sci Rep* 2017;7(1):1–11. <https://doi.org/10.1038/srep41413>.
- [124] Reiter H. Computed laminography - an X-ray-method for image analysis of solder joints. *IEE Colloquium on Techniques for the Inspection of Bonded Structures* 1997;1997:10. <https://doi.org/10.1049/ic:19970057>.
- [125] Chen HC, Lin SC. The study of using X-ray laminography on printed-circuit board inspection. In: *Proceedings of the 35th International MATADOR 2007 Conference*; 2007. p. 219–24. https://doi.org/10.1007/978-1-84628-988-0_49.
- [126] Liu B et al., "An industrial computed laminography imaging system." Accessed: 27; 2021. [Online]. Available: www.ndt.net/app.DIR2015.
- [127] Gondrom S, Zhou J, Maisl M, Reiter H, Kröning M, Arnold W. X-ray computed laminography: An approach of computed tomography for applications with limited access. *Nucl Eng Des* 1999;190(1):141–7. [https://doi.org/10.1016/S0029-5493\(98\)00319-7](https://doi.org/10.1016/S0029-5493(98)00319-7).
- [128] Fisher SL, et al. Laminography in the lab: Imaging planar objects using a conventional X-ray CT scanner. *Meas Sci Technol* 2019;30(3):035401. <https://doi.org/10.1088/1361-6501/aafcae>.
- [129] Morgeneyer TF, Helfen L, Sinclair I, Proudhon H, Xu F, Baumbach T. Ductile crack initiation and propagation assessed via in situ synchrotron radiation-computed laminography. *Scr Mater* 2011;65(11):1010–3. <https://doi.org/10.1016/j.scriptamat.2011.09.005>.
- [130] Helfen L, Baumbach T, Cloetens P, Baruchel J. Phase-contrast and holographic computed laminography. *Appl Phys Lett* 2009;94(10):104103. <https://doi.org/10.1063/1.3089237>.
- [131] M. Costin, C. Vienne, and J. Garnier, "Combining a Computed Laminography Approach with Tomographic Analysis for a Study of Weld Joints," 2019, Accessed: 14, 2021. [Online]. Available: <http://www.ndt.net/?id=23674>.
- [132] W. Holub, U. Ha, C. Schorr, M. Maisl, P. Janello, and P. Jahnke, "Comparative Evaluation of Microscopic Computed Tomography for Macroscopic Objects," *Digit. Ind. Radiol. Comput. Tomogr.*, 2015, Accessed: 09, 2021. [Online]. Available: www.ndt.net/?id=18029.
- [133] Tse PW, Wang G. Sub-surface defects detection of by using active thermography and advanced image edge detection. *J Phys Conf Ser* 2017;842(1):012029. <https://doi.org/10.1088/1742-6596/842/1/012029>.
- [134] Usamentiaga R, Venegas P, Guerediaga J, Vega L, López I. Automatic detection of impact damage in carbon fiber composites using active thermography. *Infrared Phys Technol* 2013;58:36–46. <https://doi.org/10.1016/j.infrared.2013.01.004>.
- [135] León J, Perpiñà X, Altet J, Vellvehi M, Jordà X. Spatially and frequency-resolved monitoring of intradie capacitive coupling by heterodyne excitation infrared lock-in thermography. *Appl Phys Lett* 2013;102(5):054103. <https://doi.org/10.1063/1.4790299>.
- [136] Herráiz AH, Marugán AP, Márquez FPG. "A review on condition monitoring system for solar plants based on thermography", in *Non-Destructive Testing and Condition Monitoring Techniques for Renewable Energy Industrial Assets*. Elsevier 2020:103–18.
- [137] Deane S, et al. Application of NDT thermographic imaging of aerospace structures. *Infrared Phys Technol* 2019;97:456–66. <https://doi.org/10.1016/j.infrared.2019.02.002>.
- [138] Williams ME. Repair of deteriorated bridge substructures using carbon fiber-reinforced polymer (CFRP) composites. In: *Advanced Composites in Bridge Construction and Repair*, Elsevier Inc.; 2014. p. 265–286.
- [139] Verma D, Goh KL. "Natural fiber-reinforced polymer composites: Application in marine environments", in *Biomass, Biopolymer-Based Materials, and Bioenergy: Construction, Biomedical, and other Industrial Applications*. Elsevier 2019:51–73.
- [140] Puthiyaveetil N, Thomas KR, Unnikrishnakurup S, Myrach P, Ziegler M, Balasubramaniam K. Laser line scanning thermography for surface breaking crack detection : modeling and experimental study. *Infrared Phys Technol* 2020;104:103141. <https://doi.org/10.1016/j.infrared.2019.103141>.
- [141] Ryu SY, Kim DU, Kim JK, Choi HY, Kim GH, Chang KS. Surface-temperature measurement and submicron defect isolation for microelectronic devices using thermoreflectance microscopy. *Int J Thermophys* 2015;36(5–6):1217–25. <https://doi.org/10.1007/s10765-014-1681-6>.
- [142] D. Kendig, A. Tay, and A. Shakouri, "Thermal analysis of advanced microelectronic devices using thermoreflectance thermography," in *THERMINIC 2016 - 22nd International Workshop on Thermal Investigations of ICs and Systems*, Nov. 2016, pp. 115–120, doi: 10.1109/THERMINIC.2016.7749037.
- [143] Zhang H et al. Infrared thermography, ultrasound C-scan and microscope for non-destructive and destructive evaluation of 3D carbon fiber materials: a comparative study. In: *Thermosense: Thermal Infrared Applications XXXVII*, 2015, vol. 9485, no. 12, p. 94850X, doi: 10.1117/12.2176853.
- [144] Zhang H, et al. Pulsed micro-laser line thermography on submillimeter porosity in carbon fiber reinforced polymer composites: experimental and numerical analyses for the capability of detection. *Appl Opt* 2016;55(34):D1. <https://doi.org/10.1364/ao.55.0000d1>.
- [145] Zhang H, et al. Comparative study on submillimeter flaws in stitched T-joint carbon fiber reinforced polymer by infrared thermography, microcomputed tomography, ultrasonic c-scan and microscopic inspection. *Opt Eng* 2015;54(10):104109. <https://doi.org/10.1117/1.oe.54.10.104109>.
- [146] Zhang H, et al. An experimental and analytical study of micro-laser line thermography on micro-sized flaws in stitched carbon fiber reinforced polymer composites. *Compos Sci Technol* 2016;126:17–26. <https://doi.org/10.1016/j.compscitech.2016.02.007>.
- [147] Zhang H et al., "A comparative study of experimental and finite element analysis on submillimeter flaws by laser and ultrasonic excited thermography," 2016; vol. 9861, pp. 330–346. doi: 10.1117/12.2223209.
- [148] Yang J, Choi J, Hwang S, An YK, Sohn H. A reference-free micro defect visualization using pulse laser scanning thermography and image processing. *Meas Sci Technol Jul.* 2016;27(8):85601. <https://doi.org/10.1088/0957-0233/27/8/085601>.
- [149] Bu C, Li R, Liu T, Shen R, Wang J, Tang Q. Micro-crack defects detection of semiconductor Si-wafers based on Barker code laser infrared thermography. *Infrared Phys Technol* 2022;123:104160. <https://doi.org/10.1016/j.infrared.2022.104160>.
- [150] Ahmad J, Akula A, Mulaveesala R, Sardana HK. Barker-coded thermal wave imaging for non-destructive testing and evaluation of steel material. *IEEE Sens J* 2019;19(2):735–42. <https://doi.org/10.1109/JSEN.2018.2877726>.
- [151] Rani A, Sharma A, Mulaveesala R. Barker-coded thermal wave imaging for testing and evaluation of mild steel. *Lect Notes Mech Eng* 2022:73–82. https://doi.org/10.1007/978-981-16-9093-8_7/FIGURES/8.
- [152] Bodzenta J, Kamierczak-Balata A, Harris K. Quantitative thermal measurement by the use of scanning thermal microscope and resistive thermal probes. *J Appl Phys* 2020;127(3):31103. <https://doi.org/10.1063/1.5125062>.
- [153] Y. Zhang, W. Zhu, F. Hui, M. Lanza, T. Borca-Tasciuc, and M. Muñoz Rojo, "A Review on Principles and Applications of Scanning Thermal Microscopy (SThM)," *Adv. Funct. Mater.*, vol. 30, no. 18, p. 1900892, 2020, doi: 10.1002/adfm.201900892.
- [154] Shokrieh MM, Mohammadi ARG. "Non-destructive testing (NDT) techniques in the measurement of residual stresses in composite materials: An overview", in *Residual Stresses in Composite Materials*. Elsevier Ltd 2014:58–75.
- [155] Li Z, Deng L, Kinloch IA, Young RJ. Raman spectroscopy of carbon materials and their composites: Graphene, nanotubes and fibres. *Prog Mater Sci* 2023;135:101089. <https://doi.org/10.1016/J.PMATSCI.2023.101089>.
- [156] Xu Z, et al. Application of Raman spectroscopy characterization in micro/nano-machining. *Micromachines* 2018;9(7):361. <https://doi.org/10.3390/mi9070361>.
- [157] Kuball M, Pomeroy JW. A review of raman thermography for electronic and opto-electronic device measurement with submicron spatial and nanosecond temporal resolution. *IEEE Trans Device Mater Reliab* Dec. 2016;16(4):667–84. <https://doi.org/10.1109/TDMR.2016.2617458>.
- [158] Pizani PS, Jasinevicius R, Duduch JG, Porto AJV. Ductile and brittle modes in single-point-diamond-turning of silicon probed by Raman scattering. *J Mater Sci Lett* 1999;18:1185–7.
- [159] Souidi A, Dawson RD, Gu Y. Quantitative heat dissipation characteristics in current-carrying GaN nanowires probed by combining scanning thermal microscopy and spatially resolved Raman spectroscopy. *ACS Nano* 2011;5(1):255–62. <https://doi.org/10.1021/nn102818s>.
- [160] Chatterjee K, Roy D, Tuli S. A novel pulse compression algorithm for frequency modulated active thermography using band-pass filter. *Infrared Phys Technol* 2017;82:75–84. <https://doi.org/10.1016/j.infrared.2017.02.015>.
- [161] Hedayatrasa S, Poelman G, Segers J, Van Paepegem W, Kersemans M. On the application of an optimized Frequency-Phase Modulated waveform for enhanced infrared thermal wave radar imaging of composites. *Opt Lasers Eng* 2021;138:106411. <https://doi.org/10.1016/J.OPTLASENG.2020.106411>.

- [162] Ghali VS, Mulaveesala R, Takei M. Frequency-modulated thermal wave imaging for non-destructive testing of carbon fiber-reinforced plastic materials. *Meas Sci Technol* 2011;22(10):104018. <https://doi.org/10.1088/0957-0233/22/10/104018>.
- [163] Gong J, Liu J, Qin L, Wang Y. Investigation of carbon fiber reinforced polymer (CFRP) sheet with subsurface defects inspection using thermal-wave radar imaging (TWRI) based on the multi-transform technique. *NDT E Int* 2014;62:130–6. <https://doi.org/10.1016/J.NDTEINT.2013.12.006>.
- [164] Arora V, Mulaveesala R, Kumar S, Wuriti S. Non-destructive evaluation of carbon fiber reinforced polymer using Golay coded thermal wave imaging. *Infrared Phys Technol Nov.* 2021;118:103908. <https://doi.org/10.1016/J.INFARED.2021.103908>.
- [165] Arora V, Mulaveesala R. Application of golay complementary coded excitation schemes for non-destructive testing of sandwich structures. *Opt Lasers Eng* 2017;93:36–9. <https://doi.org/10.1016/J.OPTLASENG.2017.01.009>.
- [166] Mulaveesala R, Arora V, Rani A. Coded thermal wave imaging technique for infrared non-destructive testing and evaluation. *Nondestruct Test Eval Jul.* 2019; 34(3):243–53. <https://doi.org/10.1080/10589759.2019.1597356>.
- [167] R. Mulaveesala and V. Arora, "Complementary coded thermal wave imaging scheme for thermal non-destructive testing and evaluation," <http://dx.doi.org/10.1080/17686733.2016.1229329>, vol. 14, no. 1, pp. 44–53, 2016, doi: 10.1080/17686733.2016.1229329.
- [168] R. Mulaveesala, A. Muniyappa, J. A. Siddiqui, and V. Arora, "Numerical approach to binary complementary Golay coded infrared thermal wave imaging," in *Thermosense: Thermal Infrared Applications XXXVI*, 2014, vol. 9105, p. 91050T, doi: 10.1117/12.2054271.
- [169] Federici JF, Gary D, Barat R, Michalopoulos ZH. "Detection of explosives by terahertz imaging", in *Counterterrorist Detection Techniques of Explosives*. Elsevier 2007:323–66.
- [170] T. Yasui, "Terahertz frequency metrology based on frequency comb techniques," in *Handbook of Terahertz Technology for Imaging, Sensing and Communications*, Elsevier Inc., 2013, pp. 436–463.
- [171] Dhillon SS, et al. The 2017 terahertz science and technology roadmap. *J Phys D Appl Phys* 2017;50(4):43001. <https://doi.org/10.1088/1361-6463/50/4/043001>.
- [172] Wietzke S, Jördens C, Krumbholz N, Baudrit B, Bastian M, Koch M. Terahertz imaging: A new non-destructive technique for the quality control of plastic weld joints. *J Eur Opt Soc* 2007;2:7013. <https://doi.org/10.2971/jeos.2007.07013>.
- [173] O. A. Smolyanskaya et al., "Terahertz biophotonics as a tool for studies of dielectric and spectral properties of biological tissues and liquids," *Progress in Quantum Electronics*, vol. 62. Elsevier Ltd, pp. 1–77, Nov. 01, 2018, doi: 10.1016/j.pquantelec.2018.10.001.
- [174] Tao YH, Fitzgerald AJ, Wallace VP. Non-Contact, Non-Destructive Testing in Various Industrial Sectors with Terahertz Technology. *Sensors* 2020;20(3):712. <https://doi.org/10.3390/s20030712>.
- [175] Krügener K, et al. Terahertz Inspection of Buildings and Architectural Art. *Appl Sci Jul.* 2020;10(15):5166. <https://doi.org/10.3390/app10155166>.
- [176] Karpowicz N, Zhong H, Xu J, Lin KI, Hwang JS, Zhang XC. Comparison between pulsed terahertz time-domain imaging and continuous wave terahertz imaging. *Semicond Sci Technol Jul.* 2005;20(7):S293. <https://doi.org/10.1088/0268-1242/20/7/021>.
- [177] Zhu YK, Tian GY, Lu RS, Zhang H. A review of optical NDT technologies. *Sensors* 2011;11(8):7773–98. <https://doi.org/10.3390/s110807773>.
- [178] Costa FB, Machado MA, Vieira P, Santos TG. Continuous wave terahertz imaging for NDT: Fundamentals and experimental validation. *Measurement Dec.* 2020; 172:108904. <https://doi.org/10.1016/j.measurement.2020.108904>.
- [179] M. Georges, C. Thizy, J.-F. Languy, J.-F. Vandenberg, M. P. Georges, and "An, "An overview of interferometric metrology and NDT techniques and applications for the aerospace industry," in *Proc. SPIE 9960, Interferometry XVIII*, Aug. 2016, vol. 9960, pp. 40–51, doi: 10.1117/12.2240676.
- [180] Jin G, Bao NK, Chung PS. Application of nondestructive testing methods to electronic industry using computer-aided optical metrology. *Opt Lasers Eng Aug.* 1996;25(2-3):81–91. [https://doi.org/10.1016/0143-8166\(95\)00056-9](https://doi.org/10.1016/0143-8166(95)00056-9).
- [181] G. Guelker, "Mapping of plaster detachments in historical murals by electronic speckle pattern interferometry (ESPI)," in *16th Congress of the International Commission for Optics: Optics as a Key to High Technology*, Jul. 1993, vol. 1983, no. 23, pp. 935–936, doi: 10.1117/12.2308808.
- [182] Raman RKS, Bayles R. Detection of decohesion/failure of paint/coating using electronic speckle pattern interferometry. *Eng Fail Anal Oct.* 2006;13(7):1051–6. <https://doi.org/10.1016/J.ENGFAILANAL.2005.07.013>.
- [183] Francis D. "Non-destructive evaluation (NDE) of composites: Introduction to shearography", in *Non-Destructive Evaluation (NDE) of Polymer Matrix Composites. Techniques and Applications*, Woodhead Publishing 2013:56–83.
- [184] V. Petrov et al., "Advances in Digital Holographic Interferometry," *J. Imaging*, vol. 8, no. 7, Jul. 2022, doi: 10.3390/JIMAGING8070196.
- [185] Ambu R, Aymerich F, Ginesu F, Priolo P. Assessment of NDT interferometric techniques for impact damage detection in composite laminates. *Compos Sci Technol Feb.* 2006;66(2):199–205. <https://doi.org/10.1016/J.COMPOSITECH.2005.04.027>.
- [186] Thomas BP. High-speed time average digital holography for ndt of curved sandwich structures; 2011.
- [187] B. Samuel, P. Radhakrishnan, V. P. N Nampoore, and A. Mujeeb, "Application of digital holography for NDE of metallic tubes using thermal loading," 2015, Accessed: Dec. 04, 2022. [Online]. Available: <http://www.ndt.net/?id=21089>.
- [188] A. Rajendran et al., "Three dimensional digital holographic profiling of micro-fibers," *Opt. Express*, Vol. 17, Issue 4, pp. 2938–2943, vol. 17, no. 4, pp. 2938–2943, 2009, doi: 10.1364/OE.17.002938.
- [189] Seo KB, Kim BM, Kim ES. Digital holographic microscopy based on a modified lateral shearing interferometer for three-dimensional visual inspection of nanoscale defects on transparent objects. *Nanoscale Res Lett* 2014;9(1):471. <https://doi.org/10.1186/1556-276X-9-471>.
- [190] D. Findeis and J. Gryzagoridis, "A comparison of the capabilities of portable shearography and portable electronic speckle pattern interferometry," <https://doi.org/10.1117/12.539731>, vol. 5393, pp. 41–49, Jul. 2004, doi: 10.1117/12.539731.
- [191] N.-J. Choi, S. J. Kim, and Y. J. Kang, "Optical-fiber Electronic Speckle Pattern Interferometry for Quantitative Measurement of Defects on Aluminum Liners in Composite Pressure Vessels," *J. Opt. Soc. Korea*, Vol. 17, Issue 1, pp. 50–56, vol. 17, no. 1, pp. 50–56, 2013, doi: 10.3807/JOSK.2013.17.1.050.
- [192] E. A. Zarate, E. Custodio G., C. G. Treviño-Palacios, R. Rodríguez-Vera, and H. J. Puga-Soberanes, "Defect detection in metals using electronic speckle pattern interferometry," *Sol. Energy Mater. Sol. Cells*, vol. 88, no. 2, pp. 217–225, Jul. 2005, doi: 10.1016/J.SOLMAT.2004.03.009.
- [193] C.-C. Yin, T.-K. Wen Ching-Chung Yin, and T.-K. Wen, "ESPI solution for defect detection in crystalline photovoltaic cells," <https://doi.org/10.1117/12.905261>, vol. 8321, pp. 832–837, Nov. 2011, doi: 10.1117/12.905261.
- [194] Venkataraman B, Raj B, Segebade C. "NDT of Art Objects", in *Encyclopedia of Materials. Sci Technol*, Elsevier 2001:5974–7.
- [195] Peng Y, Liu G, Quan Y, Zeng Q. The depth measurement of internal defect based on laser speckle shearing interference. *Opt Laser Technol Jul.* 2017;92:69–73. <https://doi.org/10.1016/J.OPTLASENG.2017.01.004>.
- [196] Yuanpeng Z, Huaning Z, Wenling Z, Hefei L. Application of the Fourier transform in electronic speckle photography. *Exp Mech* 2002;42(1):18–24. <https://doi.org/10.1007/BF02411047>.
- [197] T.-K. Wen, C.-C. Yin Tzu-Kuei Wen, and C.-C. Yin, "Crack detection in photovoltaic cells using electronic speckle pattern interferometry," <https://doi.org/10.1117/12.851695>, vol. 7522, no. 14, pp. 1345–1349, 2010, doi: 10.1117/12.851695.
- [198] Y. Arai, "Microshape Measurement Method Using Speckle Interferometry Based on Phase Analysis," *Photonics 2021*, Vol. 8, Page 112, vol. 8, no. 4, p. 112, 2021, doi: 10.3390/PHOTONICS8040112.
- [199] Zhang L, et al. In-situ real-time imaging of subsurface damage evolution in carbon fiber composites with shearography. *Compos Commun* 2022;32:101170. <https://doi.org/10.1016/J.COCCO.2022.101170>.
- [200] M. T. Nejad, D. Akbari, and H. Tirband, "Detection of Sub-Surface Defects in Polymer Materials Using Digital Shearography Method with Different Loading and Set-up Parameters," 2020, Accessed: Nov. 30, 2022. [Online]. Available: <http://www.ndt.net/?id=26019>.
- [201] P. Huke, J. Burke, R. Bergmann, and R. B. Bergmann, "A comparative study between deflectometry and shearography for detection of subsurface defects," <https://doi.org/10.1117/12.2063650>, vol. 9203, pp. 86–97, Aug. 2014, doi: 10.1117/12.2063650.
- [202] Staub Felipe D, et al. Procedure for detecting the shape and size of defects on metallic substrates under composite repairs using shearography. *Appl Opt* 2020; 59(27):8089. <https://doi.org/10.1364/AO.399417>.
- [203] Liu Z, Gao J, Xie H, Wallace P. NDT capability of digital shearography for different materials. *Opt Lasers Eng Dec.* 2011;49(12):1462–9. <https://doi.org/10.1016/J.OPTLASENG.2011.04.006>.

- [204] Tao N, Anisimov AG, Groves RM. Shearography non-destructive testing of thick GFRP laminates: Numerical and experimental study on defect detection with thermal loading. *Compos Struct* 2022;282:115008. <https://doi.org/10.1016/J.COMPSTRUCT.2021.115008>.
- [205] Q. Zhao, X. Dan, F. Sun, Y. Wang, S. Wu, and L. Yang, "Digital Shearography for NDT: Phase Measurement Technique and Recent Developments," *Appl. Sci* 2018, Vol. 8, Page 2662, vol. 8, no. 12, p. 2662, Dec. 2018, doi: 10.3390/APP8122662.
- [206] Non-destructive testing: A guidebook for industrial management and quality control personnel. Vienna; 1999.
- [207] Honarvar F, Varvani-Farahani A. A review of ultrasonic testing applications in additive manufacturing: Defect evaluation, material characterization, and process control. *Ultrasonics* Dec. 2020;108:106227. <https://doi.org/10.1016/j.ultras.2020.106227>.
- [208] Song Y, Zi X, Fu Y, Li X, Chen C, Zhou K. Nondestructive testing of additively manufactured material based on ultrasonic scattering measurement. *Meas J Int Meas Conf* 2018;118:105–12. <https://doi.org/10.1016/j.measurement.2018.01.020>.
- [209] Sohn H, Liu P. Non-contact laser ultrasonics for SHM in aerospace structures. In: *Structural Health Monitoring (SHM) in Aerospace Structures*. Elsevier Inc.; 2016. p. 325–52.
- [210] Martín Ó, Pereda M, Santos JJ, Galán JM. Assessment of resistance spot welding quality based on ultrasonic testing and tree-based techniques. *J Mater Process Technol* Nov. 2014;214(11):2478–87. <https://doi.org/10.1016/j.jmatprotec.2014.05.021>.
- [211] Eivani AR, Vafaenezhad H, Jafarian HR, Zhou J. A novel approach to determine residual stress field during FSW of AZ91 Mg alloy using combined smoothed particle hydrodynamics/neuro-fuzzy computations and ultrasonic testing. *J Magnes Alloy* 2021. <https://doi.org/10.1016/j.jma.2020.11.018>.
- [212] McDicken WN, Anderson T. Basic physics of medical ultrasound. In: *Clinical Ultrasound*, vol. 1. Elsevier Ltd; 2011. p. 3–15.
- [213] Filippucci E, Salaffi F, Carotti M, Grassi W. Doppler ultrasound imaging techniques for assessment of synovial inflammation. *Reports Med Imaging* 2013;6(1): 83. <https://doi.org/10.2147/RM.S32950>.
- [214] Hübschen G. Ultrasonic techniques for materials characterization. In: *Materials Characterization Using Nondestructive Evaluation (NDE) Methods*. Woodhead Publishing; 2016. p. 177–224.
- [215] Lakestani F, Coste JF, Denis R. Application of ultrasonic Rayleigh waves to thickness measurement of metallic coatings. *NDT E Int* 1995;28(3):171–8. [https://doi.org/10.1016/0963-8695\(95\)00010-U](https://doi.org/10.1016/0963-8695(95)00010-U).
- [216] Y. Fang, L. Lin, H. Feng, Z. Lu, and G. W. Emms, "Review of the use of air-coupled ultrasonic technologies for nondestructive testing of wood and wood products," *Computers and Electronics in Agriculture*, vol. 137. Elsevier B.V., pp. 79–87, 2017, doi: 10.1016/j.compag.2017.03.015.
- [217] Cochran S. "Piezoelectricity and basic configurations for piezoelectric ultrasonic transducers", in *Ultrasonic Transducers: Materials and Design for Sensors. Actuators and Medical Applications*: Woodhead Publishing; 2012. p. 3–35.
- [218] Hübschen G. "Electromagnetic acoustic transducers", in *Ultrasonic Transducers: Materials and Design for Sensors. Actuators and Medical Applications*: Woodhead Publishing; 2012. p. 36–69.
- [219] Hashimoto K. "Surface acoustic wave (SAW) devices", in *Ultrasonic Transducers: Materials and Design for Sensors. Actuators and Medical Applications*: Woodhead Publishing; 2012. p. 331–73.
- [220] L. Amoroso, S. N. Ramadas, C. Klieber, T. E. Gomez Alvarez-Arenas, and T. McNally, "Novel Nanocomposite Materials for Improving Passive Layers in Air-coupled Ultrasonic Transducer Applications," in *IEEE International Ultrasonics Symposium, IUS*, Oct. 2019, vol. 2019-October, pp. 2608–2611, doi: 10.1109/ULTSYM.2019.8925712.
- [221] K. Chen, X. Fu, D. J. Dorantes-Gonzalez, Y. Li, S. Wu, and X. Hu, "Laser-generated surface acoustic wave technique for crack monitoring - A review," *International Journal of Automation Technology*, vol. 7, no. 2. Fuji Technology Press, pp. 211–220, 2013, doi: 10.20965/ijat.2013.p0211.
- [222] Kim C, Yin H, Shmatok A, Prorok BC, Lou X, Matlack KH. Ultrasonic nondestructive evaluation of laser powder bed fusion 316L stainless steel. *Addit Manuf* 2021;38:101800. <https://doi.org/10.1016/j.addma.2020.101800>.
- [223] Le Nevé C, et al. High Temperature Hydrogen Attack: New NDE Advanced Capabilities — Development and Feedback. *Am Soc Mech Eng Press Vessel Pip Div PVP* Nov. 2019;7. <https://doi.org/10.1115/PVP2019-94001>.
- [224] Korkh YV, Burkhanov AM, Rinkevich AB. Scanning acoustic microscope for visualization of microflaws in solids. *Russ J Nondestruct Test* Oct. 2009;45(10): 677–84. <https://doi.org/10.1134/S1061830909100027>.
- [225] M. Y. Mehr et al., "An overview of scanning acoustic microscope, a reliable method for non-destructive failure analysis of microelectronic components," 2015, doi: 10.1109/EuroSimE.2015.7103077.
- [226] Khuri-Yakub BT. Scanning acoustic microscopy. *Ultrasonics* 1993;31(5):361–72. [https://doi.org/10.1016/0041-624X\(93\)90070-G](https://doi.org/10.1016/0041-624X(93)90070-G).
- [227] Bertocci F, Grandoni A, Djuric-Rissner T. Scanning Acoustic Microscopy (SAM): A Robust Method for Defect Detection during the Manufacturing Process of Ultrasonic Probes for Medical Imaging. *Sensors* Nov. 2019;19(22):4868. <https://doi.org/10.3390/s19224868>.
- [228] H. Yu, "Scanning acoustic microscopy for material evaluation," *Appl. Microsc.* 2020 501, vol. 50, no. 1, pp. 1–11, Nov. 2020, doi: 10.1186/S42649-020-00045-4.
- [229] Zhang Y, et al. Sparse Reconstruction for Micro Defect Detection in Acoustic Micro Imaging. *Sensors (Basel)* Oct. 2016;16(10). <https://doi.org/10.3390/S16101773>.
- [230] Su L, Yu X, Li K, Gu J, Pecht M. Sparse Reconstruction for Microdefect Detection of Two-Dimensional Ultrasound Image Based on Blind Estimation. *IEEE Trans Ind Electron* Oct. 2021;68(10):10154–61. <https://doi.org/10.1109/TIE.2020.3021651>.
- [231] Park J, Lee J, Jeong SG, Cho Y. A study on guided wave propagation in a long distance curved pipe. *J Mech Sci Technol* 2019;33(9):4111–7. <https://doi.org/10.1007/s12206-019-0806-z>.
- [232] Yin S, Xiao H, Xu C, Wang J, Deng M, Kundu T. Microcrack localization using nonlinear Lamb waves and cross-shaped sensor clusters. *Ultrasonics* Aug. 2022; 124:106770. <https://doi.org/10.1016/J.ULTRAS.2022.106770>.
- [233] Lee YC, Cheng SW. Measuring lamb wave dispersion curves of a bi-layered plate and its application on material characterization of coating. *IEEE Trans Ultrason Ferroelectr Freq Control* 2001;48(3):830–7. <https://doi.org/10.1109/58.920717>.
- [234] D. Cirtautas, V. Samaitis, L. Maziška, R. Raišutis, and E. Zukauskas, "Selection of Higher Order Lamb Wave Mode for Assessment of Pipeline Corrosion," *Met.* 2022, Vol. 12, Page 503, vol. 12, no. 3, p. 503, 2022, doi: 10.3390/MET12030503.
- [235] Mirkhani K, et al. Optimal design of EMAT transmitters. *NDT E Int* 2004;37(3):181–93. <https://doi.org/10.1016/j.ndteint.2003.09.005>.
- [236] Tkocz J, Dixon S. Electromagnetic acoustic transducer optimisation for surface wave applications. *NDT E Int* Oct. 2019;107:102142. <https://doi.org/10.1016/j.ndteint.2019.102142>.
- [237] Liu S, Chai K, Zhang C, Jin L, Yang Q. Electromagnetic acoustic detection of steel plate defects based on high-energy pulse excitation. *Appl Sci* Aug. 2020;10(16). <https://doi.org/10.3390/app10165534>.
- [238] Park J, Lee J, Min J, Cho Y. Defects Inspection in Wires by Nonlinear Ultrasonic-Guided Wave Generated by Electromagnetic Sensors. *Appl Sci* Jun. 2020;10(13):4479. <https://doi.org/10.3390/app10134479>.
- [239] Isla J, Cegla F. EMAT phased array: A feasibility study of surface crack detection. *Ultrasonics* Jul. 2017;78:1–9. <https://doi.org/10.1016/j.ultras.2017.02.009>.
- [240] Isla J, Cegla F. Optimization of the bias magnetic field of shear wave EMATs. *IEEE Trans Ultrason Ferroelectr Freq Control* Aug. 2016;63(8):1148–60. <https://doi.org/10.1109/TUFFC.2016.2558467>.
- [241] Komura I, Nagai S, Kashiwaya H, Mori T, Arii M. Improved ultrasonic testing by phased array technique and its application. *Nucl Eng Des* Jul. 1985;vol. 87, no. C:185–91. [https://doi.org/10.1016/0029-5493\(85\)90107-4](https://doi.org/10.1016/0029-5493(85)90107-4).
- [242] Wang X, et al. Phased array ultrasonic testing of micro-flaws in additive manufactured titanium block. *Mater Res Express* 2020;7(1):16572. <https://doi.org/10.1088/2053-1591/ab6929>.
- [243] Y. Javadi et al., "Ultrasonic phased array inspection of wire plus arc additive manufacture (WAAM) samples using conventional and total focusing method (TFM) imaging approaches," 2018.
- [244] Li W, Cho Y. Combination of nonlinear ultrasonics and guided wave tomography for imaging the micro-defects. *Ultrasonics* 2016;65:87–95. <https://doi.org/10.1016/j.ultras.2015.10.016>.

- [245] Zhituhina JV, Perov DV, Rinkevich AB, Smorodinsky YG, Kröning M, Permikin VS. Characterisation of steels with microdefects using a laser interferometry technique. *Insight Non-Destructive Test Cond Monit* 2007;49(5):267–71. <https://doi.org/10.1784/insi.2007.49.5.267>.
- [246] Wang X, Gao L, Wang Y, Wang H. Design of a hybrid ultrasound and digital holography imaging system for detection of internal micro-defects. *Hongwai yu Jiguang Gongcheng/Infrared Laser Eng Jul*. 2020;49(7):20190518–20190511. <https://doi.org/10.3788/IRLA20190518>.
- [247] Karabutov AA, Podymova NB. Study on the subsurface damage depth in machined silicon wafers by the laser-ultrasonic method. *Case Stud Nondestruct Test Eval* 2014;1:7–12. <https://doi.org/10.1016/j.cnsdt.2014.03.002>.
- [248] B. Yang et al., "Laser ultrasonic imaging for defect detection on metal additive manufacturing components with rough surfaces," *Appl. Opt. Vol. 59, Issue 33, pp. 10380-10388*, vol. 59, no. 33, pp. 10380–10388, Nov. 2020, doi: 10.1364/AO.405284.
- [249] Smith RJ, Hirsch M, Patel R, Li W, Clare AT, Sharples SD. Spatially resolved acoustic spectroscopy for selective laser melting. *J Mater Process Technol Oct*. 2016;236:93–102. <https://doi.org/10.1016/J.JMATPROTEC.2016.05.005>.
- [250] Pieris D, et al. Laser Induced Phased Arrays (LIPA) to detect nested features in additively manufactured components. *Mater Des* 2020;187. <https://doi.org/10.1016/j.matdes.2019.108412>.
- [251] Guo H, Zheng B, Liu H. Numerical simulation and experimental research on interaction of micro-defects and laser ultrasonic signal. *Opt Laser Technol Nov*. 2017;96:58–64. <https://doi.org/10.1016/j.optlastec.2017.04.004>.
- [252] Manzo AJ, Helvajian H. Utility of optical heterodyne displacement sensing and laser ultrasonics as in situ process control diagnostic for additive manufacturing. *Opt Eng* 2018;57(4):041415. <https://doi.org/10.1117/1.OE.57.4.041415>.
- [253] C. Millon, A. Vanhoye, A.-F. Obaton, and J.-D. Penot, "Development of laser ultrasonics inspection for online monitoring of additive manufacturing," *Weld. World* 2018 623, vol. 62, no. 3, pp. 653–661, 2018, doi: 10.1007/S40194-018-0567-9.
- [254] N. Trimborn, "Detecting and Quantifying High Temperature Hydrogen Attack (HTHA)," 2016, Accessed: 26, 2021. [Online]. Available: <http://creativecommons.org/licenses/by-nd/3.0/>.
- [255] Umar MZ, Vavilov V, Abdullah H, Ariffin AK. Ultrasonic Infrared Thermography in Non-Destructive Testing: A Review 1. *Russ J Nondestruct Test* 2016;52(4): 31–40. <https://doi.org/10.1134/S1061830916040082>.
- [256] Han X, et al. Acoustic chaos for enhanced detectability of cracks by sonic infrared imaging. *J Appl Phys* 2004;95(7):3792–7. <https://doi.org/10.1063/1.1652243>.
- [257] D. Zhang, X. Han, and G. Newaz, "Sonic IR crack detection of aircraft turbine engine blades with multi-frequency ultrasound excitations," in *AIP Conference Proceedings*, 2014, vol. 1581 33, no. 1, pp. 1644–1651, doi: 10.1063/1.4865021.
- [258] Park H, Choi M, Park J, Kim W. A study on detection of micro-cracks in the dissimilar metal weld through ultrasound infrared thermography. *Infrared Phys Technol* 2014;62:124–31. <https://doi.org/10.1016/J.INFARED.2013.10.006>.
- [259] Favro LD, Han X, Ouyang Z, Sun G, Sui H, Thomas RL. Infrared imaging of defects heated by a sonic pulse. *Rev Sci Instrum* 2000;71(6):2418–21. <https://doi.org/10.1063/1.1150630>.
- [260] Ni P, Lee H-N. High-Resolution Ultrasound Imaging Enabled by Random Interference and Joint Image Reconstruction. *Sensors Nov*. 2020;20(22):6434. <https://doi.org/10.3390/s20226434>.
- [261] Uppal T. Tissue harmonic imaging. *Australas J Ultrasound Med* 2010;13(2):29–31. <https://doi.org/10.1002/j.2205-0140.2010.tb00155.x>.
- [262] Misaridis TX, et al. Potential of coded excitation in medical ultrasound imaging. *Ultrasonics* 2000;38(1):183–9. [https://doi.org/10.1016/S0041-624X\(99\)00130-4](https://doi.org/10.1016/S0041-624X(99)00130-4).
- [263] J. Song, S. Kim, H. yeol Sohn, T. kyong Song, and Y. M. Yoo, "Coded excitation for ultrasound tissue harmonic imaging," *Ultrasonics*, vol. 50, no. 6, pp. 613–619, 2010, doi: 10.1016/j.ultras.2010.01.001.
- [264] Ménigot S, Girault JM. Optimization of contrast resolution by genetic algorithm in ultrasound tissue harmonic imaging. *Ultrasonics* 2016;71:231–44. <https://doi.org/10.1016/j.ultras.2016.06.022>.
- [265] Ziegler L, O'Brien RT. Harmonic ultrasound: A review. *Vet Radiol Ultrasound* 2002;43(6):501–9. <https://doi.org/10.1111/j.1740-8261.2002.tb01040.x>.
- [266] Wang X, Yang J, Ji J, Zhang Y, Zhou S. Research on Golay-coded excitation in real-time imaging of high frequency ultrasound biomicroscopy. *Sci Rep Dec*. 2021;11(1):1848. <https://doi.org/10.1038/s41598-020-80406-x>.
- [267] Ladani L, Paul K, Stromer J. "High-Frequency Ultrasound Analysis in Both Experimental and Computation Level to Understand the Microstructural Change in Soft Tissues", in *Minerals, Metals and Materials Series: Springer International Publishing; 2019. p. 87–97*.
- [268] Lashkari B, Zhang K, Dovlo E, Mandelis A. Coded excitation waveform engineering for high frame rate synthetic aperture ultrasound imaging. *Ultrasonics* 2017;77:121–32. <https://doi.org/10.1016/j.ultras.2017.02.007>.
- [269] I. Solodov, N. Krohn, and G. Busse, "NONLINEAR ULTRASONIC NDT FOR EARLY DEFECT RECOGNITION AND IMAGING," 2010, Accessed: Dec. 07, 2022. [Online]. Available: <http://www.ndt.net/?id=9086>.
- [270] D. Lines et al., "Using Coded Excitation to maintain Signal to Noise for FMC+TFM on Attenuating Materials," in *IEEE International Ultrasonics Symposium, IUS*, Oct. 2019, vol. 2019-October, pp. 635–638, doi: 10.1109/ULTSYM.2019.8925564.
- [271] Tang J, Zhu W, Qiu X, Song A, Xiang Y, Xuan FZ. Non-contact phase coded excitation of ultrasonic Lamb wave for blind hole inspection. *Ultrasonics* 2022;119: 106606. <https://doi.org/10.1016/j.ultras.2021.106606>.
- [272] Deng D, et al. Image quality improvement of magneto-acousto-electrical tomography with Barker coded excitation. *Biomed Signal Process Control Aug*. 2022; 77:103823. <https://doi.org/10.1016/j.bspc.2022.103823>.
- [273] Sun T, et al. Three-dimensional magneto-acousto-electrical tomography (3D MAET) with single-element ultrasound transducer and coded excitation: A phantom validation study. *Neurocomputing* 2023;536:80–9. <https://doi.org/10.1016/j.neucom.2023.02.055>.
- [274] Carrasco Á, Méndez F, Leaman F, Molina Vicuña C. Short Review of the Use of Acoustic Emissions for Detection and Monitoring of Cracks. *Acoust Aust* 2021;49 (2):273–80. <https://doi.org/10.1007/S40857-021-00219-4/FIGURES/5>.
- [275] L. Calabrese and E. Proverbio, "A Review on the Applications of Acoustic Emission Technique in the Study of Stress Corrosion Cracking," *Corros. Mater. Degrad. 2021, Vol. 2, Pages 1-30*, vol. 2, no. 1, pp. 1–30, Dec. 2020, doi: 10.3390/CMD2010001.
- [276] De Rosa IM, Sarasini F. Use of PVDF as acoustic emission sensor for in situ monitoring of mechanical behaviour of glass/epoxy laminates. *Polym Test* 2010;29 (6):749–58. <https://doi.org/10.1016/J.POLYMERTESTING.2010.04.006>.
- [277] Masmoudi S, El Mahi A, Turki S. Use of piezoelectric as acoustic emission sensor for in situ monitoring of composite structures. *Compos Part B Eng Oct*. 2015; 80:307–20. <https://doi.org/10.1016/J.COMPOSITESB.2015.06.003>.
- [278] S. Yuyama, T. Kishi, and Y. Hisamatsu, "Fundamental aspects of AE monitoring on corrosion fatigue processes in austenitic stainless steel," *J. Mater. Energy Syst*. 1984 54, vol. 5, no. 4, pp. 212–221, 1984, doi: 10.1007/BF02835719.
- [279] Dong Y, Ansari F. Non-destructive testing and evaluation (NDT/NDE) of civil structures rehabilitated using fiber reinforced polymer (FRP) composites. *Serv Life Estim Ext Civ Eng Struct* 2011:193–222. <https://doi.org/10.1533/9780857090928.2.193>.
- [280] M. E. Sherine and S. L. Kumari, "Study of acoustic emission signals in continuous monitoring - A review," *Proc. IEEE Int. Conf. Circuit, Power Comput. Technol. ICCPCT 2017*, Oct. 2017, doi: 10.1109/ICPCT.2017.8074174.
- [281] Gholizadeh S, Lemana Z, Baharudin BTH. A review of the application of acoustic emission technique in engineering. *Struct Eng Mech* 2015;54(6):1075–95. <https://doi.org/10.12989/SEM.2015.54.6.1075>.
- [282] Nair A, Cai CS. Acoustic emission monitoring of bridges: Review and case studies. *Eng Struct* 2010;32(6):1704–14. <https://doi.org/10.1016/J.ENGSTRUCT.2010.02.020>.
- [283] An YK, Kim MK, Sohn H. Piezoelectric transducers for assessing and monitoring civil infrastructures. *Sens Technol Civ Infrastructures* 2014;1:86–120. <https://doi.org/10.1533/9780857099136.86>.
- [284] Tonelli D, Luchetta M, Rossi F, Migliorino P, Zonta D. Structural Health Monitoring Based on Acoustic Emissions: Validation on a Prestressed Concrete Bridge Tested to Failure. *Sensors (Basel) Dec*. 2020;20(24):1–20. <https://doi.org/10.3390/S20247272>.

- [285] Geng RS. Evaluation of Calendar Damage of Aircraft Structures Using Acoustic Emission. *Key Eng Mater Aug. 2004*;270–273:503–9. <https://doi.org/10.4028/WWW.SCIENTIFIC.NET/KEM.270-273.503>.
- [286] Ai L, Soltangharai V, Anay R, Van Tooren MJL, Ziehl P. Data-driven source localization of impact on aircraft control surfaces. *IEEE Aerosp Conf Proc 2020*. <https://doi.org/10.1109/AERO47225.2020.9172742>.
- [287] Morgan BC, Tilley R. Inspection of Power Plant Headers Utilizing Acoustic Emission Monitoring. *NDT& E Int J 1999*;32:167–75.
- [288] Lee JH, Lee MR, Kim JT, Kim JS. Analysis of Acoustic Emission Signals for Condition Monitoring of Check Valve at Nuclear Power Plants. *Key Eng Mater 2004*; vol. 270–273, no. 1:531–6. <https://doi.org/10.4028/WWW.SCIENTIFIC.NET/KEM.270-273.531>.
- [289] Runow P. The use of acoustic emission methods as aids to the structural integrity assessment of nuclear power plants. *Int J Press Vessel Pip 1985*;21(3): 157–207. [https://doi.org/10.1016/0308-0161\(85\)90001-8](https://doi.org/10.1016/0308-0161(85)90001-8).
- [290] Bourchak M, Farrow IR, Bond IP, Rowland CW, Menan F. Acoustic emission energy as a fatigue damage parameter for CFRP composites. *Int J Fatigue 2007*;29 (3):457–70. <https://doi.org/10.1016/J.IJFATIGUE.2006.05.009>.
- [291] S. Deschanel, W. Ben Rhouma, and J. Weiss, “Acoustic emission multiplets as early warnings of fatigue failure in metallic materials,” *Sci. Reports 2017 71*, vol. 7, no. 1, pp. 1–10, Oct. 2017, doi: 10.1038/s41598-017-13226-1.
- [292] Daniel IM, Luo J-J, Sifniotopoulos CG, Chun H-J. Acoustic Emission Monitoring of Fatigue Damage in Metals. *Rev Prog Quant Nondestruct Eval 1997*:451–8. https://doi.org/10.1007/978-1-4615-5947-4_60.
- [293] Mazal P, Vlasic F, Koula V. Use of acoustic emission method for identification of fatigue micro-cracks creation. *Procedia Eng 2015*;133:379–88. <https://doi.org/10.1016/j.proeng.2015.12.667>.
- [294] Bjørheim F, Siriwardane SC, Pavlou D. A review of fatigue damage detection and measurement techniques. *Int J Fatigue 2022*;154:106556. <https://doi.org/10.1016/J.IJFATIGUE.2021.106556>.
- [295] B. Y. Li and W. Zhang, “Metal corrosion monitoring with acoustic emission technique,” <https://doi.org/10.1179/1432891715Z.0000000001888>, vol. 19, pp. 873–876, Nov. 2015, doi: 10.1179/1432891715Z.0000000001888.
- [296] Nohal L, Mazal P, Vlasic F, Svobodova M. Acoustic emission response to erosion-corrosion and creep damage in pipeline systems. *Procedia Struct Integr 2019*; 23:227–32. <https://doi.org/10.1016/J.PROSTR.2020.01.091>.
- [297] Shi Z, Li J, Wang J. Effect of creep load on fatigue behavior and acoustic emission characteristics of sandstone containing pre-existing crack during fatigue loading. *Theor Appl Fract Mech 2022*;119:103296. <https://doi.org/10.1016/J.TAFMEC.2022.103296>.
- [298] H. Chen, Z. Shao, and Y. Fujii, “An Experimental Investigation on the Creep Behavior of Deep Brittle Rock Materials,” *Mater. 2022, Vol. 15, Page 1877*, vol. 15, no. 5, p. 1877, 2022, doi: 10.3390/MA15051877.
- [299] P. Lu and Y. K. Chou, “Analysis of acoustic emission signal evolution for monitoring diamond-coated tool delamination wear in machining,” *Mach. Mach.*, pp. 1–28, 2013, doi: 10.1533/9780857092199.1.
- [300] P. Louda, A. Sharko, and D. Stepanchikov, “An Acoustic Emission Method for Assessing the Degree of Degradation of Mechanical Properties and Residual Life of Metal Structures under Complex Dynamic Deformation Stresses,” *Mater. 2021, Vol. 14, Page 2090*, vol. 14, no. 9, p. 2090, 2021, doi: 10.3390/MA14092090.
- [301] N. Md Nor, “Structural health monitoring through acoustic emission,” *Eco-efficient Repair Rehabil. Concr. Infrastructures*, pp. 123–146, 2018, doi: 10.1016/B978-0-08-102181-1.00006-X.
- [302] J. Q. Huang, “Non-destructive evaluation (NDE) of composites: acoustic emission (AE),” *Non-Destructive Eval. Polym. Matrix Compos. Tech. Appl.*, pp. 12–32, 2013, doi: 10.1533/9780857093554.1.12.
- [303] J. Bohse and A. J. Brunner, “Acoustic emission in delamination investigation,” *Delamination Behav. Compos. A Vol. Woodhead Publ. Ser. Compos. Sci. Eng.*, pp. 217–277, 2008, doi: 10.1533/9781845694821.2.217.
- [304] B. Lishman, A. Marchenko, M. Shortt, and P. R. Sammonds, “Acoustic emissions as a measure of damage in ice,” 2019.
- [305] M. Stamm, H. Pfeiffer, J. Reynaert, and M. Wevers, “Using Acoustic Emission Measurements for Ice-Melting Detection,” *Appl. Sci. 2019, Vol. 9, Page 5387*, vol. 9, no. 24, p. 5387, Dec. 2019, doi: 10.3390/APP9245387.
- [306] Weiss J, Grasso JR. Acoustic Emission in Single Crystals of Ice. *J Phys Chem B Aug. 1997*;101(32):6113–7. <https://doi.org/10.1021/JP963157F>.
- [307] Keshtgar A, Modarres M. Fatigue Crack Initiation Sizing Using Acoustic Emission. *J Civ Eng Archit 2017*;11(12):Dec. <https://doi.org/10.17265/1934-7359/2017.12.006>.
- [308] S. Heverdine, “Use of acoustic emission in inspection investigations within ICI,” 1991.
- [309] N. Godin, P. Reynaud, and G. Fantozzi, “Challenges and limitations in the identification of acoustic emission signature of damage mechanisms in composites materials,” *Appl. Sci.*, vol. 8, no. 8, Jul. 2018, doi: 10.3390/APP8081267.
- [310] Ito K, Kusano M, Demura M, Watanabe M. Detection and location of microdefects during selective laser melting by wireless acoustic emission measurement. *Addit Manuf 2021*;40:101915. <https://doi.org/10.1016/J.ADDMA.2021.101915>.
- [311] L. Calabrese, M. Galeano, E. Proverbio, D. Di Pietro, and A. Donato, “Monitoring Of Hydrogen Assisted Scc On Martensitic Stainless Steel By Acoustic Emission Technique,” 2016.
- [312] Verstryngne E, Lacidogna G, Accornero F, Tomor A. A review on acoustic emission monitoring for damage detection in masonry structures. *Constr Build Mater 2021*;268:121089. <https://doi.org/10.1016/J.CONBUILDMAT.2020.121089>.
- [313] Santos TG, et al. Reliability and NDT Methods in *Advanced Structured Materials*. Springer 2020;129:265–95.
- [314] Chery MR, Sathish S, Welter J, Reibel R, Blodgett MP. Development of high resolution eddy current imaging using an electro-mechanical sensor. *AIP Conference Proceedings 2012*;1430(31):324–31. <https://doi.org/10.1063/1.4716246>.
- [315] R. Ghoni, M. Dollah, A. Sulaiman, and F. Mamat Ibrahim, “Defect Characterization Based on Eddy Current Technique: Technical Review,” *Adv. Mech. Eng.*, vol. 2014, 2014, doi: 10.1155/2014/182496.
- [316] Namkung M, Wincheski B, Padmapriya N. “NDT in the Aircraft and Space Industries”, in *Reference Module in Materials Science and Materials Engineering*. Elsevier; 2016.
- [317] Larionov VV, Lider AM, Garanin GV. Eddy current analysis for nuclear power materials. *Adv Mater Res 2015*;1085:335–9. <https://doi.org/10.4028/www.scientific.net/amr.1085.335>.
- [318] V. Demers-Carpentier et al., “Deployment of Pulsed Eddy Current as an Inspection Tool for Nuclear Power Plants,” 2018.
- [319] Anwar S. A parametric model of an eddy current electric machine for automotive braking applications. *IEEE Trans Control Syst Technol 2004*;12(3):422–7. <https://doi.org/10.1109/TCST.2004.824293>.
- [320] M. A. Machado, “Development of Non-Destructive Testing by Eddy Currents for Highly Demanding Engineering Applications,” Dec. 2018, Accessed: 27, 2021. [Online]. Available: <https://run.unl.pt/handle/10362/58443>.
- [321] Santos TG, Vilaça P, Dos Santos J, Quintino L, Rosado L. Innovative eddy current probe for micro defects. *AIP Conference Proceedings 2010*;1211(1):377–84. <https://doi.org/10.1063/1.3362418>.
- [322] Almeida G, Gonzalez J, Rosado L, Vilaça P, Santos TG. Advances in NDT and materials characterization by eddy currents. *Procedia CIRP 2013*;7:359–64. <https://doi.org/10.1016/j.procir.2013.05.061>.
- [323] Hoffmann B, Houbertz R, Hartmann U. Eddy current microscopy. *Appl Phys A Mater Sci Process 1998*;66(SUPPL. 1):409–13. <https://doi.org/10.1007/s003390051173>.
- [324] Cardoso FA, et al. Improved magnetic tunnel junctions design for the detection of superficial defects by eddy currents testing. *IEEE Trans Magn 2014*;50(11): Nov. <https://doi.org/10.1109/TMAG.2014.2326959>.
- [325] A. Tsukamoto, T. Hato, S. Adachi, Y. Oshikubo, K. Tsukada, and K. Tanabe, “Development of Eddy Current Testing System Using HTS-SQUID on a Hand Cart for Detection of Fatigue Cracks of Steel Plate Used in Expressways,” *IEEE Trans. Appl. Supercond.*, vol. 28, no. 4, 2018, doi: 10.1109/TASC.2018.2795614.
- [326] Romero-Arismendi NO, Pérez-Benítez JA, Ramírez-Pacheco E, Espina-Hernández JH. “Design method for a GMR-based eddy current sensor with optimal sensitivity”, *Sensors Actuators. A Phys Oct. 2020*;314. <https://doi.org/10.1016/j.sna.2020.112348>.

- [327] Jogschies L, et al. Recent Developments of Magnetoresistive Sensors for Industrial Applications. *Sensors* Nov. 2015;15(11):28665–89. <https://doi.org/10.3390/s151128665>.
- [328] Ehlers H, Pelkner M, Thewes R. Heterodyne Eddy Current Testing Using Magnetoresistive Sensors for Additive Manufacturing Purposes. *IEEE Sens J* 2020;20(11):5793–800. <https://doi.org/10.1109/JSEN.2020.2973547>.
- [329] Cacciola M, Megali G, Pellicano D, Morabito FC. A GMR-ECT based embedded solution for applications on PCB inspections. *Sensors Actuators, A Phys* 2011;167(1):25–33. <https://doi.org/10.1016/j.sna.2010.12.014>.
- [330] Chomsuwan K, Yamada S, Iwahara M. Improvement on defect detection performance of PCB inspection based on ECT technique with multi-SV-GMR sensor. *IEEE Trans Magn* 2007;43(6):2394–6. <https://doi.org/10.1109/TMAG.2007.893480>.
- [331] Pelkner M, Pohl R, Erthner T, Stegemann R, Kreutzbruck M, Sergeeva-Chollet N, Cardoso F, Freitas S, Freitas P, Caetano DM, Fernandes J, Piedade M, Paul J. Eddy current testing with high-spatial resolution probes using MR arrays as receiver. 7th International Symposium on NDT in Aerospace. Germany: Bremen; 2015.
- [332] Zhang N, Ye C, Peng L, Tao Y. Eddy Current Probe with Three-Phase Excitation and Integrated Array Tunnel Magnetoresistance Sensors. *IEEE Trans Ind Electron* 2021;68(6):5325–36. <https://doi.org/10.1109/TIE.2020.2989704>.
- [333] Rosado LS, Santos TG, Piedade M, Ramos PM, Vilaça P. “Advanced technique for non-destructive testing of friction stir welding of metals”, in *Measurement. Journal of the International Measurement Confederation*, Oct 2010;43(8):1021–30. <https://doi.org/10.1016/j.measurement.2010.02.006>.
- [334] Zhou C, Yang X, Luan G. Effect of oxide array on the fatigue property of friction stir welds. *Scr Mater* 2006;54(8):1515–20. <https://doi.org/10.1016/j.scriptamat.2005.12.036>.
- [335] Rosado LS, Gonzalez JC, Santos TG, Ramos PM, Piedade M. Geometric optimization of a differential planar eddy currents probe for non-destructive testing. *Sensors Actuators, A Phys* 2013;197:96–105. <https://doi.org/10.1016/j.sna.2013.04.010>.
- [336] Vilaça P, Santos TG, Rosado L, Miranda RM. Innovative concept and application of EC probe for inspection of friction stir welds. *Int J Microstruct Mater* 2014;9(3–5):314–26. <https://doi.org/10.1504/IJMMP.2014.066912>.
- [337] T. G. S. Santos, P. Vilaça, J. F. dos Santos, and L. Quintino, “A new NDT system for micro imperfections detection: Application to FSW and FSpW,” *Weld. World*, vol. 53, no. SPECIAL ISSUE, 2009.
- [338] Santos TG, Vilaça P, Quintino L, Dos Santos J, Miranda RM. Application of Eddy Current techniques to inspect friction spot welds in aluminium alloy AA2024 and a composite material. *Weld World* 2011;55(9–10):12–8. <https://doi.org/10.1007/BF03321315>.
- [339] A. Washabaugh, V. Zilberstein, D. Schlicker, and N. Goldfine, “Absolute Electrical Property Measurements Using Conformable MWM Eddy-Current Sensors for Quantitative Materials Characterization,” 2000, [Online]. Available: <https://www.ndt.net/search/docs.php3?id=838>.
- [340] Zilberstein V, Schlicker D, Walrath K, Weiss V, Goldfine N. MWM eddy current sensors for monitoring of crack initiation and growth during fatigue tests and in service. Online. Available: www.elsevier.com/locate/ijfatigue; 2001.
- [341] N. Goldfine, D. Schlicker, and A. Washabaugh, “Surface-mounted eddy-current sensors for on-line monitoring of fatigue tests and for aircraft health monitoring,” 1998.
- [342] Grundy D, Zilberstein V, Goldfine N, Green J, Stol I. MWM®-Array Inspection for Quality Control of Friction Stir Welded Extrusions. In: in *ASM 7th International Conference on Trends in Welding Research*; 2005. p. 1–6.
- [343] N. Goldfine, D. Grundy, V. Zilberstein, D. G. Kinchen, and A. McCool, “Friction Stir Weld Inspection Through Conductivity Imaging Using Shaped Field MWM-Arrays,” 2002.
- [344] Ma Q, Gao B, Tian GY, Yang C, Xie L, Chen K. “High sensitivity flexible double square winding eddy current array for surface micro-defects inspection”, *Sensors Actuators, A Phys* Jul. 2020;309:111844. <https://doi.org/10.1016/j.sna.2020.111844>.
- [345] Yang Y, et al. Electromagnetic Pigging System Based on Sandwich Differential Planar Coil. *IEEE Sens J* Oct. 2022;22(19):18903–13. <https://doi.org/10.1109/JSEN.2022.3201093>.
- [346] Daura LU, Tian GY, Yi Q, Sophian A. Wireless power transfer-based eddy current non-destructive testing using a flexible printed coil array: WPT based FPC-ECT. *Philos Trans R Soc A Math Phys Eng Sci* 2020;378(2182):Oct. <https://doi.org/10.1098/rsta.2019.0579>.
- [347] Long C, Zhang N, Tao X, Tao Y, Ye C. Resolution enhanced array ECT probe for small defects inspection. *Sensors* 2023;23(4):2070. <https://doi.org/10.3390/s23042070>.
- [348] Sondhi K, et al. Flexible screen-printed coils for wireless power transfer using low-frequency magnetic fields. *J Micromechanics Microengineering* 2019;29(8):084006. <https://doi.org/10.1088/1361-6439/ab26ff>.
- [349] Marchand B, Decitre J-M, Casula O. Innovative Flexible Eddy Current Probes for the Inspection of Complex Parts [Online]. Available: Accessed: Jun 2012;05:2023. <http://www.ndt.net/?id=12722>.
- [350] Zhang N, Peng L, Tao X, Ye C. Flexible ECT probe with front-end differential setting for inspection of curved CFRP structures. *Compos Part B Eng Dec.* 2021;227:109404. <https://doi.org/10.1016/j.compositesb.2021.109404>.
- [351] Camerini C, et al. In-Line Inspection Tool with Eddy Current Instrumentation for Fatigue Crack Detection. *Sensors* Jul. 2018;18(7):2161. <https://doi.org/10.3390/s18072161>.
- [352] U. Netzelmann, G. Walle, S. Lugin, A. Ehlen, S. Bessert, and B. Valeske, “Induction thermography: principle, applications and first steps towards standardisation,” <http://dx.doi.org/10.1080/17686733.2016.1145842>, vol. 13, no. 2, pp. 170–181, Jul. 2016, doi: 10.1080/17686733.2016.1145842.
- [353] Yi Q, et al. Evaluation of debonding in CFRP-epoxy adhesive single-lap joints using eddy current pulse-compression thermography. *Compos Part B Eng Dec.* 2019;178:107461. <https://doi.org/10.1016/j.compositesb.2019.107461>.
- [354] Liu F, Zhu J, Tian GY, Ulianov C, Wang Z. Investigations for inclination angle characterization of angular defects using eddy current pulsed thermography. *Infrared Phys Technol* Aug. 2019;100:73–81. <https://doi.org/10.1016/j.infrared.2019.05.016>.
- [355] Yi Q, Tian GY, Malekmohammadi H, Laureti S, Ricci M, Gao S. Inverse reconstruction of fibre orientation in multilayer CFRP using forward FEM and eddy current pulsed thermography. *NDT E Int* 2021;122:102474. <https://doi.org/10.1016/j.ndteint.2021.102474>.
- [356] Xie J, Wu C, Gao L, Xu C, Xu Y, Chen G. Detection of internal defects in CFRP strengthened steel structures using eddy current pulsed thermography. *Constr Build Mater* 2021;282:122642. <https://doi.org/10.1016/j.conbuildmat.2021.122642>.
- [357] Tong Z, et al. An efficient electromagnetic and thermal modelling of eddy current pulsed thermography for quantitative evaluation of blade fatigue cracks in heavy-duty gas turbines. *Mech Syst Signal Process* Aug. 2020;142:106781. <https://doi.org/10.1016/j.ymssp.2020.106781>.
- [358] Xu C, Zhang W, Wu C, Xie J, Yin X, Chen G. An improved method of eddy current pulsed thermography to detect subsurface defects in glass fiber reinforced polymer composites. *Compos Struct* 2020;242:112145. <https://doi.org/10.1016/j.compstruct.2020.112145>.
- [359] Wang Z, Zhu J, Tian GY, Ciampa F. Comparative analysis of eddy current pulsed thermography and long pulse thermography for damage detection in metals and composites. *NDT E Int* Oct. 2019;107:102155. <https://doi.org/10.1016/j.ndteint.2019.102155>.
- [360] M. Genest, D. C. Dudzinski, L. Dawag, and R. K. Kersey, “Crack detection using induction thermography during high-temperature testing,” in *Thermosense: Thermal Infrared Applications XXXV*, 2013, vol. 8705, no. 22, pp. 182–187, doi: 10.1117/12.2015488.
- [361] Liang T, Ren W, Tian GY, Elradi M, Gao Y. Low energy impact damage detection in CFRP using eddy current pulsed thermography. *Compos Struct* May 2016;143:352–61. <https://doi.org/10.1016/j.compstruct.2016.02.039>.
- [362] Li H, et al. Multiphysics structured eddy current and thermography defects diagnostics system in moving mode. *IEEE Trans Ind Informatics* 2021;17(4):2566–78. <https://doi.org/10.1109/TII.2020.2997836>.
- [363] Liu Y, et al. Depth quantification of rolling contact fatigue crack using eddy current pulsed thermography in stationary and scanning modes. *NDT E Int* 2022;128:102630. <https://doi.org/10.1016/j.ndteint.2022.102630>.
- [364] Yi Q, Tian GY, Malekmohammadi H, Zhu J, Laureti S, Ricci M. New features for delamination depth evaluation in carbon fiber reinforced plastic materials using eddy current pulse-compression thermography. *NDT E Int* 2019;102:264–73. <https://doi.org/10.1016/j.ndteint.2018.12.010>.
- [365] Wang H, Huang J, Liu L, Qin S, Fu Z. A novel pulsed eddy current criterion for non-ferromagnetic metal thickness quantifications under large liftoff. *Sensors* 2022;22(2):614. <https://doi.org/10.3390/s22020614>.

- [366] Xie J, et al. Visualization of defects in CFRP-reinforced steel structures using improved eddy current pulsed thermography. *Autom Constr* 2023;145:104643. <https://doi.org/10.1016/j.autcon.2022.104643>.
- [367] Tong Z, et al. Quantitative mapping of depth profile of fatigue cracks using eddy current pulsed thermography assisted by PCA and 2D wavelet transformation. *Mech Syst Signal Process* Aug. 2022;175:109139. <https://doi.org/10.1016/j.ymssp.2022.109139>.
- [368] Tu Y, Mei H, Liu L, Shen Z, Guo C, Wang L. Transient thermal pattern separation and detection of conductive defects in composite insulators using eddy current pulsed thermography. *NDT E Int* Jul. 2022;129:102653. <https://doi.org/10.1016/j.ndteint.2022.102653>.
- [369] Hernandez J, Fouliard Q, Vo K, Raghavan S. Detection of corrosion under insulation on aerospace structures via pulsed eddy current thermography. *Aerosp Sci Technol* 2022;121:107317. <https://doi.org/10.1016/j.ast.2021.107317>.
- [370] A. Sophian, G. Tian, and M. Fan, "Pulsed Eddy Current Non-destructive Testing and Evaluation: A Review," *Chinese Journal of Mechanical Engineering (English Edition)*, vol. 30, no. 3. Chinese Mechanical Engineering Society, pp. 500–514, 01, 2017, doi: 10.1007/s10033-017-0122-4.
- [371] D. Topp and M. Smith, "Application Of The ACFM Inspection Method To Rail And Rail Vehicles," 2004.
- [372] Li W, Yuan X, Chen G, Ge J, Yin X, Li K. High sensitivity rotating alternating current field measurement for arbitrary-angle underwater cracks. *NDT E Int* 2016; 79:123–31. <https://doi.org/10.1016/j.ndteint.2016.01.003>.
- [373] Li W, Yuan X, Chen G, Yin X, Ge J. A feed-through ACFM probe with sensor array for pipe string cracks inspection. *NDT E Int* Oct. 2014;67:17–23. <https://doi.org/10.1016/j.ndteint.2014.06.006>.
- [374] Nicholson GL, Davis CL. Modelling of the response of an ACFM sensor to rail and rail wheel RCF cracks. *NDT E Int* 2012;46(1):107–14. <https://doi.org/10.1016/j.ndteint.2011.11.010>.
- [375] M. C. Lugg, "The First 20 years of the A.C. field Measurement Technique," 2012, Accessed: Nov. 15, 2022. [Online]. Available: <http://www.ndt.net/?id=12552>.
- [376] Yuan X, et al. Visual and Intelligent Identification Methods for Defects in Underwater Structure Using Alternating Current Field Measurement Technique. *IEEE Trans Ind Informatics* 2022;18(6):3853–62. <https://doi.org/10.1109/TII.2021.3117034>.
- [377] W. D. Dover, R. Collins, and D. H. Michael, "The use of AC-held measurements for crack detection and sizing in air and underwater," *Philos. Trans. R. Soc. London. Ser. A, Math. Phys. Sci.*, vol. 320, no. 1554, pp. 271–283, Nov. 1986, doi: 10.1098/RSTA.1986.0116.
- [378] Elsevier 2012:534–57.
- [379] D. J. Eisenmann, D. Enyart, C. Lo, and L. Brasche, "Review of progress in magnetic particle inspection," in *AIP Conference Proceedings*, 2014, vol. 1581 33, no. 1, pp. 1505–1510, doi: 10.1063/1.4865001.
- [380] Vasylenko IV, Kazakevych ML, Pavlishchuk VV. Design of Ferrofluids and luminescent ferrofluids derived from CoFe₂O₄ nanoparticles for nondestructive defect monitoring. *Theor Exp Chem* 2019;54(6):365–8. <https://doi.org/10.1007/s11237-019-09582-w>.
- [381] Liu B, Cao Y, Zhang H, Lin YR, Sun WR, Xu B. Weak magnetic flux leakage: A possible method for studying pipeline defects located either inside or outside the structures. *NDT E Int* Jul. 2015;74:81–6. <https://doi.org/10.1016/j.ndteint.2015.05.008>.
- [382] Li E, Kang Y, Tang J, Wu J. A New Micro Magnetic Bridge Probe in Magnetic Flux Leakage for Detecting Micro-cracks. *J Nondestruct Eval* 2018;37(3):1–9. <https://doi.org/10.1007/s10921-018-0499-8/FIGURES/13>.
- [383] H. Q. Pham et al., "Highly Sensitive Planar Hall Magnetoresistive Sensor for Magnetic Flux Leakage Pipeline Inspection," *IEEE Trans. Magn.*, vol. 54, no. 6, 2018, doi: 10.1109/TMAG.2018.2816075.
- [384] Gao Y, Tian GY, Li K, Ji J, Wang P, Wang H. Multiple cracks detection and visualization using magnetic flux leakage and eddy current pulsed thermography. *Sensors Actuators A Phys* Oct. 2015;234:269–81. <https://doi.org/10.1016/j.SNA.2015.09.011>.
- [385] Ru G, Gao B, Liu D, Ma Q, Li H, Woo WL. Structural Coupled Electromagnetic Sensing of Defects Diagnostic System. *IEEE Trans Ind Electron* 2023;70(1): 951–64. <https://doi.org/10.1109/TIE.2022.3148755>.
- [386] S. Hosseingholizadeh, T. Filleter, and A. N. Sinclair, "Enhancement of Defect Characterization with AC Magnetic Flux Leakage: Far-Side Defect Shape Estimation and Sensor Lift-Off Compensation," *IEEE Trans. Magn.*, vol. 58, no. 5, 2022, doi: 10.1109/TMAG.2022.3157794.
- [387] Desvauts S, Duquennoy M, Gualandri J, Ourak M. The evaluation of surface residual stress in aeronautic bearings using the Barkhausen noise effect. *NDT E Int* 2004;37(1):9–17. [https://doi.org/10.1016/S0963-8695\(03\)00046-X](https://doi.org/10.1016/S0963-8695(03)00046-X).
- [388] Gauthier J, Krause TW, Atherton DL. Measurement of residual stress in steel using the magnetic Barkhausen noise technique. *NDT E Int* 1998;31(1):23–31. [https://doi.org/10.1016/S0963-8695\(97\)00023-6](https://doi.org/10.1016/S0963-8695(97)00023-6).
- [389] N. Prabhu Gaunkar, D. C. Jiles, and G. V. Prabhu Gaunkar, "Detection of surface cracks in ferromagnetic materials by C-scan mapping of residual stresses using Barkhausen emissions," *AIP Adv.*, vol. 10, no. 1, p. 015246, 2020, doi: 10.1063/1.5130609.
- [390] Santa-aho S, Laitinen A, Sorsa A, Vippola M. Barkhausen Noise Probes and Modelling: A Review. *J Nondestruct Eval* Dec. 2019;38(4):94. <https://doi.org/10.1007/s10921-019-0636-z>.
- [391] Olabi AG, Lorza RL, Benyounis KY. "Quality Control in Welding Process", in *Comprehensive Materials Processing* 2014;vol. 6:193–212.
- [392] Neslusan M, et al. Microstructural transformation of a rail surface induced by severe thermoplastic deformation and its non-destructive monitoring via Barkhausen noise. *Wear* 2018;402–403:38–48. <https://doi.org/10.1016/j.wear.2018.01.014>.
- [393] Takács N, Posgay G, Harasztosi L, Beke DL. Correlation between Barkhausen-noise and corrugation of railway rails. *J Mater Sci* 2002;37(17):3599–601. <https://doi.org/10.1023/A:1016592704808>.
- [394] Liu J, Tian GY, Gao B, Zeng K, Zheng Y, Chen J. Micro-macro characteristics between domain wall motion and magnetic Barkhausen noise under tensile stress. *J Magn Magn Mater* 2020;493:165719. <https://doi.org/10.1016/j.jmmm.2019.165719>.
- [395] Wang ZD, Yao K, Deng B, Ding KQ. Quantitative study of metal magnetic memory signal versus local stress concentration. *NDT E Int* 2010;43(6):513–8. <https://doi.org/10.1016/j.ndteint.2010.05.007>.
- [396] Zhao B, Yao K, Wu L, Li X, Wang Y-S. Application of Metal Magnetic Memory Testing Technology to the Detection of Stress Corrosion Defect. *Appl Sci Oct* 2020;10(20):7083. <https://doi.org/10.3390/app10207083>.
- [397] S. Bao, M. Fu, S. Hu, Y. Gu, and H. Lou, "A Review of the Metal Magnetic Memory Technique," 2016, doi: 10.1115/omae2016-54269.
- [398] Jiles DC. Review of magnetic methods for nondestructive evaluation (Part 2). *NDT Int* 1990;23(2):83–92. [https://doi.org/10.1016/0308-9126\(90\)91892-W](https://doi.org/10.1016/0308-9126(90)91892-W).
- [399] Xu K, Yang K, Liu J, Wang Y. Study on metal magnetic memory signal of buried defect in fracture process. *J Magn Magn Mater* 2020;498. <https://doi.org/10.1016/j.jmmm.2019.166139>.
- [400] Ni C, Hua L, Wang X. Crack propagation analysis and fatigue life prediction for structural alloy steel based on metal magnetic memory testing. *J Magn Magn Mater* 2018;462:144–52. <https://doi.org/10.1016/j.jmmm.2018.05.019>.
- [401] Zhao X, Su S, Wang W, Zhang X. Metal magnetic memory inspection of Q345B steel beam in four point bending fatigue test. *J Magn Magn Mater* Nov. 2020; 514. <https://doi.org/10.1016/j.jmmm.2020.167155>.
- [402] Su S, Yang Y, Wang W, Ma X. Crack propagation characterization and statistical evaluation of fatigue life for locally corroded bridge steel based on metal magnetic memory method. *J Magn Magn Mater* Oct. 2021;536. <https://doi.org/10.1016/j.jmmm.2021.168136>.
- [403] Liu B, Zeng Z, Wang H. Study on the early fatigue damage evaluation of high strength steel by using three components of metal magnetic memory signal. *NDT E Int* 2021;117. <https://doi.org/10.1016/j.ndteint.2020.102380>.
- [404] Wang H, Dong L, Wang H, Ma G, Xu B, Zhao Y. Effect of tensile stress on metal magnetic memory signals during on-line measurement in ferromagnetic steel. *NDT E Int* 2021;117. <https://doi.org/10.1016/j.ndteint.2020.102378>.
- [405] Shi P, Su S, Chen Z. Overview of researches on the nondestructive testing method of metal magnetic memory: status and challenges. *J Nondestruct Eval* 2020; 39(2):43. <https://doi.org/10.1007/s10921-020-00688-z>.
- [406] R. Tschuncky, K. Szielasko, and I. Altpeter, "Hybrid Methods for Materials Characterization," in *Materials Characterization Using Nondestructive Evaluation (NDE) Methods*, Elsevier Inc., 2016, pp. 263–291.
- [407] G. Dobmann, I. Altpeter, B. Wolter, and R. Kern, "Industrial Applications of 3MA - Micromagnetic Multiparameter Microstructure and Stress Analysis," *undefined*, 2007.

- [449] Oger L, Malard B, Odemer G, Peguet L, Blanc C. Influence of dislocations on hydrogen diffusion and trapping in an Al-Zn-Mg aluminium alloy. *Mater Des Oct* 2019;180:107901. <https://doi.org/10.1016/J.MATDES.2019.107901>.
- [450] Nagashima T, et al. Interfacial hydrogen localization in austenite/martensite dual-phase steel visualized through optimized silver decoration and scanning Kelvin probe force microscopy. *Mater Corros* 2017;68(3):306–10. <https://doi.org/10.1002/maco.201609104>.
- [451] Krieger W, Merzlikin SV, Bashir A, Szczepaniak A, Springer H, Rohwerder M. Spatially resolved localization and characterization of trapped hydrogen in zero to three dimensional defects inside ferritic steel. *Acta Mater* 2018;144:235–44. <https://doi.org/10.1016/j.actamat.2017.10.066>.
- [452] Bueno AHS, Moreira ED, Gomes JACP. Evaluation of stress corrosion cracking and hydrogen embrittlement in an API grade steel. *Eng Fail Anal* 2014;36:423–31. <https://doi.org/10.1016/j.engfailanal.2013.11.012>.
- [453] Nagumo M, Takai K, Okuda N. Nature of hydrogen trapping sites in steels induced by plastic deformation. *J Alloys Compd* 1999;293:310–6. [https://doi.org/10.1016/S0925-8388\(99\)00322-9](https://doi.org/10.1016/S0925-8388(99)00322-9).
- [454] Ryu JH, Chun YS, Lee CS, Bhadeshia HKDH, Suh DW. Effect of deformation on hydrogen trapping and effusion in TRIP-assisted steel. *Acta Mater* 2012;60(10):4085–92. <https://doi.org/10.1016/j.actamat.2012.04.010>.
- [455] Qu W, Gu C, Zheng J, Zhao Y, Hua Z. Effect of plastic deformation at room temperature on hydrogen diffusion of S30408. *Int J Hydrogen Energy* 2019;8751–8. <https://doi.org/10.1016/j.ijhydene.2018.07.156>.
- [456] Pu SD, Turk A, Lenka S, Ooi SW. Hydrogen desorption change after deformation of a bainitic steel with unstable retained austenite. *Scr Mater* 2019;170:38–42. <https://doi.org/10.1016/j.scriptamat.2019.05.026>.
- [457] T. Depover, A. Laureys, D. P. Escobar, E. Van den Eckhout, E. Wallaert, and K. Verbeken, "Understanding the interaction between a steel microstructure and hydrogen," *Materials (Basel)*, vol. 11, no. 5, 2018, doi: 10.3390/ma11050698.
- [458] Hui W, et al. Influence of cold deformation and annealing on hydrogen embrittlement of cold hardening bainitic steel for high strength bolts. *Mater Sci Eng A* 2016;662:528–36. <https://doi.org/10.1016/j.msea.2016.03.104>.
- [459] S. Komazaki and T. Sugimoto, "Changes in hydrogen desorption profiles and materials degradation in 12%Cr rotor steel," *11th Int. Conf. Fract. 2005, ICF11*, vol. 7, pp. 5123–5128, 2005.
- [460] Pérez Escobar D, Duprez L, Verbeken K, Verhaege M. Study of the hydrogen traps in a high strength TRIP steel by thermal desorption spectroscopy. *Mater Sci Forum* 2012;706–709:2253–8. <https://doi.org/10.4028/www.scientific.net/MSF.706-709.2253>.
- [461] Wei FG, Tsuzaki K. Response of hydrogen trapping capability to microstructural change in tempered Fe-0.2C martensite. *Scr Mater* 2005;52(6):467–72. <https://doi.org/10.1016/j.scriptamat.2004.11.008>.
- [462] Steppan E, Mantzke P, Steffens BR, Rhode M, Kannengiesser T. Thermal desorption analysis for hydrogen trapping in microalloyed high-strength steels. *Weld World* 2017;61(4):637–48. <https://doi.org/10.1007/s40194-017-0451-z>.
- [463] Park YD, Maroef IS, Landau A, Olson DL. Retained Austenite as a hydrogen trap in steel welds. *Weld J (Miami, Fla)* 2002;81(2):27–35.
- [464] Liu Y, Wang M, Liu G. Hydrogen trapping in high strength martensitic steel after austenitized at different temperatures. *Int J Hydrogen Energy* 2013;38(33):14364–8. <https://doi.org/10.1016/j.ijhydene.2013.08.121>.
- [465] Lemus LF, Rodrigues JH, Santos DS, Almeida LH. Hydrogen trap on the microstructure of Cr-Mo type steels. *Defect Diffus Forum* 2009;283–286:370–5. <https://doi.org/10.4028/www.scientific.net/DDF.283-286.370>.
- [466] Honda T, Komazaki S, Sugimoto T, Kohno Y. Microstructure evaluation of high chromium ferritic steels based on hydrogen desorption profile analysis. *Adv Mater Res* 2007;15–17:684–9. <https://doi.org/10.4028/www.scientific.net/amr.15-17.684>.
- [467] Pérez Escobar D, Depover T, Wallaert E, Duprez L, Verhaege M, Verbeken K. Thermal desorption spectroscopy study of the interaction between hydrogen and different microstructural constituents in lab cast Fe-C alloys. *Corros Sci* 2012;65:199–208. <https://doi.org/10.1016/j.corsci.2012.08.017>.
- [468] Yamashita H, Komazaki SI, Sato K, Kimura K. Creep damage evaluation of heat resistant ferritic stainless steel by hydrogen thermal desorption analysis. *Tetsu-To-Hagane/Journal Iron Steel Inst Japan* 2016;102(11):630–7. <https://doi.org/10.2355/tetsutohagane.TETSU-2016-047>.
- [469] Wallaert E, Depover T, Arafin M, Verbeken K. Thermal desorption spectroscopy evaluation of the hydrogen-trapping capacity of NbC and NbN precipitates. *Metall Mater Trans A Phys Metall Mater Sci* 2014;45(5):2412–20. <https://doi.org/10.1007/s11661-013-2181-1>.
- [470] Peng Z, et al. "Effect of Submicron-Scale MnS Inclusions on Hydrogen Trapping and HIC Susceptibility of X70 Pipeline Steels", *steel Res. Int Jul.* 2018;89(7):1700566. <https://doi.org/10.1002/srin.201700566>.
- [471] Maroef I, Olson DL, Eberhart M, Edwards GR. Hydrogen trapping in ferritic steel weld metal. *Int Mater Rev* 2002;47(4):191–223. <https://doi.org/10.1179/095066002225006548>.
- [472] Depover T, Verbeken K. Thermal desorption spectroscopy study of the hydrogen trapping ability of W based precipitates in a Q&T matrix. *Int J Hydrogen Energy* 2018;43(11):5760–9. <https://doi.org/10.1016/j.ijhydene.2018.01.184>.
- [473] Turk A, San Martín D, Rivera-Díaz-del-Castillo PEJ, Galindo-Nava EI. Correlation between vanadium carbide size and hydrogen trapping in ferritic steel. *Scr Mater* 2018;152(July):112–6. <https://doi.org/10.1016/j.scriptamat.2018.04.013>.
- [474] Malitckii E, et al. Comparative study of hydrogen uptake and diffusion in ODS steels. *Fusion Eng Des* 2013;88(9–10):2607–10. <https://doi.org/10.1016/j.fusengdes.2013.04.050>.
- [475] Bouchala T, Abdelhadi B, Benoudjit A. Fast analytical modeling of eddy current non-destructive testing of magnetic material. *J Nondestruct Eval* 2013;32(3):294–9. <https://doi.org/10.1007/s10921-013-0182-z>.
- [476] Fan M, Huang P, Ye B, Hou D, Zhang G, Zhou Z. Analytical modeling for transient probe response in pulsed eddy current testing. *NDT E Int Jul.* 2009;42(5):376–83. <https://doi.org/10.1016/j.ndteint.2009.01.005>.
- [477] Sanabria SJ, Furrer R, Neuenschwander J, Niemz P, Schütz P. Analytical modeling, finite-difference simulation and experimental validation of air-coupled ultrasound beam refraction and damping through timber laminates, with application to non-destructive testing. *Ultrasonics Dec.* 2015;63:65–85. <https://doi.org/10.1016/j.ultras.2015.06.013>.
- [478] Suresh V, Abudhahir A. An Analytical Model for Prediction of Magnetic Flux Leakage from Surface Defects in Ferromagnetic Tubes. *Meas Sci Rev* 2016;16(1):8–13. <https://doi.org/10.1515/msr-2016-0002>.
- [479] N. Kareta, "Modelling of Statistical Influences of Microdefects for a Reliable Production of Casting Components," Nov. 02, 2020. <https://www.spotlightmetal.com/modelling-of-statistical-influences-of-microdefects-for-a-reliable-production-of-casting-components-a-976246/> (accessed 26, 2021).
- [480] Carvalho MS, Martins AP, Santos TG. Simulation and validation of thermography inspection for components produced by additive manufacturing. *Appl Therm Eng Aug.* 2019;159:113872. <https://doi.org/10.1016/j.applthermaleng.2019.113872>.
- [481] Machado MA, Silva MI, Martins AP, Carvalho MS, Santos TG. Double active transient thermography. *NDT E Int* 2022;125:102566. <https://doi.org/10.1016/J.NDTEINT.2021.102566>.
- [482] Imperiale A, Chatillon S, Darmon M, Leymarie N, Demaldent E. UT simulation using a fully automated 3D hybrid model: Application to planar backwall breaking defects inspection. *AIP Conf Proc* 2018;1949(1):050004. <https://doi.org/10.1063/1.5031546>.
- [483] Chouh H, Rougeron G, Chatillon S, Iehl JC, Farrugia JP, Ostromoukhov V. High performance ultrasonic field simulation on complex geometries. *AIP Conf Proc* 2016;1706(1):050002. <https://doi.org/10.1063/1.4940501>.
- [484] A.-M. Zelenyak, R. Oster, M. Mosch, P. Jahnke, and M. G. R. Sause, "Numerical Modeling of Ultrasonic Inspection in Fiber Reinforced Materials with Explicit Microstructure," 2016, Accessed: Aug. 19, 2022. [Online]. Available: <http://creativecommons.org/licenses/by/3.0/>.
- [485] W. Lord, "NUMERICAL MODELING OF ELECTROMAGNETIC NDT PHENOMENA," 1983, pp. 461–470, doi: 10.1007/978-3-662-02363-1_39.
- [486] Palanisamy R, Lord W. Finite element modeling of electromagnetic NDT phenomena. *IEEE Trans Magn* 1979;15(6):1479–81. <https://doi.org/10.1109/TMAG.1979.1060412>.
- [487] Yuan F, et al. RCF crack direction assessment in moving ferromagnetic material by DC electromagnetic NDT technique. *NDT E Int* 2023;102882. <https://doi.org/10.1016/J.NDTEINT.2023.102882>.
- [488] He X, Gu F, Ball A. A review of numerical analysis of friction stir welding. *Prog Mater Sci Aug.* 2014;65:1–66. <https://doi.org/10.1016/J.PMATSCI.2014.03.003>.

- [489] Ke W, Castaings M, Bacon C. 3D finite element simulations of an air-coupled ultrasonic NDT system. *NDT E Int* 2009;42(6):524–33. <https://doi.org/10.1016/j.ndteint.2009.03.002>.
- [490] Zhang F, Pan Y, Zhao J, Zhang X. Test, modeling, and analysis of air-coupled ultrasonic transducer based on piezoelectric film. *AIP Adv* 2020;10(6):065014. <https://doi.org/10.1063/5.0004688>.
- [491] C. Zhao, S. Tanweer, J. Li, M. Lin, X. Zhang, and Y. Liu, "Nonlinear Guided Wave Tomography for Detection and Evaluation of Early-Life Material Degradation in Plates," *Sensors* 2021, Vol. 21, Page 5498, vol. 21, no. 16, p. 5498, Aug. 2021, doi: 10.3390/S21165498.
- [492] A. P. Martins, M. S. Carvalho, J. B. Cardoso, and T. G. Santos, "Simulation of NDT methods for Additive Manufacturing of composites," 2018, Accessed: 08, 2021. [Online]. Available: <http://www.ndt.net/?id=22808>.
- [493] M. Reiter, M. Erler, C. Kuhn, C. Gusenbauer, and J. Kastner, "SimCT: a simulation tool for X-ray imaging," 2016.
- [494] Duvauchelle P, Freud N, Kaftandjian V, Babot D. Computer code to simulate X-ray imaging techniques. *Nucl Instruments Methods Phys Res Sect B Beam Interact with Mater Atoms* 2000;170(1):245–58. [https://doi.org/10.1016/S0168-583X\(00\)00185-3](https://doi.org/10.1016/S0168-583X(00)00185-3).
- [495] S. Mahaut et al., "Simulation of Complex Ultrasonic NDT Cases Using Coupled Analytical-Numerical Method: The Mohycan Project," Aug. 2010, Accessed: 26, 2021. [Online]. Available: <https://www.ndt.net/search/docs.php?id=9413>.
- [496] Dimova G, Yurukov V, Djivdjanov K. Critical defect size assessment in pipelines on a nuclear power plant. *MATEC Web Conf* 2018;145:05014. <https://doi.org/10.1051/mateconf/201814505014>.
- [497] Wei L, Guoming C, Wenyan L, Zhun L, Feng L. Analysis of the inducing frequency of a U-shaped ACFM system. *NDT E Int* 2011;44(3):324–8. <https://doi.org/10.1016/j.ndteint.2010.10.009>.
- [498] Yeom Y-T, Kim H-J, Song S-J, Tang Z, Kwon S-D, Kang S-S. A Study on Evaluation Method for Micro Defects on Surface based on Leaky Rayleigh Wave. *J Korean Phys Soc* 2019;74(5):459–64. <https://doi.org/10.3938/jkps.74.459>.
- [499] Tang QJ, Gao SS, Liu YJ, Wang YZ, Dai JM. THEORETICAL STUDY ON INFRARED THERMAL WAVE IMAGING DETECTION OF SEMICONDUCTOR SILICON WAFERS WITH MICRO-CRACK DEFECTS. *Therm Sci* 2020;vol. 24, no. 6 PART B:4011–7. <https://doi.org/10.2298/TSCI2006011T>.
- [500] Su L, Yu X, Li K, Yao X, Pecht M. Simulation and Experimental Verification of Edge Blurring Phenomenon in Microdefect Inspection Based on High-Frequency Ultrasound. *IEEE Access* 2019;7:11515–25. <https://doi.org/10.1109/ACCESS.2019.2892231>.
- [501] Yu X, Huang H, Xie W, Gu J, Li K, Su L. Simulation Research on Sparse Reconstruction for Defect Signals of Flip Chip Based on High-Frequency Ultrasound. *Appl Sci* 2020;10(4):1292. <https://doi.org/10.3390/app10041292>.
- [502] James G, Witten D, Hastie T, Tibshirani R. *An Introduction to Statistical Learning*. 7th ed. New York, NY: Springer; 2013.
- [503] Shrifan NHMM, Akbar MF, Isa NAM. Prospect of using artificial intelligence for microwave nondestructive testing technique: A review. *IEEE Access* 2019;7:110628–50. <https://doi.org/10.1109/ACCESS.2019.2934143>.
- [504] Hema Rajini N, Bhavani R. Automatic classification of computed tomography brain images using ANN, k-NN and SVM. *AI Soc* 2014;29(1):97–102. <https://doi.org/10.1007/s00146-013-0442-6>.
- [505] Kozic E, et al. Metallization defect detection in 3D integrated components using scanning acoustic microscopy and acoustic simulations. *Microelectron Reliab* 2018;88–90:262–6. <https://doi.org/10.1016/j.microrel.2018.07.075>.
- [506] Muhammad W, Brahme AP, Ibragimova O, Kang J, Inal K. A machine learning framework to predict local strain distribution and the evolution of plastic anisotropy & fracture in additively manufactured alloys. *Int J Plast* 2021;136. <https://doi.org/10.1016/j.iplas.2020.102867>.
- [507] Duan Y, et al. Automated defect classification in infrared thermography based on a neural network. *NDT E Int* Oct. 2019;107:102147. <https://doi.org/10.1016/j.ndteint.2019.102147>.
- [508] Huda ASN, Taib S, Ghazali KH, Jadin MS. A new thermographic NDT for condition monitoring of electrical components using ANN with confidence level analysis. *ISA Trans* 2014;53(3):717–24. <https://doi.org/10.1016/j.isatra.2014.02.003>.
- [509] N. Harrap, R. Rheume, and A. Gosselin, "Artificial intelligence approaches as tools for auditing and improving data analysis of advanced ultrasound techniques in non-destructive testing," 2019, doi: 10.2118/193088-ms.
- [510] Virkkunen I, Koskinen T, Jessen-Juhler O, Rinta-aho J. Augmented ultrasonic data for machine learning. *J Nondestruct Eval* 2021;40(1):4. <https://doi.org/10.1007/s10921-020-00739-5>.
- [511] Fakhri MA, Chiachio M, Chiachio J, Mustapha S. A Bayesian approach for damage assessment in welded structures using Lamb-wave surrogate models and minimal sensing. *NDT E Int* 2022;128:102626. <https://doi.org/10.1016/J.NDTEINT.2022.102626>.
- [512] AbdAlla AN, Faraj MA, Samsuri F, Rifai D, Ali K, Al-Douri Y. Challenges in improving the performance of eddy current testing: Review. *Meas Control* 2019;52(1–2):46–64. <https://doi.org/10.1177/0020294018801382>.
- [513] Rosado LS, Janeiro FM, Ramos PM, Piedade M. Defect characterization with eddy current testing using nonlinear-regression feature extraction and artificial neural networks. *IEEE Trans Instrum Meas* 2013;62(5):1207–14. <https://doi.org/10.1109/TIM.2012.2236729>.
- [514] A. Nicolai, D. Caputo, L. Chieco, F. Grimaccia, and M. Mussetta, "Machine Learning-Based Detection Technique for NDT in Industrial Manufacturing," *Math*. 2021, Vol. 9, Page 1251, vol. 9, no. 11, p. 1251, 2021, doi: 10.3390/MATH9111251.
- [515] Hu B, et al. A Lightweight Spatial and Temporal Multi-Feature Fusion Network for Defect Detection. *IEEE Trans Image Process* 2021;30:472–86. <https://doi.org/10.1109/TIP.2020.3036770>.
- [516] Song L, Li X, Yang Y, Zhu X, Guo Q, Yang H. Detection of Micro-Defects on Metal Screw Surfaces Based on Deep Convolutional Neural Networks. *Sensors* Oct. 2018;18(11):3709. <https://doi.org/10.3390/s18113709>.
- [517] Noori Hoshyar A, Rashidi M, Liyanapathirana R, Samali B. Algorithm Development for the Non-Destructive Testing of Structural Damage. *Appl Sci* Jul. 2019;9(14):2810. <https://doi.org/10.3390/app9142810>.
- [518] Tripathi G, Anowarul H, Agarwal K, Prasad DK. Classification of micro-damage in piezoelectric ceramics using machine learning of ultrasound signals. *Sensors (Switzerland)* Oct. 2019;19(19). <https://doi.org/10.3390/s19194216>.
- [519] Niu S, Li B, Wang X, Lin H. Defect Image Sample Generation with GAN for Improving Defect Recognition. *IEEE Trans Autom Sci Eng* Jul. 2020;17(3):1611–22. <https://doi.org/10.1109/TASE.2020.2967415>.
- [520] Taheri H, Bocanegra MG, Taheri M. Artificial Intelligence, Machine Learning and Smart Technologies for Nondestructive Evaluation. *Sensors* 2022;vol. 22, no. 11. MDPI, 01. <https://doi.org/10.3390/s22114055>.
- [521] Uhlig S, Alkhasli I, Schubert F, Tschöpe C, Wolff M. A review of synthetic and augmented training data for machine learning in ultrasonic non-destructive evaluation. *Ultrasonics* 2023;107041. <https://doi.org/10.1016/J.ULTRAS.2023.107041>.
- [522] Liu Y, Bao Y. Review on automated condition assessment of pipelines with machine learning. *Adv Eng Informatics* Aug. 2022;53:101687. <https://doi.org/10.1016/J.AEI.2022.101687>.
- [523] Sun H, Ramuhalli P, Jacob RE. Machine learning for ultrasonic nondestructive examination of welding defects: A systematic review. *Ultrasonics* 2023;127:106854. <https://doi.org/10.1016/J.ULTRAS.2022.106854>.
- [524] Atwya M, Panoutsos G. Transient Thermography for Friction Stir Welding: A Machine Learning Approach. *IEEE Trans Ind Informatics* Jul. 2020;16(7):4423–35. <https://doi.org/10.1109/TII.2019.2948023>.
- [525] Ryu S, Park SH, Jhang KY. Plastic properties estimation of aluminum alloys using machine learning of ultrasonic and eddy current data. *NDT E Int* Jul. 2023;137:102857. <https://doi.org/10.1109/TII.2019.2948023>.
- [526] Amiri N, Farrahi GH, Kashyzadeh KR, M. Chizari. Applications of ultrasonic testing and machine learning methods to predict the static & fatigue behavior of spot-welded joints. *J Manuf Process* 2020;52:26–34. <https://doi.org/10.1109/TII.2019.2948023>.
- [527] Ebrahimkhanlou A, Dubuc B, Salamone S. A generalizable deep learning framework for localizing and characterizing acoustic emission sources in riveted metallic panels. *Mech Syst Signal Process* 2019;130:248–72. <https://doi.org/10.1016/j.ymsp.2019.04.050>.
- [528] Shipway NJ, Huthwaite P, Lowe MJS, Barden TJ. Using ResNets to perform automated defect detection for Fluorescent Penetrant Inspection. *NDT E Int* 2021;119:102400. <https://doi.org/10.1016/j.ndteint.2020.102400>.

- [529] Le M, Pham CT, Lee J. Deep neural network for simulation of magnetic flux leakage testing. *Meas J Int Meas Confed* 2021;170:108726. <https://doi.org/10.1016/j.measurement.2020.108726>.
- [530] Ajmi C, Zapata J, Elferchichi S, Zaafour A, Laabidi K. Deep Learning Technology for Weld Defects Classification Based on Transfer Learning and Activation Features. *Adv Mater Sci Eng* 2020;2020. <https://doi.org/10.1155/2020/1574350>.
- [531] M. Hasanian, M. G. Ramezani, B. Golchinfar, and H. Saboonchi, "Automatic segmentation of ultrasonic TFM phased array images: the use of neural networks for defect recognition," in *Sensors and Smart Structures Technologies for Civil, Mechanical, and Aerospace Systems 2020*, 2020, vol. 11379, p. 13, doi: 10.1117/12.2558975.
- [532] Singh H, Ahmed AS, Melandsø F, Habib A. Ultrasonic image denoising using machine learning in point contact excitation and detection method. *Ultrasonics* 2023;127:106834. <https://doi.org/10.1016/J.ULTRAS.2022.106834>.
- [533] M. G. Ramezani, M. Hasanian, B. Golchinfar, and H. Saboonchi, "Automatic boiler tube leak detection with deep bidirectional LSTM neural networks of acoustic emission signals," in *Sensors and Smart Structures Technologies for Civil, Mechanical, and Aerospace Systems 2020*, 2020, vol. 11379, p. 56, doi: 10.1117/12.2558885.
- [534] Kopp R, Joseph J, Wardle BL. "Automated segmentation of in situ X-ray microtomography of progressive damage in advanced composites via deep learning", in *AIAA Scitech. Forum* 2021;2021:1–23. <https://doi.org/10.2514/6.2021-2024>.
- [535] Liu H, Zhang Y. Deep learning based crack damage detection technique for thin plate structures using guided lamb wave signals. *Smart Mater Struct* 2020;29(1):pp. <https://doi.org/10.1088/1361-665X/ab58d6>.
- [536] C. Kofler, C. A. Dohr, J. Dohr, and A. Zernig, "Data-Centric Model Development to Improve the CNN Classification of Defect Density SEM Images," in *IECON Proceedings (Industrial Electronics Conference)*, 2022, vol. 2022-October, doi: 10.1109/IECON49645.2022.9968911.
- [537] Siljama O, Koskinen J, Jessen-Juhler O, Virkkunen I. Automated flaw detection in multi-channel phased array ultrasonic data using machine learning. *J Nondestruct Eval* 2021;40(3):1–13. <https://doi.org/10.1007/S10921-021-00796-4/FIGURES/6>.
- [538] Z. H. Chen and J. C. Juang, "AE-RTISNet: Aeronautics Engine Radiographic Testing Inspection System Net with an Improved Fast Region-Based Convolutional Neural Network Framework," *Appl. Sci.* 2020, Vol. 10, Page 8718, vol. 10, no. 23, p. 8718, Dec. 2020, doi: 10.3390/APP10238718.
- [539] Hu Y, et al. Automatic defect detection from X-ray Scans for Aluminum Conductor Composite Core Wire Based on Classification Neutral Network. *NDT E Int* Dec. 2021;124:102549. <https://doi.org/10.1016/J.NDTEINT.2021.102549>.
- [540] Y. Cao, Y. Wang, H. Feng, and T. Wang, "Method for detecting surface defects of ceramic tile based on improved Cascade RCNN," in *2022 4th International Conference on Frontiers Technology of Information and Computer, ICFITC 2022*, 2022, pp. 41–45, doi: 10.1109/ICFITC57696.2022.10075095.
- [541] L. Lu et al., "Defect Detection of Small-size Fittings Based on Reformative Cascade RCNN Network," in *2022 2nd International Conference on Algorithms, High Performance Computing and Artificial Intelligence, AHPCAI 2022*, 2022, pp. 490–494, doi: 10.1109/AHPCAI57455.2022.10087747.
- [542] Q. Xie, W. Zhou, H. Tan, and X. Wang, "Surface Defect Recognition in Steel Plates Based on Improved Faster R-CNN," in *Chinese Control Conference, CCC*, 2022, vol. 2022-July, pp. 6759–6764, doi: 10.23919/CCC55666.2022.9901872.
- [543] Zhang K, Lv G, Guo S, Chen D, Liu Y, Feng W. Evaluation of subsurface defects in metallic structures using laser ultrasonic technique and genetic algorithm-back propagation neural network. *NDT E Int* Dec. 2020;116:102339. <https://doi.org/10.1016/j.ndteint.2020.102339>.
- [544] Mardanshahi A, Nasir V, Kazemirad S, Shokrieh MM. Detection and classification of matrix cracking in laminated composites using guided wave propagation and artificial neural networks. *Compos Struct* Aug. 2020;246. <https://doi.org/10.1016/j.compstruct.2020.112403>.
- [545] Younes D, Alghannam E, Tan Y, Lu H. Enhancement in Quality Estimation of Resistance Spot Welding Using Vision System and Fuzzy Support Vector Machine. *Symmetry (Basel)* Aug. 2020;12(8):1380. <https://doi.org/10.3390/sym12081380>.
- [546] Xie J, Xu C, Chen G, Huang W, Song G. Automated identification of front/rear surface cracks in ferromagnetic metals based on eddy current pulsed thermography. *Infrared Phys Technol* Nov. 2022;126:104345. <https://doi.org/10.1016/j.infrared.2022.104345>.
- [547] Arenas MP, et al. Novel austenitic steel ageing classification method using eddy current testing and a support vector machine. *Meas J Int Meas Confed* Oct. 2018;127:98–103. <https://doi.org/10.1016/j.measurement.2018.05.101>.
- [548] Prakash N, Nieberl D, Mayer M, Schuster A. Learning defects from aircraft NDT data. *NDT E Int* 2023;102885. <https://doi.org/10.1016/J.NDTEINT.2023.102885>.
- [549] Shrifan NHMM, Jawad GN, Isa NAM, Akbar MF. Microwave Nondestructive Testing for Defect Detection in Composites Based on K-Means Clustering Algorithm. *IEEE Access* 2021;9:4820–8. <https://doi.org/10.1109/ACCESS.2020.3048147>.
- [550] Rishah A, Tavakolian P, Melinkov A, Mandelis A. Infrared computer vision in non-destructive imaging: Sharp delineation of subsurface defect boundaries in enhanced truncated correlation photothermal coherence tomography images using K-means clustering. *NDT E Int* 2022;125:102568. <https://doi.org/10.1016/J.NDTEINT.2021.102568>.
- [551] Gao X, Tian Y, Jiao J, Gao J, Li C. An accurate measurement method of lamb wave phase velocity based on clustering algorithms. *Meas J Int Meas Confed* 2022; 195:111178. <https://doi.org/10.1016/j.measurement.2022.111178>.
- [552] Obaton AF, Wang Y, Butsch B, Huang Q. A non-destructive resonant acoustic testing and defect classification of additively manufactured lattice structures. *Weld World* 2021;1–11. <https://doi.org/10.1007/s40194-020-01034-7>.
- [553] Jiang F, Guan Z, Li Z, Wang X. A method of predicting visual detectability of low-velocity impact damage in composite structures based on logistic regression model. *Chinese J Aeronaut* 2021;34(1):296–308. <https://doi.org/10.1016/j.cja.2020.10.006>.
- [554] C. Völker, S. Kruschwitz, and G. Ebell, "A Machine Learning-Based Data Fusion Approach for Improved Corrosion Testing," *Surveys in Geophysics*, vol. 41, no. 3. Springer, pp. 531–548, 01, 2020, doi: 10.1007/s10712-019-09558-4.
- [555] P. Jo Chun, I. Ujike, K. Mishima, M. Kusumoto, and S. Okazaki, "Random forest-based evaluation technique for internal damage in reinforced concrete featuring multiple nondestructive testing results," *Constr. Build. Mater.*, vol. 253, p. 119238, Aug. 2020, doi: 10.1016/j.conbuildmat.2020.119238.
- [556] Shipway NJ, Huthwaite P, Lowe MJS, Barden TJ. Performance Based Modifications of Random Forest to Perform Automated Defect Detection for Fluorescent Penetrant Inspection. *J Nondestruct Eval* 2019;38(2):1–11. <https://doi.org/10.1007/s10921-019-0574-9>.
- [557] Sheng H, Wang P, Tang C, Shi Y, Zheng Y. Microstructure and mechanical properties evaluation of automotive plate steel based on micromagnetic NDT technologies. *Measurement* Aug. 2022;199:111459. <https://doi.org/10.1016/J.MEASUREMENT.2022.111459>.
- [558] K. Liu, Z. Ma, Y. Liu, J. Yang, and Y. Yao, "Enhanced Defect Detection in Carbon Fiber Reinforced Polymer Composites via Generative Kernel Principal Component Thermography," *Polym.* 2021, Vol. 13, Page 825, vol. 13, no. 5, p. 825, Mar. 2021, doi: 10.3390/POLYM13050825.
- [559] Oliveira MA, Simas Filho EF, Albuquerque MCS, Santos YTB, da Silva IC, Farias CTT. Ultrasound-based identification of damage in wind turbine blades using novelty detection. *Ultrasonics* Dec. 2020;108:106166. <https://doi.org/10.1016/j.ultras.2020.106166>.
- [560] A. Gupta et al., "Identifying Combination of Defects and Unknown Defects on Semiconductor Wafers using Deep Learning and Hierarchical Reclustering," in *Proceedings - 2022 35th International Conference on VLSI Design, VLSID 2022 - held concurrently with 2022 21st International Conference on Embedded Systems, ES 2022*, 2022, pp. 150–155, doi: 10.1109/VLSID2022.2022.00039.
- [561] S. Guo, Z. Liu, and Y. Tan, "Research on Weld Defect Identification Technology Based on EMD and BP Neural Network," in *Proceedings - 2022 8th Annual International Conference on Network and Information Systems for Computers, ICNISC 2022*, 2022, pp. 655–659, doi: 10.1109/ICNISC57059.2022.00134.
- [562] Li TJ, Chen CC, Liu JJ, Shao GF, Chan CCK. A Novel THz Differential Spectral Clustering Recognition Method Based on t-SNE. *Discret Dyn Nat Soc* 2020;2020. <https://doi.org/10.1155/2020/6787608>.
- [563] Kim JG, Jang C, Kang SS. Classification of ultrasonic signals of thermally aged cast austenitic stainless steel (CASS) using machine learning (ML) models. *Nucl Eng Technol* 2022;54(4):1167–74. <https://doi.org/10.1016/j.net.2021.09.033>.
- [564] M. Le, V. S. Luong, D. K. Nguyen, D. K. Le, and J. Lee, "Auto-Detection of Hidden Corrosion in an Aircraft Structure by Electromagnetic Testing: A Machine-Learning Approach," *Appl. Sci.* 2022, Vol. 12, Page 5175, vol. 12, no. 10, p. 5175, 2022, doi: 10.3390/APP12105175.
- [565] Kraljevski I, Duckhorn F, Tschöpe C, Wolff M. Machine Learning for Anomaly Assessment in Sensor Networks for NDT in Aerospace. *IEEE Sens J* 2021;21(9): 11000–8. <https://doi.org/10.1109/JSEN.2021.3062941>.

- [566] Rodríguez-Martín M, et al. Step heating thermography supported by machine learning and simulation for internal defect size measurement in additive manufacturing. *Measurement* Dec. 2022;205:112140. <https://doi.org/10.1016/J.MEASUREMENT.2022.112140>.
- [567] M. Parvez M et al., "Machine learning based models for defect detection in composites inspected by Barker coded thermography: A qualitative analysis," *Adv. Eng. Softw.*, vol. 178, p. 103425, 2023, doi: 10.1016/J.ADVENGSOFT.2023.103425.
- [568] Ju S, Li D, Jia J. Machine-learning-based methods for crack classification using acoustic emission technique. *Mech Syst Signal Process* Oct. 2022;178:109253. <https://doi.org/10.1016/J.YMSSP.2022.109253>.
- [569] Wang J, Zhou W, Ren X, Su M, Liu J. A waveform-based clustering and machine learning method for damage mode identification in CFRP laminates. *Compos Struct* 2023;312:116875. <https://doi.org/10.1016/J.COMPSTRUCT.2023.116875>.
- [570] Ben-Yelun I, Díaz-Lago M, Saucedo-Mora L, Sanz MÁ, Callado R, Montáns FJ. Self-learning locally-optimal hypertuning using maximum entropy, and comparison of machine learning approaches for estimating fatigue life in composite materials of the aerospace industry. *Eng Struct* 2023;283:115829. <https://doi.org/10.1016/J.ENGSTRUCT.2023.115829>.
- [571] Doaei M, Tavallali MS, Nejati H. Fault classification in electrofusion polyethylene joints by combined machine learning, thermal pulsing and IR thermography methods – A comparative study. *Infrared Phys Technol* 2019;96:262–6. <https://doi.org/10.1016/J.INFRARED.2018.11.032>.
- [572] Banjara NK, Sasmal S, Voggu S. Machine learning supported acoustic emission technique for leakage detection in pipelines. *Int J Press Vessel Pip* Dec. 2020; 188:104243. <https://doi.org/10.1016/J.IJPVP.2020.104243>.
- [573] Lv G, et al. Laser ultrasonics and machine learning for automatic defect detection in metallic components. *NDT E Int* 2023;133:102752. <https://doi.org/10.1016/J.NDTEINT.2022.102752>.
- [574] Hornás J, et al. Modelling fatigue life prediction of additively manufactured Ti-6Al-4V samples using machine learning approach. *Int J Fatigue* 2023;169: 107483. <https://doi.org/10.1016/J.IJFATIGUE.2022.107483>.
- [575] Parlak İE, Emel E. Deep learning-based detection of aluminum casting defects and their types. *Eng Appl Artif Intell* 2023;118:105636. <https://doi.org/10.1016/J.ENGAPPAI.2022.105636>.
- [576] Cariou V, Jouan-Rimbaud Bouveresse D, Qannari EM, Rutledge DN. ComDim Methods for the Analysis of Multiblock Data in a Data Fusion Perspective. In: *Data Handling in Science and Technology*, vol. 31. Elsevier Ltd; 2019. p. 179–204.
- [577] de Juan A, Tauler R. Data Fusion by Multivariate Curve Resolution. In: *Data Handling in Science and Technology*, vol. 31. Elsevier Ltd; 2019. p. 205–33.
- [578] dos Santos TG, Silva BS, dos Santos Vilaça P, Quintino L, Sousa JMC. Data fusion in non destructive testing using fuzzy logic to evaluate friction stir welding. *Weld Int* 2008;22(12):826–33. <https://doi.org/10.1080/09507110802591327>.
- [579] R. Cormerais, A. Duclos, G. Wasselynyck, G. Berthiau, and R. Longo, "A Data Fusion Method for Non-Destructive Testing by Means of Artificial Neural Networks," *Sensors* 2021, Vol. 21, Page 2598, vol. 21, no. 8, p. 2598, 2021, doi: 10.3390/S21082598.
- [580] Oesch T, Weise F, Bruno G. Detection and quantification of cracking in concrete aggregate through virtual data fusion of X-ray computed tomography images. *Materials (Basel)* 2020;13(18). <https://doi.org/10.3390/MA13183921>.
- [581] Yilmaz B, Ba A, Jasiuniene E, Bui H-K, Berthiau G. Evaluation of Bonding Quality with Advanced Nondestructive Testing (NDT) and Data Fusion. *Sensors* 2020; 20(18):5127. <https://doi.org/10.3390/s20185127>.
- [582] Mishra M, Bhatia AS, Maity D. A comparative study of regression, neural network and neuro-fuzzy inference system for determining the compressive strength of brick-mortar masonry by fusing nondestructive testing data. *Eng Comput* 2021;37(1):77–91. <https://doi.org/10.1007/s00366-019-00810-4>.
- [583] Gros XE, Bousigues J, Takahashi K. NDT data fusion at pixel level. *NDT&E Int* 1999;32(5):283–92. [https://doi.org/10.1016/S0963-8695\(98\)00056-5](https://doi.org/10.1016/S0963-8695(98)00056-5).
- [584] Ahadi Akhlaghi I, Salkhordeh Haghighi M, Kahrobaee S, Hojati M. Prediction of chemical composition and mechanical properties in powder metallurgical steels using multi-electromagnetic nondestructive methods and a data fusion system. *J Magn Magn Mater* 2020;498:166246. <https://doi.org/10.1016/j.jmmm.2019.166246>.
- [585] Bayat S, Jamzad A, Zobeiry N, Poursartip A, Mousavi P, Abolmaesumi P. Temporal enhanced Ultrasound: A new method for detection of porosity defects in composites. *Compos Part A Appl Sci Manuf* 2023;164:107259. <https://doi.org/10.1016/j.compositesa.2022.107259>.
- [586] Moradi M, Abolmaesumi P, Mousavi P. Tissue typing using ultrasound RF time series: Experiments with animal tissue samples. *Med Phys* 2010;37(8):4401–13. <https://doi.org/10.1118/1.3457710>.
- [587] Zobeiry N, Bayat S, Anas E, Mousavi P, Abolmaesumi P, Poursartip A. Temporal enhanced ultrasound as a Novel NDT technique for characterization of defects in composites. *American Society for Composites* Nov. 2018;vol. 0, no. 0. <https://doi.org/10.12783/asc33/26149>.
- [588] Tang QJ, Fan WM, Ji J, Song YF. Defect detection of GFRP/NOMEX honeycomb sandwich structure by linear frequency modulation infrared thermal imagiy. *Therm Sci* 2021;25(6):4611–9. <https://doi.org/10.2298/TSCI2106611T>.
- [589] Subbarao V, Mulaveesla R, Takei M. "Cross-correlation based compression technique for frequency modulated thermal wave imaging", *Physics*. Md): College. Park; 2010.
- [590] Arora V, Mulaveesala R. Pulse compression with Gaussian weighted chirp modulated excitation for infrared thermal wave imaging. *Prog Electromagn Res Lett* 2014;44:133–7. <https://doi.org/10.2528/PIERL13111301>.
- [591] Lakha MV, Reddy KC. Image processing application for non destructive testing. In: *IEEE international conference on power, control, signals and instrumentation engineering, ICPCSI 2017*; 2018, p. 1490–1494, doi: 10.1109/ICPCSI.2017.8391960.
- [592] Petrov I, Vdovenko A, Dolmatov D, Sednev D. The implementation of post-processing algorithm for ultrasonic testing of welds. In: *IOP conference series: materials science and engineering*; 2019, vol. 510, no. 1, p. 012004, doi: 10.1088/1757-899X/510/1/012004.
- [593] Kreidl M, Houfek P. Using the correlation function in ultrasonic non-destructive testing. *Acta Polytech* 2002;42(3). <https://doi.org/10.14311/348>.
- [594] Stern Theodore. Mechanism of Micro-Crack Propagation in Semicrystalline Polymers. *Journal of Research Updates in Polymer Science* 2014;3:57–62. <https://doi.org/10.6000/1929-5995.2014.03.02.1>.